BOSTON UNIVERSITY

GRADUATE SCHOOL OF ARTS AND SCIENCES

Dissertation

THE OPEN BOSE–HUBBARD DIMER

by

TADEUSZ PUDLIK

B.A., Amherst College, 2009

Submitted in partial fulfillment of the

requirements for the degree of

Doctor of Philosophy

2016

Approved by

First Reader   _____

David K. Campbell, Ph.D.
Professor of Physics and ECE

Second Reader   _____

Anatoli Polkovnikov, Ph.D.
Professor of Physics

Acknowledgments

No project of nearly six years can be completed without incurring many debts of gratitude, and the work described in this dissertation is no exception. My advisor, David K. Campbell, deserves my first and foremost thanks for his patience, relentless optimism, and excitement for work relevant to experiment. Whether as a teacher, a research supervisor, or a collaborator, David treats others with a rare yet natural humanity and respect. I am especially grateful for his support when I worked remotely from Duke University for a year to live together with my wife.

The work described below owes much to discussions and correspondence with my two main collaborators, Dirk Witthaut and Holger Hennig. They pointed me to useful literature, shared the software they wrote, suggested and criticized ideas. I have also benefited greatly from discussions with Mike Kolodrubetz, Anatoli Polkovnikov, Stephen W. Teitsworth, Michael Tomka, and Stephanos Venakides.

I spent my first year of research at BU as an experimentalist in the lab of Bennett Goldberg and Anna Swan. I learned much about the practice of physics from them and their senior students, Alex Kitt and Sebastian Remi, and appreciate their understanding when I left to do theory.

My graduate school years would have been dreary without the companionship of my fellow students: the tennis games with Nahom Kifle, discussing Schutz (1980) and Hastie et al. (2009) with Shainen Davidson, the conversations with Tom Iadecola and Jason Christopher, the role-playing games with Michael Chernicoff, and above all the friend-

ship Tiago Souza and I have shared from our first days in QM1. These are some of the fondest memories from my time at the University.

Finally, I would like to thank my family. My parents, Bożena and Artur, have been enthusiastically supportive throughout these six years, as they had been for the preceding twenty-four. My brother Jacek was always there when I needed someone to talk to—or a couch to crash on in Paris. Above all, my wife, Mary Beth, kept up my spirits and provided inspiration and encouragement every day. I could not have done it without you.

THE OPEN BOSE–HUBBARD DIMER

TADEUSZ PUDLIK

Boston University, Graduate School of Arts and Sciences, 2016

Major Professor: David K. Campbell, Ph.D., Professor of Physics and ECE

ABSTRACT

This dissertation discusses a number of theoretical models of coupled bosonic modes, all closely related to the Bose–Hubbard dimer. In studying these models, we will repeatedly return to two unifying themes: the classical structure underlying quantum dynamics and the impact of weakly coupling a system to an environment. Or, more succinctly, semiclassical methods and open quantum systems.

Our primary motivation for studying models such as the Bose–Hubbard is their relevance to ongoing ultracold atom experiments. We review these experiments, derive the Bose–Hubbard model in their context and briefly discuss its limitations in the first half of Chapter 1. In its second half, we review the theory of open quantum systems and the master equation description of the dissipative Bose–Hubbard model. This opening chapter constitutes a survey of existing results, rather than original work.

In Chapter 2, we turn to the mean-field limit of the Bose–Hubbard model. After reviewing the striking localization phenomena predicted by the mean-field (and confirmed by experiment), we identify the first corrections to this picture for the dimer. The most interesting of these is the dynamical tunneling between the self-trapping points of the mean-field. We derive an accurate analytical expression for the tunneling rate using semiclassical techniques.

We continue studying the dynamics near the self-trapping fixed points in Chapter 3,

focusing on corrections to the mean-field that arise at larger nonlinearities and on shorter time scales than dynamical tunneling. We study the impact of dissipation on coherence and entanglement near the fixed points, and explain it in terms of the structure of the classical phase space.

The last chapter of the dissertation is also devoted to a dissipative bosonic dimer model, but one arising in a very different physical context. Abandoning optical lattices, we consider the problem of formulating a quantum model of operation of the cylindrical anode magnetron, a vacuum tube crossed-field microwave amplifier. We derive an effective dissipative dimer model and study its relationship to the classical description. Our dimer model is a first step towards the analysis of solid-state analogs of such devices.

Contents

List of Figures

List of Abbreviations and Symbols

BEC . Bose–Einstein condensate

BJJ . . bosonic Josephson junction

BH . . Bose–Hubbard

DNLS discrete nonlinear Schrödinger equation

GP . . Gross–Pitaevskii

$\hat{1}$ . . . . Identity operator

$\mathbb{1}\left(\cdot\right)$. Indicator function

Chapter 1

Introduction

In this chapter, we briefly review the experimental and theoretical developments that motivate our work. In particular, we discuss the phenomenon of Bose–Einstein condensation, the rise of optical lattices and related systems, the Bose–Hubbard model, and open quantum systems techniques.

1.1 Bose–Einstein condensation

The Bose-Einstein condensate (BEC) is an exotic state of matter originally predicted in the 1920s (Bose, 1924; Einstein, 1924), but created in the laboratory only in the remarkable experiments of Cornell and Wieman (Anderson et al., 1995), Ketterle (Davis et al., 1995), and Hulet (Bradley et al., 1995) in 1995.[1] In the BEC, the de Broglie wavelength of the atoms exceeds the interatomic spacing, and the atomic gas obeys quantum statistics. As a consequence, the condensate is characterized by the macroscopic population of a single quantum state; this leads to a host of unusual experimentally observable properties, such as matter-wave interference (Andrews et al., 1997), quantized vortices (Matthews et al., 1999), or solitons (Becker et al., 2008).

The literature on Bose–Einstein condensation is vast and no attempt will be made

---

[1]Superfluid Helium 4 is also a condensed state of bosons; it was observed by Kapitsa, Allen and Misener as early as 1937, and recognized as exhibiting BEC physics by Fritz London just a year later (London, 1938). However, due to strong interactions among the helium atoms the fraction of atoms participating in the condensate is low, approximately 0.1.

to summarize it here. Instead, the interested reader is referred to the many excellent textbooks (Pethick and Smith, 2008), monographs (Pitaevskii and Stringari, 2003), and reviews (Dalfovo et al., 1999; Castin, 2000; Leggett, 2001) of the subject.

1.2 Optical lattices

The first atomic Bose-Einstein condensates were confined in harmonic traps, but more interesting potentials were rapidly developed. At the very simplest, the condensate can be cut into two with a laser sheet (Andrews et al., 1997), or it may be composed of two different spin states (Zibold et al., 2010). In either case, we now have two condensates, the relative phase of which can be controlled by subjecting one of them to a microwave pulse. The next advance is loading the condensate into an optical lattice, an array of microscopic potentials induced by the ac Stark effect of interfering laser beams. The very latest developments, such as the quantum gas microscope (Bakr et al., 2009), allow for subjecting a condensate confined to a plane to an essentially arbitrary potential.

The strength and even sign of interactions among the atoms of the condensate can be tuned by means of a Feshbach resonance (Chin et al., 2010). The combination of tunable interactions with a range of external potentials is what gives ultracold atoms in optical lattices their rich behavior and makes them subjects of study not just in atomic but also in many-body and condensed matter physics. A famous early example of the rich phenomenology accessible in these systems was the observation of the Mott insulator-superfluid transition (Greiner et al., 2002a).

1.3 The Bose–Hubbard model

The aforementioned Mott insulator-superfluid transition in a sufficiently deep (strong) optical lattice can be most simply explained in the framework of the Bose–Hubbard model (Jaksch et al., 1998). This model will be the starting point for work described in this dissertation. Because of its central importance, in this section we show how the Bose–Hubbard arises from a more general description of the optical lattice and discuss its validity as an approximation to the full dynamics.

1.3.1 Derivation

We begin with the Hamiltonian,

$$
\begin{aligned}
H = \int d^3x \, \hat{\psi}^\dagger(\mathbf{x}) \left(-\frac{\hbar^2}{2m}\nabla^2 + V_0(\mathbf{x}) + V_T(\mathbf{x}) \right) \hat{\psi}(\mathbf{x}) \\
+ \frac{1}{2}\frac{4\pi a_s \hbar^2}{m} \int d^3x \, \hat{\psi}^\dagger(\mathbf{x})\hat{\psi}^\dagger(\mathbf{x})\hat{\psi}(\mathbf{x})\hat{\psi}(\mathbf{x}),
\end{aligned}
\tag{1.1}
$$

where V_0 is the periodic optical lattice potential, V_T the trap potential, and $\hat{\psi}(\mathbf{x})$ the bosonic field operator at $\mathbf{x}$. The interaction between the atoms is approximated by a short-range pseudopotential with an s-wave scattering length of a_s, appropriate if the gas is dilute: $na_s^3 \ll 1$, where n is the density (Dalfovo et al., 1999). The field operator can be expanded in Wannier functions indexed by i, which (since the potential V_0 is assumed deep) will be "well-localized" at the minima of the potential at x_i, in a sense to be made precise later. If we assume the energies in the system are low compared to the interband energy gap, we can restrict the expansion to the first band, and truncate the expansion at the first term:

$$
\hat{\psi}(\mathbf{x}) = \sum_i \hat{a}_i w(\mathbf{x} - \mathbf{x}_i),
\tag{1.2}
$$

By "well-localized" Wannier functions we mean such that integrals of the form,

$$\int d^3x\, V_0 w^*(\mathbf{x} - \mathbf{x}_i) w(\mathbf{x} - \mathbf{x}_j)$$

or

$$\int d^3x\, w^*(\mathbf{x} - \mathbf{x}_i) \nabla^2 w(\mathbf{x} - \mathbf{x}_j) \tag{1.3}$$

are negligibly small if sites i, j are more distant than nearest neighbors. Then, up to a term which is a constant if the number of atoms is conserved, the Hamiltonian of Equation 1.1 is the Bose–Hubbard model,[2]

$$H = -J \sum_{\langle i,j \rangle} \hat{a}_i^\dagger \hat{a}_j + \sum_i \epsilon_i \hat{n}_i + \frac{1}{2} U \sum_i \hat{n}_i (\hat{n}_i - \hat{1}), \tag{1.4}$$

where $\hat{n}_i \equiv \hat{a}_i^\dagger \hat{a}_i$ and the parameters are,[3]

$$
\begin{aligned}
J &= \int d^3x\, w^*(\mathbf{x} - \mathbf{x}_i) \left(-\frac{\hbar^2}{2m} \nabla^2 + V_0(\mathbf{x}) \right) w(\mathbf{x} - \mathbf{x}_{i+1}), \\
\epsilon_i &= \int d^3x\, V_T(\mathbf{x}) |w(\mathbf{x} - \mathbf{x}_i)|^2, \\
U &= \frac{4\pi a_s \hbar^2}{m} \int d^3x\, |w(\mathbf{x} - \mathbf{x}_i)|^4.
\end{aligned}
\tag{1.5}
$$

The consistency of this tight-binding model can be evaluated by considering a harmonic approximation in which the potential V_0 is expanded about the minimum of the well. If the frequency of the harmonic motion about the minimum is ν, the size of the harmonic ground state wavefunction is $a_0 = \sqrt{\hbar/m\nu}$, and the well spacing $\lambda/2$, the tight-binding model can only be valid if,

$$a_s \ll a_0 \ll \lambda/2,$$

---

[2] The notation $\sum_{\langle i,j \rangle}$ indicates a sum over nearest neighbors.

[3] J and U are independent of i because of the translational symmetry of the lattice.

that is, the interaction is localized relative to the orbitals, which are in turn localized on the scale of the lattice spacing, and

$$\frac{1}{2}Un_i(n_i - 1) \ll \hbar v \quad \forall i,$$

that is, the interaction energy is much smaller than the band spacing (so the higher bands remain unoccupied).

These conditions are typically satisfied in optical lattice experiments. But while necessary, they are in general not sufficient for the Bose–Hubbard model to be a good approximation. Studies of small systems with more accurate techniques such as the multiconfigurational time-dependent Hartree algorithm, which allow for the treatment of multiple bands, show that the Bose–Hubbard approximation to an optical lattice may be misleading in certain parameter regimes (Sakmann et al., 2009; Sakmann, 2010, 2011). Such discrepancies are yet to be observed experimentally.

1.3.2   The Bose–Hubbard without an optical lattice

In the preceding section we derived the Bose–Hubbard model in the context of an optical lattice, arguably its most natural realization in cold-atom physics. Other realizations are possible, however; many experimental groups today, including those performing work most closely related to this thesis, choose to employ internal, rather than motional, bosonic degrees of freedom. Such realizations were originally conceived by Cirac et al. (1998). The derivation of the Bose–Hubbard model in this context is similar to the one presented above, with plain localized spatial wavefunctions replacing Wannier functions. The key assumption is again the restriction to a single such wavefunction, in this context referred to as the "one-mode approximation."

The one-mode approximation is expected to break down in large condensates, when

collisional interactions among atoms in a mode affect the spatial wavefunction (Steel and Collett, 1998). A simple estimate due to Milburn et al. (1997) suggests the critical size is a few hundred atoms. Another potential problem is that the spatial wavefunction may be spin-dependent, as a result of the spin-dependence of the *s*-wave scattering length a_s. This effect can be estimated by studies of the ground state modes of the two species (Zibold, 2012, Section 3.6) and has been shown to be small for experimentally relevant parameter values.

1.3.3 Mean-field approximation

If the number of atoms per mode is large, the dynamics of interacting cold atoms can be approximately described by a mean-field model. In this section we briefly review its standard derivation due to Trombettoni and Smerzi (2001), by first obtaining the Gross–Pitaevskii (GP) equation and then making the single-mode approximation, leading to the discrete nonlinear Schrödinger (DNLS) equation. In the next chapter, we will discuss an alternative approach, deriving the DNLS for the dimer case directly from the Bose–Hubbard model.

Consider again the many-body Hamiltonian of Equation 1.1. Using the canonical commutation relation $[\hat{\psi}(\mathbf{x}), \hat{\psi}(\mathbf{x}')] = \delta(\mathbf{x} - \mathbf{x}')$, the equation of motion of the bosonic field operator can be shown to be,

$$\imath\hbar\frac{\partial}{\partial t}\hat{\psi}(\mathbf{x}, t) = [\hat{\psi}(\mathbf{x}), H] = \left(-\frac{\hbar^2}{2m}\nabla^2 + V_0(\mathbf{x}) + V_T(\mathbf{x}) + \frac{4\pi a_s\hbar^2}{m}\hat{\psi}(\mathbf{x})^\dagger\hat{\psi}(\mathbf{x})\right)\hat{\psi}(\mathbf{x}). \quad (1.6)$$

We decompose the field operator in a generalization of Bogoliubov's approach (Dalfovo et al., 1999),

$$\hat{\psi}(\mathbf{x}, t) = \Phi(\mathbf{x}, t) + \hat{\psi}'(\mathbf{x}, t), \quad (1.7)$$

where $\Phi(\mathbf{x}, t) \equiv \langle \hat{\psi}(\mathbf{x}, t) \rangle$. The mean field approximation consists of setting $\hat{\psi}'(\mathbf{x}, t) = 0$. The equation of motion for Φ follows immediately from Equation 1.6:

$$\imath\hbar\frac{\partial\Phi(\mathbf{x}, t)}{\partial t} = \left(-\frac{\hbar^2}{2m}\nabla^2 + V_0(\mathbf{x}) + V_T(\mathbf{x}) + \frac{4\pi a_s\hbar^2}{m}|\Phi(\mathbf{x}, t)|^2\right)\Phi(\mathbf{x}, t). \tag{1.8}$$

This is the Gross–Pitaevskii equation.

To obtain a mean-field approximation to the Bose–Hubbard model, we make a tight-binding approximation to the GP equation (Smerzi et al., 1997; Raghavan et al., 1999). Specifically, we assume the mean-field wavefunction can be decomposed,

$$\Phi(\mathbf{x}, t) \approx \sqrt{N}\sum_n \psi_n(t)\phi_n(\mathbf{x}), \tag{1.9}$$

where N is the number of atoms in the system, and $\phi_n(\mathbf{x}) \equiv \phi(\mathbf{x} - \mathbf{x}_n)$ is normalized ($\int |\phi_n(\mathbf{x})|^2 d^3\mathbf{x} = 1$) and localized near the nth minimum of V_0, so that

$$\int \phi_n(\mathbf{x})\phi_{n+1}(\mathbf{x}) d^3\mathbf{x} \approx 0, \quad \int \nabla\phi_n \cdot \nabla\phi_{n+k} d^3\mathbf{x} \approx 0 \text{ if } |k| > 1. \tag{1.10}$$

Substituting this decomposition into the GP equation, multiplying by $\phi_k^*(\mathbf{x})$ and integrating over all space, we obtain (dropping the explicit $\mathbf{x}$ dependence of ϕ_n for legibility),

$$\imath\hbar\frac{\partial\psi_k}{\partial t} = -\frac{\hbar^2}{2m}\left(\psi_k\int (\nabla\phi_k)^2 d^3\mathbf{x} + \psi_{k+1}\int \nabla\phi_k \cdot \nabla\phi_{k+1} d^3\mathbf{x} + \psi_{k-1}\int \nabla\phi_k \cdot \nabla\phi_{k-1} d^3\mathbf{x}\right)$$
$$+ \psi_{k+1}\int \phi_k^*\phi_{k+1}V_0(\mathbf{x}) d^3\mathbf{x} + \psi_{k-1}\int \phi_k^*\phi_{k-1}V_0(\mathbf{x}) d^3\mathbf{x} + \psi_k\int |\phi_k|^2 V_T(\mathbf{x}) d^3\mathbf{x}$$
$$+ \frac{4\pi a_s\hbar^2}{m}N|\psi_k|^2\psi_k\int |\phi_k|^4 d^3\mathbf{x}.$$

Regrouping the terms,

$$i\hbar\frac{\partial\psi_k}{\partial t} = -(\psi_{k+1} + \psi_{k-1})\left[\frac{\hbar^2}{2m}\int \nabla\phi_k \cdot \nabla\phi_{k+1}\, d^3\mathbf{x} - \int \phi_k^*(\mathbf{x})\phi_{k+1}V_0(\mathbf{x})\, d^3\mathbf{x}\right]$$

$$+ \psi_k\left[\int |\phi_k|^2 V_T(\mathbf{x})\, d^3\mathbf{x} - \frac{\hbar^2}{2m}\int (\nabla\phi_k)^2\, d^3\mathbf{x}\right]$$

$$+ \frac{4\pi a_s\hbar^2}{m}N|\psi_k|^2\psi_k\int |\phi_k|^4\, d^3\mathbf{x}.$$

Now, let

$$J = \frac{\hbar^2}{2m}\left[\int \nabla\phi_k(\mathbf{x}) \cdot \nabla\phi_{k+1}\, d^3\mathbf{x} - \int \phi_k^*(\mathbf{x})\phi_{k+1}(\mathbf{x})V_0(\mathbf{x})\, d^3\mathbf{x}\right],$$

$$\varepsilon_k = \frac{1}{2J}\left[\int |\phi_k(\mathbf{x})|^2 V_T(\mathbf{x})\, d^3\mathbf{x} - \frac{\hbar^2}{2m}\int (\nabla\phi_k(\mathbf{x}))^2\, d^3\mathbf{x}\right], \qquad (1.11)$$

$$\Lambda = \frac{4\pi a_s\hbar^2 N}{2Jm}\int |\phi_k(\mathbf{x})|^4\, d^3\mathbf{x},$$

and define a de-dimensionalized time scale $\tau = \frac{2J}{\hbar}t$. This yields the discrete nonlinear Schrödinger equation,

$$i\frac{\partial\psi_k}{\partial\tau} = -\frac{1}{2}\left(\psi_{k+1} + \psi_{k-1}\right) + \varepsilon_k\psi_k + \Lambda|\psi_k|^2\psi_k. \qquad (1.12)$$

Comparing the parameters of the DNLS equation with those of the Bose–Hubbard (Equation 1.5), it is tempting to conclude that $\Lambda = UN/2J$. However, the replacement of operators with c-numbers in the derivation of the GP equation is valid only in the limit of large atom number N, when $N \approx N \pm 1$, so this expression is only expected to be valid asymptotically as $N \to \infty$. As we will show in Chapter 2, a more careful analysis, with due attention devoted to symmetrizing operators before replacing them with c-numbers, shows that $\Lambda = U(N + 1)/2J$.

1.4 Open quantum systems

In this section we review the theory of open quantum systems (Breuer and Petruccione, 2002), which provides a set of techniques for modeling quantum systems coupled to external reservoirs. In Chapters 3 and 4, these techniques will be applied to the study of two models consisting of a dimer exchanging energy and particles with reservoirs: the open Bose–Hubbard dimer and the quantum magnetron, respectively.

1.4.1 The Born–Markov master equation

The primary subject of study in textbook quantum mechanics is an isolated system, such as a particle in a harmonic potential, the electrons and nuclear cores comprising a molecule, or electrons in a lattice potential. But there arise situations in which the small system we are interested in studying is weakly coupled to a much larger system which cannot be entirely ignored. Examples of this include atoms interacting with a microwave cavity (Carmichael, 1993), quantum dots coupled to leads (Datta, 2005), or applications requiring quantum feedback and control (Wiseman and Milburn, 2010).

Because the environment to which our small system is coupled is typically not of inherent interest, yet much too large to treat exactly, the first step is to derive an effective model of the system into which the environment only enters parametrically. In other words, the model should include no quantum operators defined on the large Hilbert space of the environment. Achieving this requires approximations, most commonly the Born approximation (weak system-environment coupling) and the Markov approximation (the environment is too large for its dynamics to be affected by the dynamics of the system). Applying these approximations yields the so-called Born–Markov master equation governing the time evolution of the system's density matrix. A physically meaningful Markovian master equation can always be expressed in the so-called Lindblad form (Wiseman

and Milburn, 2010, p. 119),

$$\frac{d\rho}{dt} = -\iota[\hat{H}, \rho] + \sum_{k=1}^{K} \mathcal{D}[\hat{L}_k]\rho, \tag{1.13}$$

where ρ is the density matrix of the system, $\hat{H}$ is a Hermitian operator, $\{\hat{L}_k\}$ are arbitrary operators such that $\sum_{k=1}^{K} \hat{L}_k^\dagger \hat{L}_k$ is a bounded operator,[4] and the superoperator $\mathcal{D}$ is defined as,

$$\mathcal{D}[\hat{A}]\rho \equiv \hat{A}\rho\hat{A}^\dagger - \frac{1}{2}\left(\hat{A}^\dagger\hat{A}\rho + \rho\hat{A}^\dagger\hat{A}\right). \tag{1.14}$$

For a BEC in an optical lattice in the single-mode (i.e., Bose–Hubbard) approximation coupled to a thermal gas of noncondensed atoms, the master equation reads (Anglin, 1997; Ruostekoski and Walls, 1998; Witthaut et al., 2011),

$$\frac{d\rho}{dt} = -\iota[H, \rho] + \sum_{j} \gamma_j \mathcal{D}[\hat{a}_j]\rho + \kappa \mathcal{D}[\hat{a}_j^\dagger \hat{a}_j]\rho, \tag{1.15}$$

where H is the Hamiltonian (Equation 1.4) and $\hat{a}_j$ annihilates a boson in the jth mode. The two superoperators represent the loss of bosons to the thermal gas (with rates γ_j) and the heating of the system, resulting in a loss of phase coherence (with a rate κ). If the atom losses are solely due to interactions with the thermal gas, then all the γ_j are equal, and γ and κ are functions of the gas temperature, its chemical potential, and the trapping potential (Anglin, 1997). But we will be concerned with the general case, in which additional losses are introduced in a controlled manner, and $\gamma_j \gg \kappa$ for some j.

In Appendix D we derive another master equation, describing the dissipative bosonic dimer model of the magnetron discussed in Chapter 4.

---

[4]An operator $\hat{L}$ on a normed vector space is bounded if $\|\hat{L}v\| < M\|v\|$ for some $M \in \mathbb{R}$ and all vectors v in the space. Although Lindblad (1976) proved the necessity of this condition for a physical master equation, Wiseman and Milburn (2010, p .119) point out that it is often violated by operators of interest in practice. This inconsistency remains an open problem.

1.4.2 Quantum jump method

For small systems, the master equation can be integrated directly. But if the Hilbert space dimension is large, it may be preferable to use a Monte Carlo approach known as the quantum jump or Monte Carlo wave function method (Dalibard et al., 1992; Carmichael, 1993; Plenio and Knight, 1998). The quantum jump method simulates a stochastic process in Hilbert space for which the expectation values of all observables (averaged over realizations of the stochastic process) are the same as for the original Born–Markov equation. The advantage of this approach is that only the wavefunction, a vector in Hilbert space of dimension N, must be stored and operated upon, rather than the full density matrix of dimension N^2. In this section, we derive the quantum jump algorithm and discuss its implementation and performance.

1.4.2.1 Quantum measurement theory

The quantum jump algorithm can be derived by viewing the system-bath interaction from a quantum measurement theory perspective (Wiseman and Milburn, 2010). Although this can be done at a high level of generality, we will consider the specific case of a Bose–Hubbard system subject to atom loss. The central idea is to consider the loss of an atom from a well as a measurement performed on the system: by detecting the loss, we gain information about the system, because we learn that immediately before detection the well contained at least one atom. In quantum measurement theory, a measurement process is described in terms of measurement operators $\{\hat{M}_r\}$, such that the state of the system (conditional on the measurement result being r) is,

$$|\psi_r(t + dt)\rangle = \frac{\hat{M}_r |\psi(t)\rangle}{\sqrt{p_r}}, \tag{1.16}$$

where p_r is the probability of the measurement result being r,

$$p_r = \langle \psi(t) | \hat{M}_r^\dagger \hat{M}_r | \psi(t) \rangle . \tag{1.17}$$

In the case of a M-well Bose–Hubbard system leaking atoms, we have M possible measurement results, corresponding to an atom decaying from well 1, 2, …, M, and the measurement operators are proportional to the annihilation operators,

$$\hat{M}_r = \hat{a}_r \sqrt{\gamma_r \, dt}, \quad r \in \{1, 2, \ldots, M\}. \tag{1.18}$$

Less obviously, there is one more possible measurement result: we may not detect an atom between times t and $t + dt$. This null result also has a corresponding operator, $\hat{M}_0$. Based on Equation 1.16 one might expect that this operator is proportional to the identity: the system has not been affected. However, the probabilities of the measurement outcomes (Equation 1.17) must add up to 1 for an arbitrary wavefunction. This means,

$$\hat{M}_0 = \hat{1} - \left(\imath \hat{H} + \frac{1}{2} \sum_r \gamma_r \hat{a}_r^\dagger \hat{a}_r \right) dt, \tag{1.19}$$

for some Hermitian operator $\hat{H}$. (As we will see shortly, to recover the Born–Markov master equation of the previous section we must let $\hat{H}$ be the Hamiltonian.[5]) The curious fact that $\hat{M}_0 \neq \hat{1}$ can be interpreted as follows: the absence of a removal event reveals information about the system, changing the probability distribution over the well occupation numbers and so altering the wave functions. Intuitively, if strong dissipation is applied to a well and yet no atoms are ejected from it, the well is likely to be empty. Alternatively, in the context of a Bose–Hubbard model, one may interpret the suppression of

---

[5]This can already be intuited, since in the dissipationless case $\frac{d}{dt} |\psi(t)\rangle = -\imath H |\psi(t)\rangle$, a special case of Equation 1.16 with $\hat{M}_0 = -\imath \hat{H} dt$.

tunneling into the dissipative well as a manifestation of the quantum Zeno effect (Cirac et al., 1994). See Section 3 of Mølmer et al. (1993) for a more detailed discussion and references devoted specifically to this paradoxical "null measurement" phenomenon.

If we perform a measurement on the system and observe the outcome to be r, it follows from Equation 1.16 that the system's density matrix is now given by,

$$\rho_r(t+dt) = \frac{\hat{M}_r \rho \hat{M}_r^\dagger}{p_r}. \tag{1.20}$$

But if we perform the measurement and *do not* observe the outcome, our knowledge of the system's state is described by the weighted average,

$$\rho(t+dt) = \sum_r p_r \rho_r = \sum_r \hat{M}_r \rho \hat{M}_r^{\dagger}. \tag{1.21}$$

In the case of the leaky Bose–Hubbard model,

$$\rho(t+dt) = \left[\hat{1} - \left(\iota\hat{H} + \frac{1}{2}\sum_r \gamma_r \hat{a}_r^\dagger \hat{a}_r\right) dt\right] \rho \left[\hat{1} - \left(-\iota\hat{H} + \frac{1}{2}\sum_r \gamma_r \hat{a}_r^\dagger \hat{a}_r\right) dt\right] + \sum_r \hat{a}_r \rho \hat{a}_r^\dagger\, dt$$

$$= \rho - \iota[H,\rho]dt + \sum_r \mathcal{D}[\hat{a}_r]\rho\, dt,$$

or,

$$\frac{d\rho}{dt} = -\iota[H,\rho] + \sum_r \mathcal{D}[\hat{a}_r]\rho.$$

Thus, the Born–Markov equation describes the evolution of the system under a continuous measurement, the results of which are not observed. Although the microscopic measurement process involves discontinuous jumps (Equation 1.16), we average over them because their timing is random, obtaining a continuous evolution equation for a probabilistic description of the state of the system. In this sense, the master equation is analogous to a Fokker–Planck equation.

But to every Fokker–Planck equation corresponds a Langevin equation, a stochastic differential equation for individual trajectories. Similarly, we can describe the measurement process in terms of a stochastic differential equation for the wavefunction. Let $N_r(t)$ be the number of atoms which have decayed from well r, and $dN_r(t)$ a stochastic increment which satisfies,

$$dN_r(t)^2 = dN_r(t),$$

$$\mathrm{E}[dN_r(t)] = p_r.$$

From Equation 1.16,

$$|\psi_r(t+dt)\rangle = \frac{\hat{a}_r |\psi\rangle (t)}{\sqrt{\langle \hat{a}^\dagger \hat{a}\rangle(t)}} \qquad r \neq 0, \tag{1.22}$$

and (expanding a denominator to first order in dt),

$$|\psi_0(t+dt)\rangle = \left(\hat{1} - \left(\imath H + \frac{1}{2}\sum_r \hat{a}_r^\dagger \hat{a} - \frac{1}{2}\sum_r \langle \hat{a}_r^\dagger \hat{a}_r\rangle(t)\right)dt\right)|\psi(t)\rangle. \tag{1.23}$$

The wavefunction evolves according to the stochastic Schrödinger equation,

$$
\begin{aligned}
d\,|\psi(t)\rangle = &\left(\hat{1} - \sum_r dN_r(t)\right)dt\left(-\imath H - \frac{1}{2}\sum_r \hat{a}_r^\dagger \hat{a} + \frac{1}{2}\sum_r \langle \hat{a}_r^\dagger \hat{a}_r\rangle(t)\right)|\psi(t)\rangle \\
&+ \sum_r dN_r(t)\left(\frac{\hat{a}_r}{\sqrt{\langle \hat{a}^\dagger \hat{a}\rangle(t)}} - \hat{1}\right)|\psi(t)\rangle,
\end{aligned} \tag{1.24}
$$

or equivalently,

$$
\begin{aligned}
d\,|\psi(t)\rangle = &\,dt\left(-\imath H - \frac{1}{2}\sum_r \hat{a}_r^\dagger \hat{a} + \frac{1}{2}\sum_r \langle \hat{a}_r^\dagger \hat{a}_r\rangle(t)\right)|\psi(t)\rangle \\
&+ \sum_r dN_r(t)\left(\frac{\hat{a}_r}{\sqrt{\langle \hat{a}^\dagger \hat{a}\rangle(t)}} - \hat{1}\right)|\psi(t)\rangle.
\end{aligned} \tag{1.25}
$$

The basic idea behind the quantum jump algorithm is to repeatedly solve this equation numerically (with different realizations of the stochastic increment) and estimate $\rho(t)$ as the average of $|\psi(t)\rangle \langle \psi(t)|$ over the realizations.

1.4.2.2 Algorithms for the stochastic Schrödinger equation

The simplest method for simulating the stochastic Schrödinger equation of the previous section is the following procedure due to Mølmer et al. (1993). We start with a simulation time interval $[0, T]$ and an initial state described by a wavefunction $|\psi(t = 0)\rangle$. The time interval is divided into time steps δt. At each time step, we do the following:

1. Evolve the state with the operator,

$$U = \exp\left(((\hat{M}_0 - \hat{1})\delta t \right),$$

   which solves Equation 1.16 in the null case when no measurement occurred. Note that in the absence of dissipation ($\gamma_j = 0 \ \forall j$) this reduces to ordinary time evolution, as $(\hat{M}_0 - \hat{1})$ is then ιH.

2. Draw a random number $x \sim U(0, 1)$ and compare it to,

$$p = \sum_r \gamma_r \langle \psi| \hat{a}_r^\dagger \hat{a}_r |\psi\rangle \, \delta t.$$

   If $x < p$, draw another random number $y \sim U(0, 1)$ to choose one of the wells (with probabilities summing to 1 and proportional to p_r) and update the wavefunction by removing an atom from the chosen well,

$$|\psi\rangle \rightarrow \hat{a}_r |\psi\rangle.$$

This is the quantum jump.

3. Regardless of whether a jump took place or not, normalize the wavefunction.

A superior algorithm can be devised by recalling that the norm of the wavefunction evolved with U, i.e. $\|\langle\psi|\hat{M}_0^\dagger\hat{M}_0|\psi\rangle\|^2$, is the probability that no jump has taken place during the evolution (Equation 1.17). Thus, instead of evolving the wavefunction in steps of δt and generating a random number at each time step, we can adopt the following procedure (Breuer and Petruccione, 2002, Section 7.1.3.3):

1. Draw a random number $x \sim U(0, 1)$.

2. Use a standard ODE solver to integrate,

$$\frac{d|\psi\rangle}{dt} = (\hat{M}_0 - \hat{1})|\psi\rangle, \tag{1.26}$$

   from the initial time to T, checking at each integration step whether the norm $\|\langle\psi|\psi\rangle\|^2 > x$.

3. If $\|\langle\psi|\psi\rangle\|^2 < x$ at any time step, perform a quantum jump: $|\psi\rangle \to \hat{a}_r|\psi\rangle$, with $r \in \{1, 2, \ldots, M\}$ chosen at random with probabilities proportional to $\gamma_r\langle\psi|\hat{a}_r^\dagger\hat{a}_r|\psi\rangle$. Then, restart the procedure with the current time and wavefunction as the initial conditions (i.e., draw a new x value and continue integrating).

Although this algorithm is faster than the naive one, it suffers from a potential accuracy issue: the timing of the jump is only determined with a precision of one integrator time step. This will lead to a loss of precision when using a high-order or adaptive integration method, which may have large intervals between time steps. The problem can be solved using a "trick" developed by Henon (1982) in the context of computing Poincaré maps, a task which also requires determining the time when some function of the ODE

solution takes on a specified value to a precision greater than the integration time step. Call this time we wish to determine τ. Henon's "trick" in the context of our problem works as follows:

1. Let the integrator that evolves the wavefunction in time also evolve its norm. When the norm falls below the prescribed value, the integrator returns. This gives an (over)estimate of τ good to approximately one time integration step.

2. Next, perform a change of variables: let the wavefunction norm, rather than the time, be the independent variable. Evolve the system back to the (nearby) point where norm = 0. This gives an estimate of τ good to the precision of the integrator (i.e., as good as the estimates of the other observables).

For a more detailed description see the implementation of the quantum jump algorithm in Appendix A, or Henon's original paper.

In closing, we make a few remarks about the performance of the quantum jump algorithm relative to the direct integration of the master equation. For a system with a Hilbert space dimension N, direct integration requires solving $O(N^2)$ coupled ODEs, which involves $O(N^4)$ scalar multiplications per time step and requires $O(N^2)$ memory to store the density matrix. In contrast, the quantum jump algorithm solves $O(N)$ coupled ODEs K times; therefore, the number of operations required is $O(N^2K)$, and the amount of memory required is $O(N)$. For a system with tens of thousands of dimensions, $K \approx N$ is generally sufficient, giving $O(N^3)$ performance. However, the K trajectories can be easily computed in parallel, so this seriously understates the gain in performance. Furthermore, the decreased memory footprint is critical: for a system with a Hilbert space dimension of $N = 10^5$, a dense double-precision density matrix would require 75 GB of memory to store, while the wavefunction is smaller than 1 MB. As long as only expectation values

of observables are desired, the full density matrix need never be computed; they can be found by averaging the expectation values for individual trajectories,

$$\text{Tr}(\rho\hat{A}) = \text{E}[\langle\psi|\hat{A}|\psi\rangle].$$

This is the approach we have taken in our simulations.

Chapter 2

Dynamical tunneling in the Bose–Hubbard dimer

In this chapter we engage in a closer study of the mean-field approximation in the case of the two-site Bose–Hubbard (BH) model. We give a more careful derivation of the mean-field approximation, and review its dynamics with a focus on the onset of self-trapping. We then develop a semiclassical description of the breakdown of self-trapping as the number of atoms becomes small.

This chapter is partially based on work published as Pudlik et al. (2014).

2.1 The Hamiltonian and $SU(2)$ coherent states

In this chapter, we will study the Bose–Hubbard dimer, with the Hamiltonian,

$$\hat{H} = -J(\hat{a}_1^\dagger \hat{a}_2 + \hat{a}_2^\dagger \hat{a}_1) + \frac{U}{2}\Big(\hat{n}_1(\hat{n}_1 - \hat{1}) + \hat{n}_2(\hat{n}_2 - \hat{1})\Big). \tag{2.1}$$

where $\hat{n}_i \equiv \hat{a}_i^\dagger \hat{a}_i$. The Hamiltonian commutes with the total boson number operator $\hat{N} = \hat{n}_1 + \hat{n}_2$. Consequently, using the identity,

$$\Big(\hat{N}^2 + (\hat{n}_1 - \hat{n}_2)^2)\Big) - \hat{N} = \hat{n}_1(\hat{n}_1 - \hat{1}) + \hat{n}_2(\hat{n}_2 - \hat{1}),$$

and dropping terms proportional to $\hat{N}$, which do not affect the dynamics, we can rewrite the Hamiltonian as,

$$H = -J(\hat{a}_1^\dagger \hat{a}_2 + \hat{a}_2^\dagger \hat{a}_1) + \frac{U}{2}(\hat{n}_1 - \hat{n}_2)^2. \tag{2.2}$$

The operators appearing in the Hamiltonian can be combined to form an su(2) algebra,

$$\hat{L}_x = \frac{1}{2}(\hat{a}_1^\dagger \hat{a}_2 + \hat{a}_2^\dagger \hat{a}_1),$$

$$\hat{L}_y = \frac{\imath}{2}(\hat{a}_1^\dagger \hat{a}_2 - \hat{a}_2^\dagger \hat{a}_1), \tag{2.3}$$

$$\hat{L}_z = \frac{1}{2}(\hat{a}_2^\dagger \hat{a}_2 - \hat{a}_1^\dagger \hat{a}).$$

In terms of these operators, Equation 2.2 takes the concise form,

$$H = -2J\hat{L}_x + 2U\hat{L}_z^2. \tag{2.4}$$

Rewritten this way, the Bose–Hubbard dimer is equivalent to the $\gamma_z = 0$ case of the Lipkin-Meshkov-Glick model (Lipkin et al., 1965; Meshkov et al., 1965; Glick et al., 1965),

$$H_{\text{LMG}} = hL_z + \gamma_x L_x^2 + \gamma_z L_z^2. \tag{2.5}$$

Furthermore, from Equation 2.4 it is manifest that the dynamical group of H is $SU(2)$.[1] This fact can be used to construct a family of symmetry-adapted coherent states (Zhang et al., 1990), the $SU(2)$ coherent states, which we introduce next.

Given the total number of bosons N, a basis for the Hilbert space is provided by the Fock states,

$$|n_1, n_2\rangle = \frac{1}{\sqrt{n_1! n_2!}}(\hat{a}_1^\dagger)^{n_1}(\hat{a}_2^\dagger)^{n_2} |0, 0\rangle, \tag{2.6}$$

---

[1]The dynamical group of a system is the group corresponding to the Lie algebra spanned by a complete set of operators in terms of which one can write the Hamiltonian.

where $|0, 0\rangle$ represents the vacuum state. These states provide a convenient basis for numerical work, but are not typical of the experiments described in the first chapter. In particular, a Bose–Einstein condensate is represented by states of the form,

$$|x_1, x_2\rangle_c = \frac{1}{\sqrt{N!}} (x_1 \hat{a}_1^\dagger + x_2 \hat{a}_2^\dagger)^N |0, 0\rangle \,. \tag{2.7}$$

These states are equivalent to $SU(2)$ or atomic coherent states (Arecchi et al., 1972) and form a foundation for the development of phase-space methods and approximations (Brif and Mann, 1999). In particular, they can be used to derive exact equations for the evolution of quasiprobability distributions such as the Husimi Q and Glauber-Sudarshan P. The mean-field model can be recovered from these equations by *(a)* dropping the second-order quantum diffusion terms, which decrease in amplitude relative to the first-order terms like $1/N$ as the particle number increases, and *(b)* approximating the quasiprobability distribution with a Gaussian of width $\sim 1/N$ centered at its mean. We will not discuss this fascinating perspective further here, but refer the interested reader to the works of Trimborn et al. (2008a,b, 2009).

2.2   The mean-field approximation

If the number of atoms per mode is large, the dynamics of the Bose–Hubbard model can be approximately described by mean-field equations. We have already discussed the historical derivation of this model through the GP equation. An alternative approach is to start with the Bose–Hubbard Hamiltonian of Equation 2.1 and perform a replacement of operators with c numbers,

$$\begin{aligned} \hat{a}_j &\rightarrow \psi_j \\ \hat{a}_j^\dagger &\rightarrow \psi_j^* \end{aligned} \tag{2.8}$$

To avoid ambiguities, the Hamiltonian must first be symmetrized (Graefe and Korsch, 2007; Mossmann and Jung, 2006). After dropping constant terms, this procedure yields the classical Hamiltonian,

$$H = -J(\psi_1^*\psi_2 + \psi_2^*\psi_1) + \frac{U}{2}(|\psi_1|^4 + |\psi_2|^4), \tag{2.9}$$

with equations of motion,

$$\begin{aligned}
\imath\hbar\frac{\partial\psi_j}{\partial t} &= \frac{\partial H}{\partial\psi_j^*}, \\
\imath\hbar\frac{\partial\psi_j^*}{\partial t} &= -\frac{\partial H}{\partial\psi_j}.
\end{aligned} \tag{2.10}$$

The symmetrized number operators satisfy,

$$\hat{N} = \hat{n}_1 + \hat{n}_2 = \hat{n}_1^s + \hat{n}_2^s - \hat{1},$$

which after the replacement of Equation 2.8 becomes $|\psi_1|^2 + |\psi_2|^2 - 1 = N$. Thus, to normalize the coordinates, we perform the transformation to new coordinates $\varphi_j = \psi_j/\sqrt{N+1}$. The canonical equations of motion are preserved if the Hamiltonian takes the form,

$$H = -J(\varphi_1^*\varphi_2 + \varphi_2^*\varphi_1) + \frac{U(N+1)}{2}(|\varphi_1|^4 + |\varphi_2|^4).$$

Setting $\Lambda = U(N+1)/2J$ and defining a dimensionless time $\tau = 2Jt/\hbar$, we get the dimensionless Hamiltonian,

$$H = -\frac{1}{2}(\varphi_1^*\varphi_2 + \varphi_2^*\varphi_1) + \frac{\Lambda}{2}(|\varphi_1|^4 + |\varphi_2|^4). \tag{2.11}$$

The corresponding canonical equation of motion,

$$\iota \frac{\partial \varphi_j}{\partial \tau} = \frac{\partial H}{\partial \varphi_j^*} = -\frac{\varphi_{-j}}{2} + \Lambda |\varphi_j|^2 \varphi_j,$$

is the two-mode variant of the DNLS equation (Equation 1.12). If we perform an amplitude-phase decomposition $\varphi_j = \sqrt{x_j} \exp(\iota \theta_j)$ followed by the canonical transformation,

$$(z, Z, \phi', \Phi) = \left(x_1 - x_2, \frac{x_1 + x_2}{2}, \frac{\theta_1 - \theta_2}{2}, \theta_1 + \theta_2 \right),$$

we can bring the Hamiltonian into the form (Graefe and Korsch, 2007),

$$H = \frac{\Lambda z^2}{4} - \frac{1}{2}\sqrt{1 - z^2} \cos 2\phi'. \tag{2.12}$$

Finally, we perform a transformation to coordinates (z, ϕ), where $\phi = 2\phi'$. This transformation is not canonical, as it does not preserve phase space volume, but it is canonoid with respect to H (Jose and Saletan, 1998, p. 233): the equations of motion in the new coordinate system are still Hamilton's equations for some Hamiltonian. That new Hamiltonian is the one used by Raghavan et al. (1999),[2]

$$H = \frac{\Lambda z^2}{2} - \sqrt{1 - z^2} \cos \phi. \tag{2.13}$$

These transformations reveal that the system has only one degree of freedom, rather than the two one might have expected from Equation 2.11. Physically, this reflects the facts that the overall phase of the mean-field wavefunctions φ_j has no significance, and that the number of atoms $|\varphi_1|^2 + |\varphi_2|^2 = x_1 + x_2 = 2Z$ is conserved. The variables that do appear in the Hamiltonian represent the population (z) and phase (ϕ) differences between the

---

[2]Note that the new Hamiltonian cannot be obtained simply by replacing $2\phi'$ with ϕ in the old Hamiltonian, as would be the case if the transformation were canonical.
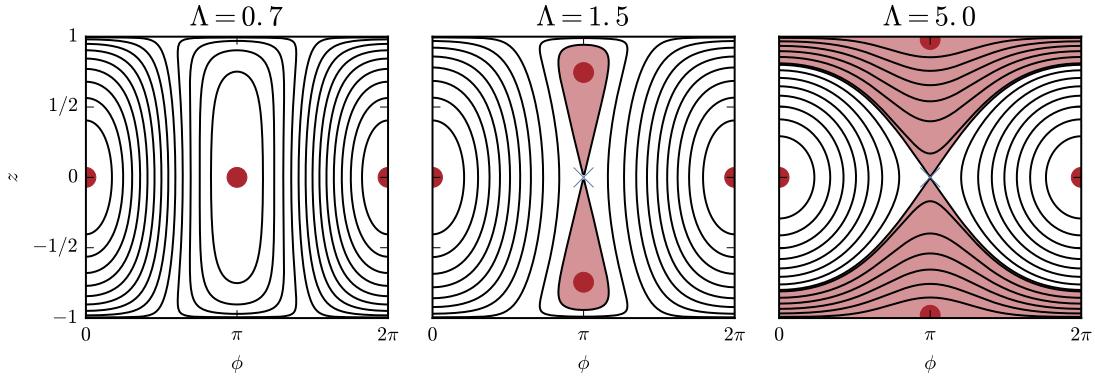
Figure 2.1: The phase portrait of the BJJ model at different values of the parameter Λ. The self-trapping region is shown in red, and the stable fixed points as red dots. The unstable fixed point is marked with a blue cross.

two modes. Mathematically, the phase space of the DNLS Hamiltonian of Equation 2.11 is the complex projective space $\mathbb{CP}^1$, which is isomorphic to the sphere. The coordinates z and ϕ are cylindrical coordinates for this sphere.

To avoid confusion with the GP equation (Equation 1.8), which is also obtained via a mean-field approximation, we will refer to the mean-field model of Equation 2.13 as the bosonic Josephson junction (BJJ) model.

2.3 Dynamics of the BJJ model

The phase portrait of the BJJ model at different values of Λ is shown in Figure 2.1. For $\Lambda <$ 1, the system has two stable fixed points, centers at $(z, \phi) = (0, 0)$ and $(0, \pi)$; when $\Lambda =$ 0, the periodic motion around them corresponds to Rabi oscillations of N independent particles. The model exhibits a bifurcation at $\Lambda = 1$:[3] as Λ is increased beyond this critical

---

[3]The general bosonic Josephson junction undergoes a Hamiltonian saddle-node bifurcation (Howard, 2013) when the nonlinearity is increased. At the bifurcation, a new elliptically stable fixed point (center) and a hyperbolically unstable fixed point (saddle) come into being. In the special case of a symmetric dimer the location of the bifurcation in phase space coincides with the location of an already existing elliptically stable fixed point such that the bifurcation has the shape of a pitchfork as noted by Zibold et al. (2010).

value, a stable center at $z = 0$, $\phi = \pi$ breaks down into a saddle point point at the same coordinates and a pair of stable centers at $z = \pm\sqrt{1 - \frac{1}{\Lambda^2}}$, $\phi = \pi$. These stable centers, corresponding to a persistent population imbalance between the dimer's two wells, are known as the self-trapping points.

The equations of motion of the Hamiltonian of Equation 2.13 are,

$$\frac{d\phi}{dt} = \frac{\partial H}{\partial z} = \Lambda z + \frac{z}{\sqrt{1 - z^2}} \cos\phi,$$
$$\frac{dz}{dt} = -\frac{\partial H}{\partial \phi} = \sqrt{1 - z^2} \sin\phi.$$

Linearizing these equations about either of the self-trapping fixed point shows that these fixed points are stable centers, with an oscillation frequency of $f = \sqrt{\Lambda^2 - 1}/2\pi$, or in dimensionful units of time,

$$f_{BJJ} = \frac{J}{\hbar} \frac{\sqrt{\Lambda^2 - 1}}{\pi}. \tag{2.14}$$

How accurate is the BJJ model? Both self-trapping (Albiez et al., 2005) and the bifurcation at $\Lambda = 1$ (Zibold et al., 2010) have been observed experimentally. An implicit prediction of the model is that the system remains condensed; this turns out to be accurate for initial conditions near the self-trapping fixed points, but not for ones near the separatrix (Hennig et al., 2012).

2.4 Tunneling between the self-trapping points

Within the BJJ model, the self-trapping fixed points are stable: a trajectory initially sufficiently close to one of them remains close to it for all time. In the full Bose–Hubbard dynamics, however, tunneling between the two self-trapping points occurs with a finite frequency. An example of this process is shown in Figure 2.2, which depicts the Husimi
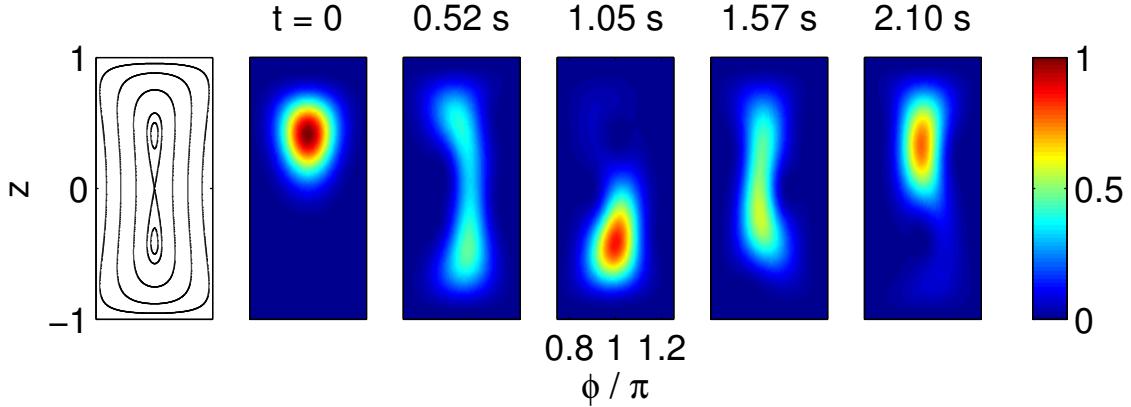
Figure 2.2: Tunneling between the self-trapping fixed points. In the BJJ model, trajectories suffi-ciently close to the self-trapping point remain confined to its neighborhood forever (far left panel). However, as shown in the remaining panels, in the Bose–Hubbard model the Husimi function of a coherent state initially centered at the $z > 0$ self-trapping fixed point tunnels from one fixed point to the other. Parameters: $N = 40$ atoms, with $\Lambda = 1.1$ and $J = 10\,\mathrm{Hz}$.

function (Lee, 1995), a quasiprobability distribution over the coherent states $|z, \phi\rangle$ given

by,

$$Q_\psi(z, \phi) = |\langle z, \phi|\psi\rangle|^2 \tag{2.15}$$

for a pure state $|\psi\rangle$. The Husimi function is initially centered at one of the fixed points, but over time it tunnels to the other, and then back again.

A quantitative signature of the tunneling is an oscillation of the wells' populations. The frequency of this oscillation can be found by numerically integrating the Schrödinger equation of the Bose–Hubbard dimer for a long time and computing the power spectrum of the well populations. The most prominent feature in the spectrum corresponds to the tunneling frequency.

Since the dynamics of the coherent state near the self-trapping fixed points appears very simple, we may try to reduce the dimensionality of the problem by restricting the system to some subspace of the Hilbert space. Remarkably, in the neighborhood of the
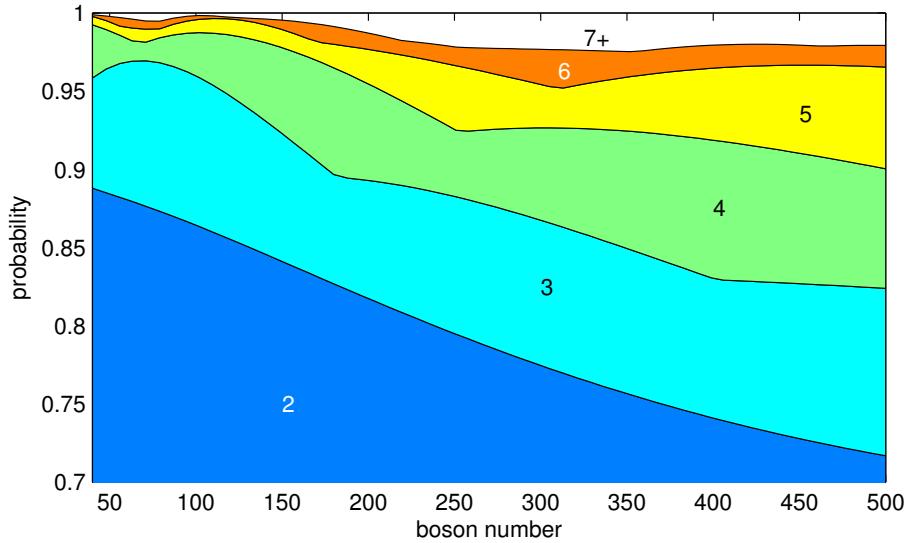
Figure 2.3: The probability of observing the coherent state centered at the self-trapping fixed point in one of the n most probable states, for $n = 2, 3, 4, \ldots$, as a function of the particle number N. ($\Lambda = 1.025$, $U = 2\pi \times 0.063\,\mathrm{Hz}$.)

mean-field fixed points, only a few energy eigenstates contribute appreciably to the coherent state.[4] How many states need to be accounted for depends on the particle number (see Figure 2.3). Our intuition is that as N increases, the "size" of the coherent state in phase space shrinks, but the "size" of the eigenstates shrinks even faster, and ever-more eigenstates are needed to correctly account for the coherent state dynamics. However, even for a few hundred atoms much of the tunneling dynamics can be captured by keeping just two states (see Figure 2.4). At the self-trapping fixed points, these two states are the pair of highest energy states of the Bose–Hubbard model[5]. They are symmetric and antisymmetric combinations of states localized in each well.

The energy splitting between the symmetric and antisymmetric states agrees closely with the oscillation frequency extracted by numerically integrating the Schrödinger equa-

---

[4]This phenomenon will be discussed in greater detail in Chapter 3. See also Chuchem et al. (2010).

[5]The highest energy states are the relevant ones only if Λ is positive. Self-trapped fixed points also exist for $\Lambda \leq -1$, but in this case the relevant states are the two *lowest* energy ones.
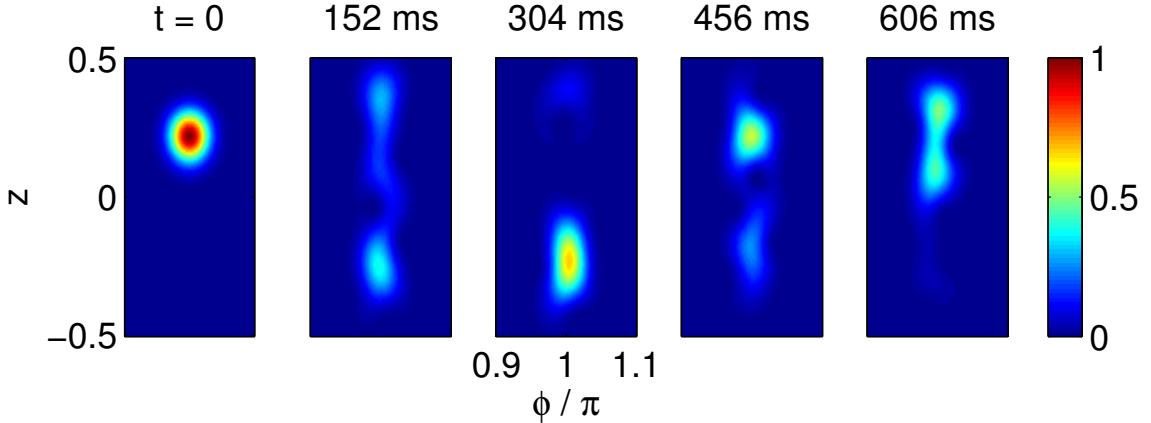
Figure 2.4: A two-state description of the tunneling remains valid as N increases, although the dynamics is more complex as the system becomes less discrete. The Husimi function is shown at the five times spaced by a quarter of the tunneling period expected from the two-state model. ($N = 500$ atoms, $\Lambda = 1.025$ and $U = 2\pi \times 0.063 \, \text{Hz.}$)

tion. The splitting between these states can also be computed for $\Lambda < 1$; in this case, there is only one fixed point at $\phi = \pi$, and the energy splitting closely agrees with the BJJ frequency of oscillations about that point. Both above and below $\Lambda = 1$, the BJJ limit is approached as N is increased (see Figure 2.5).

The energies of the two highest-energy states are easily found numerically even for very large N, but it is desirable to explain the simple trends with N and Λ shown in Figure 2.5 using an analytical model. Quantum perturbation theory can be used to obtain estimates of the tunneling frequency for small $J/U \approx N/\Lambda$ (Bernstein et al., 1990; Salgueiro et al., 2007; Dounas-Frazer et al., 2007), but not in the region $\Lambda \approx 1$ where tunneling becomes a significant effect. In the next section, we will pursue an alternative approach.
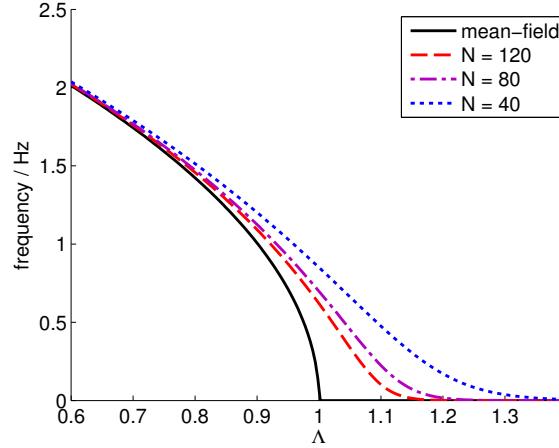
Figure 2.5: The BJJ result of zero tunneling frequency for $\Lambda > 1$ is gradually approached by the two-eigenstate model as the number of atoms increases. Nonetheless, a nonzero frequency is expected for any Λ and any finite N. In all plots, $J = 10\,\mathrm{Hz}$. The mean-field result is that of Equation 2.14.

2.5   Semiclassical quantization

To shed light on the convergence of the results of the two-state model to those of the BJJ, we will start with the BJJ model and recover additional features of the dynamics through Bohr–Sommerfeld quantization. Graefe and Korsch (2007) applied Bohr–Sommerfeld quantization to this problem numerically, obtaining excellent estimates of the eigenenergies even for atom numbers $N < 10$. In this section, we start from their formulation of the quantization condition but proceed analytically to produce accurate closed-form expressions for the tunneling frequency.

The quantization condition in the self-trapping region of the symmetric dimer described by the Hamiltonian of Eq. 2.13 is (Graefe and Korsch, 2007),

$$\sqrt{1 + \kappa^2}\cos(2S_w - S_\phi) = -\kappa. \tag{2.16}$$

Here, $2S_w$ is the action associated with the self-trapped classical orbit, $\kappa = \exp(-\pi S_\epsilon)$,
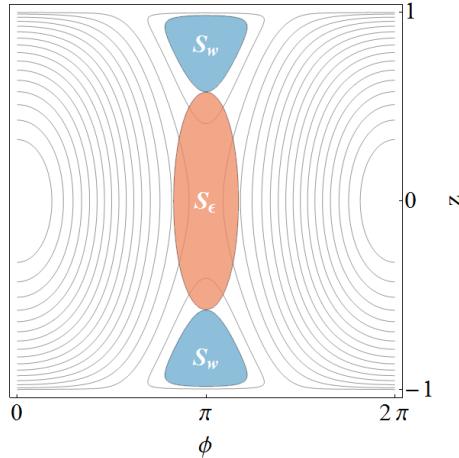
Figure 2.6: The actions appearing in the quantization condition (Eq. 2.16) have a geometric interpretation. This figure depicts the phase space of the BJJ model for $\Lambda = 2$. The grey curves are trajectories; the actions S_w and S_ϵ for energy $E = -1.15$ are equal to the areas of the marked regions. In the case of S_w, the action corresponds to the phase space area of the classical orbit.

and $2S_\epsilon$ is the (Euclidean) action associated with tunneling. Both S_w and S_ϵ are measured in units of Planck's constant, h, and so are dimensionless. [6] The phase correction term S_ϕ can be expressed in terms of S_ϵ as,

$$S_\phi = \arg \Gamma \left(\frac{1}{2} + \iota S_\epsilon \right) - S_\epsilon \ln |S_\epsilon| + S_\epsilon. \tag{2.17}$$

For a discussion of the physical significance of S_ϕ, see Child (1991, pp. 50–51).

The actions S_w and S_ϵ are functions of the energy E and the nonlinearity Λ, and can be expressed as integrals over phase space (see Figure 2.6); this is discussed in greater detail in Appendix B.2.

Let us assume that the energy splitting between symmetric and antisymmetric combinations of states localized in the two self-trapping regions of phase space is small relative to the spacing of allowed energies in each region. As shown in Appendix B.1, in this case

---

[6]The factors of 2 are conventional: the WKB approximation, which inspired this quantization condition, is typically expressed in terms of integrals $\int p \, dx$ between the turning points. But $\int p \, dx = \frac{1}{2} \oint p \, dx = S/2$.
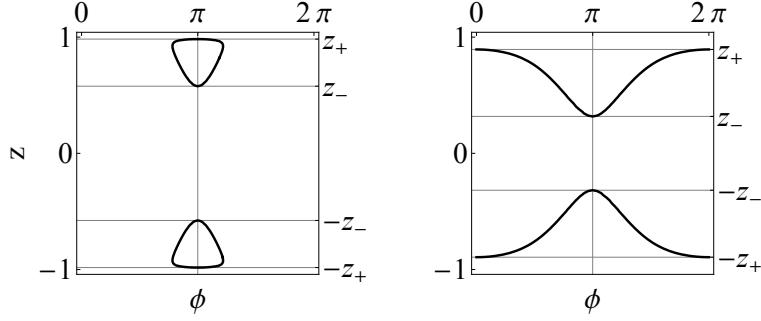
Figure 2.7: Pairs of classical orbits and their turning points $z_\pm$. The orbits on the left ($\Lambda = 2$, $E = 1.15$) are librations, while those on the right ($\Lambda = 4$, $E = 1.15$) are rotations.

the quantization condition implies the splitting is approximately

$$\Delta E = \frac{\hbar\omega}{\pi} \exp(\pi S_\epsilon), \qquad (2.18)$$

where ω is the frequency of the classical motion in a self-trapped orbit (related to the action of the orbit S_w, since $2\pi/\hbar\omega = T/\hbar = 2\partial S_w/\partial E$) and S_ϵ is as before the Euclidean action associated with the tunneling. These quantities depend on the shape and size of the classical orbits, which are determined by Λ and the energy of the unperturbed state E.

Let the classical turning points be $z_\pm$ (see Figure 2.7). The size of the orbits is captured by the dimensionless parameter,

$$k \equiv \sqrt{\frac{z_+^2 - z_-^2}{z_+^2}}. \qquad (2.19)$$

Furthermore, let,

$$k' \equiv \sqrt{1 - k^2} = \frac{z_-}{z_+}, \quad \text{and} \quad \alpha^2 = \frac{z_+^2 - z_-^2}{z_+^2 - 1}.$$

In Appendix B.2 we show that in terms of these quantities the splitting ΔE of the highest-energy state is given by,

$$
\begin{aligned}
\Delta E &= \frac{\hbar \omega}{\pi} \exp(\pi S_\epsilon) \\
&= \frac{\hbar z_+ \Lambda}{2\mathrm{K}(k)} \exp\left(-(N+1)\left(-\left(1 - \frac{2E}{\Lambda}\right)\frac{1}{z_+}\Pi(z_+^{-2}, k') + z_+ \left(\mathrm{K}(k') - \mathrm{E}(k')\right)\right)\right),
\end{aligned}
\tag{2.20}
$$

where K, Π and E are the complete elliptic integrals (Olver et al., 2015, §19.2(ii)), while E is the unperturbed energy of the highest-energy state satisfying the quantization condition,

$$
\frac{\pi}{N+1} - \pi(1 - z_+) \cdot \mathbb{1}\, (E < \Lambda/2) = \left(1 - \frac{2E}{\Lambda}\right)\frac{1}{z_+}\left(\mathrm{K}(k) - \frac{1}{1 - z_+^2}\Pi(\alpha^2, k)\right) - z_+ \mathrm{E}(k), \tag{2.21}
$$

with $\mathbb{1}\,(\cdot)$ denoting the indicator function.

These complicated expressions constitute a solution to the problem of semiclassical quantization but offer little insight into the dimer's behavior. Nonetheless, some of the problem's structure has become apparent:

1. The splitting depends on E and Λ only through the turning points $z_\pm$ and the combination $(1 - 2E/\Lambda)$. The sign of this last quantity distinguishes between the two types of motion depicted in Figure 2.7: $1 - 2E/\Lambda > 0$ for rotations (orbits surrounding one of the poles at $z = \pm 1$) and $1 - 2E/\Lambda < 0$ for librations.

2. The only non-elementary functions in the expressions above are the complete elliptic integrals K, E, and Π. When they do appear they all take the same argument (modulus), either k or k', which is a measure of the size of the classical orbit.

This structure can be exploited to find much simpler expressions for the splitting, valid in the limit of $N \gg 1$.

Let us first rescale the energy through a linear transformation:

$$e = \left(-E + \frac{\Lambda}{2} + \frac{1}{2\Lambda}\right) \cdot \frac{(\Lambda - 1)^2}{2\Lambda}, \tag{2.22}$$

The rescaled energy e lies in $[0, 1)$ for any orbit in the self-trapping region. The highest-energy state orbit has an area $h/2$, while the total semiclassical action of a dimer with N particles is $h(N + 1)$. As N increases, both the energy e of the highest-energy state and the dimensionless measure of orbit size k (Equation 2.19) become small. If the highest-energy state orbit is a libration ($e < (\Lambda - 1)^{-2}$), expanding Equation 2.21 to lowest order in k and e and solving for e gives an estimate of the energy of the highest-energy state,

$$e \approx \frac{2\Lambda\sqrt{\Lambda^2 - 1}}{(\Lambda - 1)^2(N + 1)}. \tag{2.23}$$

This estimate is very good: the relative error in approximating the numerical semiclassical result is less than 1% for $N = 20$ and $\Lambda = 1.25$, and decreases with both N and Λ. Analogous expansions for the classical orbital frequency and the tunneling phase lead to the following expression for the ground state splitting:

$$\Delta E \approx 2J\frac{\omega}{\pi} \left(\frac{1}{\omega}e^{-z_0}\right)^{(N+1)(1-e)}, \tag{2.24}$$

where $z_0 \equiv \sqrt{1 - \frac{1}{\Lambda^2}}$ is the position of the self-trapping fixed point and $\omega = \sqrt{\Lambda^2 - 1}$ is the frequency of motion about it. The tunneling frequency $\Delta E/\hbar$ decreases exponentially with the "barrier width" $\approx z_0$, the "barrier height" $\approx (1 - e)$ and the number of atoms N. The details of the calculation are described in Appendix B.3.

Figure 2.8 compares the semiclassical splitting estimates with the results of exact diagonalization of the Bose–Hubbard model. The results of solving the quantization problem
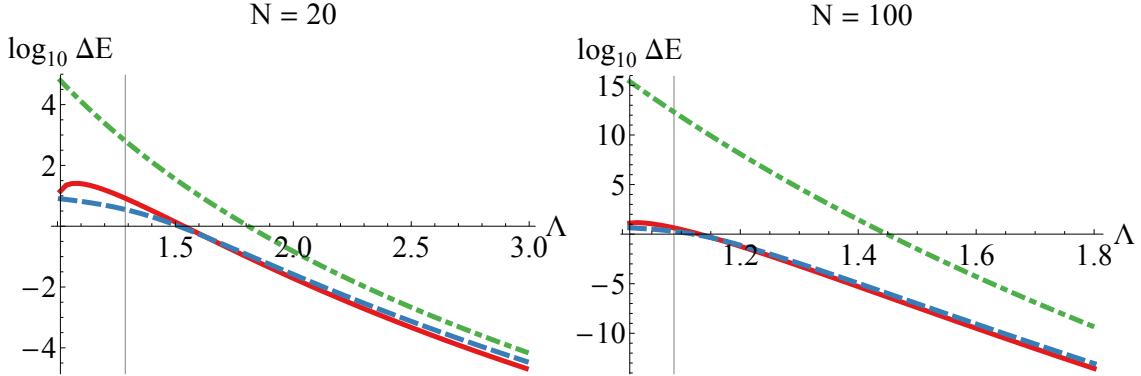
Figure 2.8: Comparison of semiclassical estimates of the splitting with exact diagonalization. The analytical approximation of Equation 2.24 (red line) agrees closely with the results of exact diagonalization (blue dashed line). In contrast, the approximation of Scharf et al. (1987), drawn with a green dot-dashed line performs poorly in this low-Λ regime, especially for larger N. The black vertical line marks the Λ value below which the semiclassical approximation breaks down because the area of phase space associated with the self-trapped region is less than $h/2$.

numerically are not shown: except for Λ so small that not even one semiclassical orbit fits within the self-trapping region, they agree very closely with the exact Bose–Hubbard splitting. The analytic approximation discussed in this section is generally within a factor of 2 of the exact result, and improves with N. Since the splitting changes by as many as 15 orders of magnitude over the investigated range of Λ, this agreement amounts to remarkably robust performance.

A different closed-form semiclassical approximation to ΔE was obtained by van Hemmen and Sütö (1986) and refined by Scharf et al. (1987). This last approximation attains an excellent accuracy, on the order of a few percent, but only for $U \approx J$. In the context of cold atomic experiments, in which the atom number is on the order of hundreds, this corresponds to very small tunneling frequencies (well below 10^{-100} Hz). For $U \ll J$, where the tunneling frequency becomes large, the approximation of Scharf et al. (1987) is many orders of magnitude from the true value (see Figure 2.8). Therefore, the approximation we provide in Equation 2.24 is the first closed-form expression valid in the

experimentally-relevant regime.

2.6   Applications

In this section, we consider the implications of the analysis presented above for three problems: determining the time scale for macroscopic entanglement, producing quantum speedup of dissipation, and obtaining experimental confirmation.

2.6.1   Time scale for macroscopic entanglement

Tunneling in the self-trapping regime leads to the generation of entangled superpositions of many-particle states, or macroscopic entanglement (Carr et al., 2010). The entanglement between the two modes is maximized at times $T/4$ and $3T/4$, where T is the tunneling period. Therefore, our semiclassical estimate of the tunneling frequency immediately yields an estimate of the time required for entanglement generation. It is notable that the dynamics of entanglement, a profoundly unclassical phenomenon, is captured by the first quantum correction to the (classical) BJJ model.

2.6.2   Quantum speedup of dissipation

So far we have considered only an isolated Bose–Hubbard dimer. In this section we briefly discuss the central role tunneling in the self-trapped regime plays in a quantitatively accurate model of a dissipative dimer that leaks atoms to the environment.[7]

Consider a coherent state of N bosons centered at one of the self-trapping fixed points, say the left well. We will attempt to model its dynamics within a two-dimensional subspace of the full system's Hilbert space, the subspace spanned by the symmetric and antisymmetric energy eigenstates, $|E_S\rangle$ and $|E_A\rangle$. In the basis of states localized in the two

---

[7]For a discussion of the effect of dissipation at large nonlinearities $UN/2J \gg 1$, when the tunneling becomes slow and is dominated by other effects, see the next chapter.

wells, $|1\rangle = (|E_S\rangle + |E_A\rangle)/\sqrt{2}$ and $|2\rangle = (|E_S\rangle - |E_A\rangle)/\sqrt{2}$, the Hamiltonian is represented by the matrix,

$$\begin{pmatrix} \bar{E} & \Delta E \\ \Delta E & \bar{E} \end{pmatrix}$$

where $\bar{E} = (E_S + E_A)/2$ and $\Delta E = (E_S - E_A)/2$. These parameters can be calculated semi-classically with high accuracy as we have shown in the preceding section (Equation 2.23 and Equation 2.24), though we use exact values in the simulation discussed below. The initial condition is the localized state $|1\rangle$. Now, assume there is decay from the right well at a rate γ. In the two-level model this is described by the effective decay rates,

$$\Gamma_1 = -\gamma \langle 1| \hat{a}_2^\dagger \hat{a}_2 |1\rangle, \quad \Gamma_2 = -\gamma \langle 2| \hat{a}_2^\dagger \hat{a}_2 |2\rangle,$$

leading to the effective Hamiltonian,

$$H_{\text{eff}}^{(2)} = \begin{pmatrix} \bar{E} - \imath\Gamma_1/2 & \Delta E \\ \Delta E & \bar{E} - \imath\Gamma_2/2 \end{pmatrix}. \tag{2.25}$$

This simple model can be used to estimate how the probability of all N atoms remaining in the system diminishes over time. To evaluate the results, we compare them to those obtained using the complete coherent state and the full master equation of Section 1.4.1,

$$\dot{\rho} = -\imath[\hat{H}, \hat{\rho}] - \frac{\gamma}{2} \left(\hat{a}_1^\dagger \hat{a}_1 \hat{\rho} + \hat{\rho}\hat{a}_1^\dagger \hat{a}_1 - 2\hat{a}_1 \hat{\rho}\hat{a}_1^\dagger \right). \tag{2.26}$$

The probabilities of remaining in the N atom subspace predicted using the two Hamiltonians are shown in Figure 2.9. If many-body tunneling between the fixed points is neglected ($\Delta E = 0$), the rate of atom loss is significantly underestimated. But when the correct value of ΔE is used, the effective two-state model produces results almost indis-
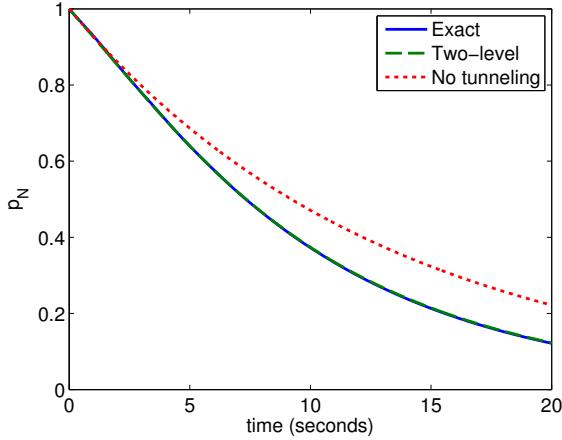
Figure 2.9: Correctly estimating the rate of tunneling between the self-trapping fixed points is critical to predicting the atom loss rate from a leaky dimer. The probability of finding all N atoms in the system over time is plotted for three different models. The dashed green line is the simple Hamiltonian of Equation 2.25, based only on two parameters $\bar{E}$ and ΔE which can be calculated semiclassically. It overlaps with the numerically exact results obtained by integrating the many-body master equation of Equation 2.26 (solid blue line). The simple model with ΔE set to zero differs significantly (dotted red line). ($J = 1\,\text{Hz}$, $U = 4/5\,\text{Hz}$, $N = 6$)

tinguishable from the full Bose–Hubbard. Remarkably, we can thus reproduce the decay dynamics of a correlated many-body system using only two parameters, $\bar{E}$ and ΔE, which can be calculated semiclassically.

2.6.3 Prospects of experimental observation

The BJJ dynamics of the BEC dimer was experimentally mapped out in great detail a few years ago by Zibold et al. (2010). Could a similar experiment observe tunneling between the fixed points for $\Lambda > 1$?

As we mentioned in Section 1.3.2, experimental realizations of the dimer fall into two categories: "external" and "internal" (Leggett, 2001), or those utilizing two spatially separated wells and those using two internal states of atoms. Correctly describing the dynamics of the spatially separated wells requires going beyond the Bose–Hubbard model
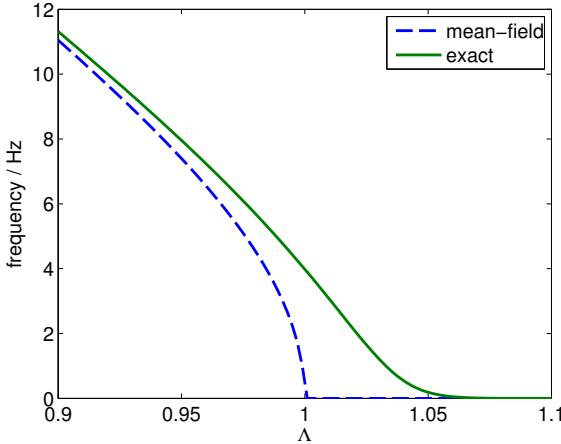
Figure 2.10: Frequency of tunneling between the fixed points versus Λ for $U = 2\pi \times 0.063$ Hz and $N = 500$, the experimental parameters of Zibold et al. (2010). The mean-field prediction is also shown for reference.

that was our starting point in this work, as the localized orbitals associated with the operators $\hat{a}_i$, $\hat{a}_i^\dagger$ are time-dependent Sakmann et al. (2009). Fortunately, this complication does not arise in the case of internal states (Zibold, 2012). Therefore, the tunneling and dissipation enhancement effects we have described are most likely to be observed in experiments relying on internal states.

The expected tunneling frequency given the experimental parameters of Zibold et al. (2010) is shown in Figure 2.10. The frequency is on the order of a few Hertz. Since the atom decay times reported in this experiment are $\sim$ 100 ms, the tunneling frequency is too small to be observed at present. However, an order of magnitude improvement in atom retention times would render experimental observation feasible.

At first glance, it may seem that the retention time limitation could be sidestepped by lowering both N and J by the same factor. Since the quantum tunneling time depends on N exponentially, but on J only linearly (Equation 2.24), this could speed up the semiclassical dynamics while keeping Λ constant. Unfortunately, the experiment of Zibold et al. (2010) was already carried out at the lowest J currently accessible: lowering it even more

introduces unacceptable noise due to electromagnetic fluctuations. [8]

2.6.4   Beyond the dimer: semiclassical quantization for lattices

Although our analysis was limited to the dimer, analogous processes should occur in a system with multiple states, only one of which has an appreciable population. The Bose–Hubbard Hamiltonian can be straightforwardly extended to such systems; in the case of the trimer, self-trapping has been demonstrated in both the quantum model and its classical limit (Mossmann and Jung, 2006; Hennig et al., 2010). However, carrying out semiclassical quantization is difficult because the classical model is now chaotic. So far, progress has only been made for the case of very small and very large J/U (Itin and Schmelcher, 2011), i.e. precisely the region of parameter space where tunneling between the self-trapping points does not take place. Therefore, the extension of our results beyond the dimer is likely to prove challenging.

2.7   Summary & Outlook

In this chapter we have studied the tunneling between the self-trapped fixed points of the BEC dimer using a semiclassical approach. We derived an exact solution to the problem in terms of elliptic integrals giving the phase space areas of semiclassical orbits. For particle numbers $N \gg 1$, the semiclassical ground state orbit and (appropriately transformed) energy become small; in this limit we found an approximate closed-form expression for the tunneling frequency that is accurate in the experimentally relevant parameter range. The tunneling frequency decreases exponentially with the effective width and height of barriers in phase space, as well as the number of particles. Nonetheless, accounting for the tunneling is crucial to obtaining quantitatively accurate estimates of atom loss rates

---

[8]We thank Wolfgang Muessel for private communication on this point.

in a leaky dimer.

Chapter 3

Dynamics near the self-trapping fixed points of the Bose–Hubbard dimer

In the previous chapter, we investigated corrections to the mean-field dynamics of the Bose–Hubbard dimer when the nonlinearity is relatively weak, $UN/2J \gtrsim 1$. In this chapter, we focus on the regime of stronger nonlinearity, when tunneling no longer plays an important role. We study the connection between the semiclassical phase space and inherently quantum phenomena such as entanglement and dissipation-induced coherence. Near the semiclassical self-trapping fixed points, the dynamics of EPR entanglement and condensate fraction consists of beats among just three eigenstates. Since persistent EPR entangled states arise only in the neighborhood of these fixed points, our analysis explains essentially all of the entanglement dynamics in the system. We derive accurate analytical approximations by expanding about the strong-coupling limit; surprisingly, their realm of validity is nearly the entire parameter space for which the self-trapping fixed points exist. Finally, we show significant enhancement of entanglement can be produced by applying localized dissipation.

This chapter is partially based on work published as Pudlik et al. (2013).

3.1 Entanglement and coherence

In addition to the expectation values $\langle z \rangle$ and $\langle \phi \rangle$ studied in the previous chapter, we will investigate the dynamics of two quantities that do not have a mean-field counterpart. The first is the *condensate fraction* or purity, defined as the largest eigenvalue of the single-particle density matrix,

$$\rho = \begin{pmatrix} \langle \hat{a}_1^\dagger \hat{a}_1 \rangle & \langle \hat{a}_1^\dagger \hat{a}_2 \rangle \\ \langle \hat{a}_2^\dagger \hat{a}_1 \rangle & \langle \hat{a}_2^\dagger \hat{a}_2 \rangle \end{pmatrix}.$$

The condensate fraction measures how close the many-body state is to a pure BEC (Witthaut et al., 2008; Trimborn et al., 2009). The second quantity of interest is the observable introduced by Hillery and Zubairy (2006); He et al. (2011),

$$\text{EPR} = \langle \hat{a}_1^\dagger \hat{a}_2 \rangle \langle \hat{a}_2^\dagger \hat{a}_1 \rangle - \langle \hat{a}_1^\dagger \hat{a}_1 \hat{a}_2^\dagger \hat{a}_2 \rangle. \tag{3.1}$$

This observable quantifies the entanglement between the two modes of the dimer: the modes are said to be EPR-entangled whenever EPR > 0. This entanglement criterion has two advantages: it is experimentally accessible, and applies to dissipative as well as closed systems.

Although these quantities have no mean-field analogs, prior work (Hennig et al., 2012) showed a strong influence of the mean-field phase portrait on their dynamics. Specifically, the condensate fraction remains large near all of the stable fixed points while EPR entanglement is found only near the $z \neq 0$ fixed points (see Figure 3.1).

This so-called "global phase space picture" suggests a new method for generating EPR entanglement in the Bose–Hubbard dimer: driving the system closer to the mean-field fixed points using controlled atom loss. Since the mean-field dynamics is particularly simple near the fixed points, one might hope the full quantum dynamics to be simple as
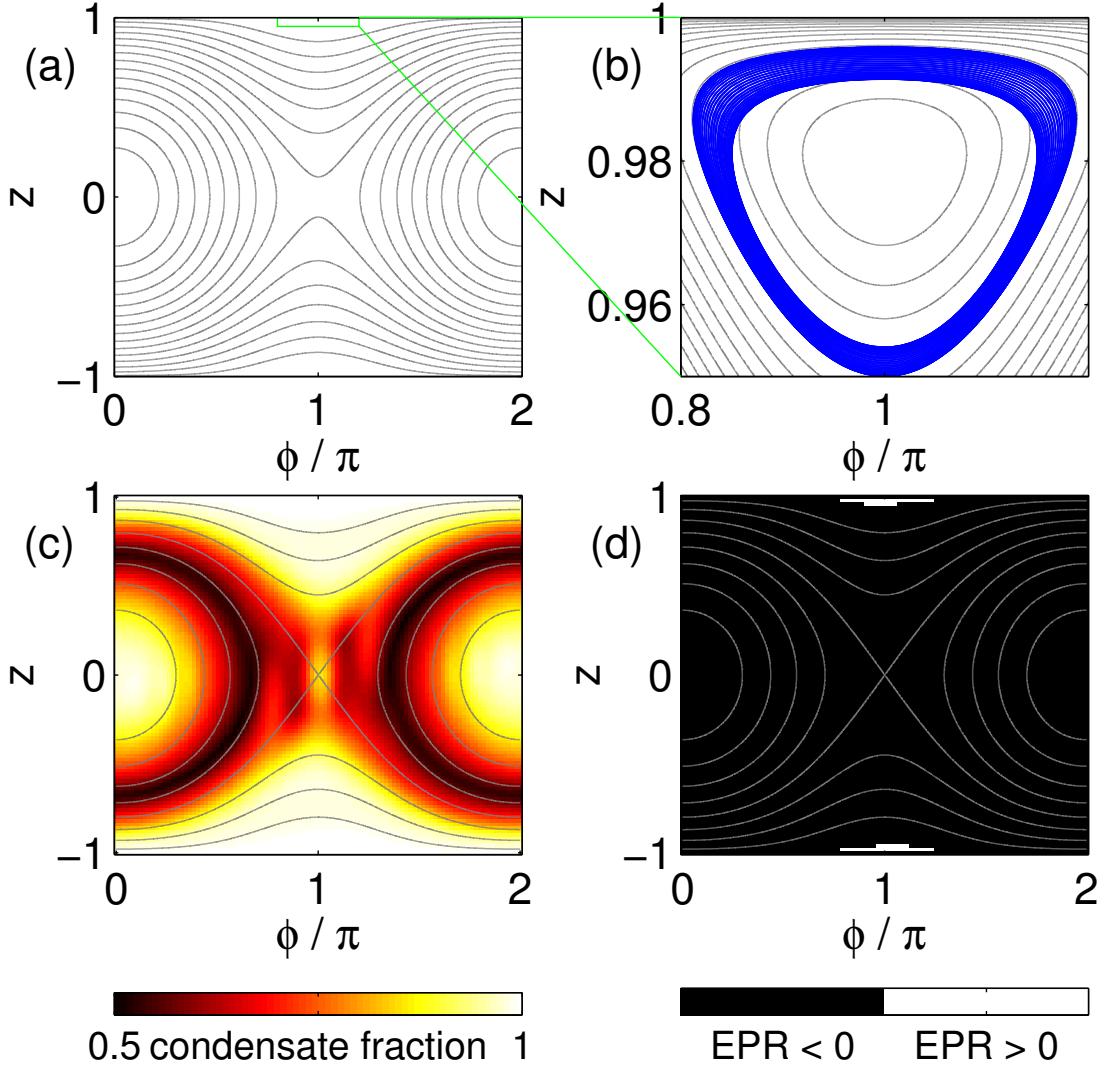
Figure 3.1: The global phase space picture of the BEC dimer. **(a)** Mean-field trajectories. **(b)** The expectation values of z and ϕ over time (phase space trajectory) for an initially coherent state close to the stable fixed point. The phase trajectory is drawn in blue; nearby mean-field trajectories are in grey. Note that the actual trajectory has a "thickness" associated with it—a phenomenon beyond the mean-field description. **(c)** The condensate fraction after 1 second of evolution, for initially coherent states uniformly sampled in z and ϕ: condensate fraction remains high for initial conditions in the neighborhood of the stable fixed points. **(d)** EPR entanglement for initially coherent states after 1 second of evolution: the only states still EPR entangled are those initially very near the self-trapping fixed points. All plots are for $N = 40$, $J = 10\,\hbar/\text{s}$ and $U = 100/39 \approx 2.6\,\hbar/\text{s}$, so $\Lambda \approx 5.3$.
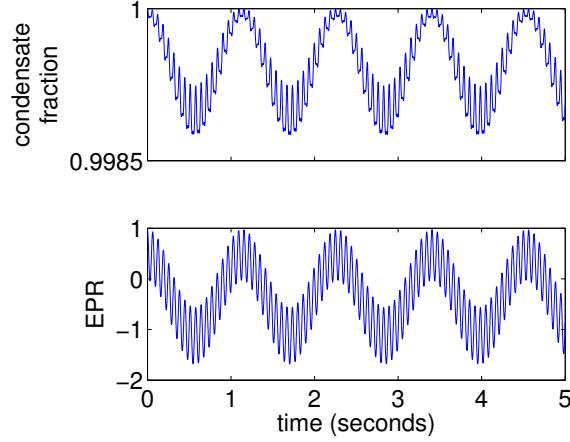
Figure 3.2: The condensate fraction and EPR entanglement over time for an initially coherent ($z = 0.95$, $\phi = \pi$) state of the Bose–Hubbard dimer with $N = 40$, $J = 10\,\hbar/\text{s}$ and $U = 100/39 \approx 2.6\,\hbar/\text{s}$, so $\Lambda \approx 5.3$. The stable fixed point is at $z \approx 0.98$, $\phi = \pi$. Results obtained by numerical integration of the Schrödinger equation.

well, allowing for a clear yet quantitative understanding. To develop such an understanding, in Section 3.2 we describe the full quantum dynamics of the Bose–Hubbard dimer near the mean-field fixed points, and in Section 3.3 consider the effects of controlled atom loss on this dynamics.

3.2 Dynamics near the self-trapped fixed points

Let us consider the behavior of the system near the self-trapping fixed points, located at $z = \pm\sqrt{1 - 1/\Lambda^2}$, $\phi = \pi$. In their neighborhood the observables defined in the previous section exhibit peculiar dynamics, the most striking feature of which is the presence of two distinct frequencies (see Figure 3.2).

The higher frequency is expected on the basis of the bosonic Josephson junction model of Section 2.2. Recall that linearizing the equations of motion obtained from the
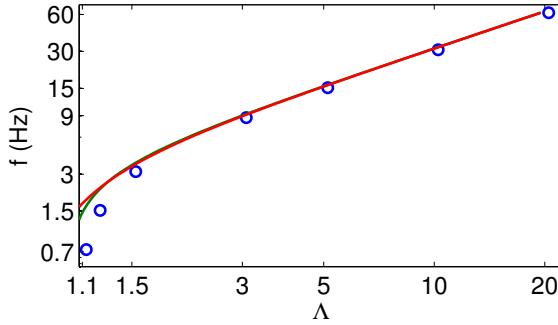
Figure 3.3: The high frequency observed near the fixed point for different values of Λ (blue circles), on a log-log scale. The mean-field prediction (green line) is consistent with the numerically exact results. The $O(\Lambda^{-2})$ perturbative result (show in red) agrees with the mean-field down to $\Lambda = 1.5$, below which it overestimates the frequency; see Section 3.2.2 for a discussion.

Hamiltonian of Equation 2.13 about the fixed point yields (cf. Equation 2.14),

$$f_{\text{BJJ}} = \frac{\sqrt{\Lambda^2 - 1}}{\pi} \frac{J}{\hbar}. \tag{3.2}$$

This mean-field prediction works for a broad range of Λ (see Figure 3.3). The lower frequency, however, cannot be explained within the BJJ approximation. To see this, consider the trajectory of the system in z, ϕ space (see Figure 3.1(b)). In the BJJ model, this trajectory is expected to coincide with an energy contour of the Hamiltonian. However, simulation of the full quantum dynamics reveals a "thick" orbit, the size of which oscillates with the low frequency.[1]

---

[1]Similar low frequency phenomena were noted before by Milburn et al. (1997), but not discussed quantitatively.

3.2.1 Eigenstate decomposition

To explain the low frequency oscillations, let us decompose the evolving quantum state into the energy eigenstates:

$$|\psi(t)\rangle = \sum_{n=0}^{N} a_n\, e^{-\imath E_n t/\hbar}\, |E_n\rangle. \tag{3.3}$$

At first glance, this decomposition does not offer much insight, as the Hamiltonian has a large number of eigenstates and their energies can only be found numerically. However, in the neighborhood of the system's fixed points only a few states contribute appreciably to the wave function (see Figure 3.4). This is not entirely surprising: the stable fixed points are the extrema of the mean-field energy, so in the neighborhood of these points only the eigenstates with most nearly extremal energy values should contribute to the coherent state. Indeed, for the $z = 0.95$, $\phi = \pi$ coherent state of Figure 3.2, we find the contributions of the three highest-energy eigenstates to be,

$$a_0 = 0.9353 \qquad\qquad E_0 = 2040\,\hbar/s$$

$$a_1 = 0.3474 \qquad\qquad E_1 = 1942\,\hbar/s$$

$$a_2 = 0.0653 \qquad\qquad E_2 = 1850\,\hbar/s.$$

These three eigenstates together account for,

$$|a_0|^2 + |a_1|^2 + |a_2|^2 = 0.9997$$
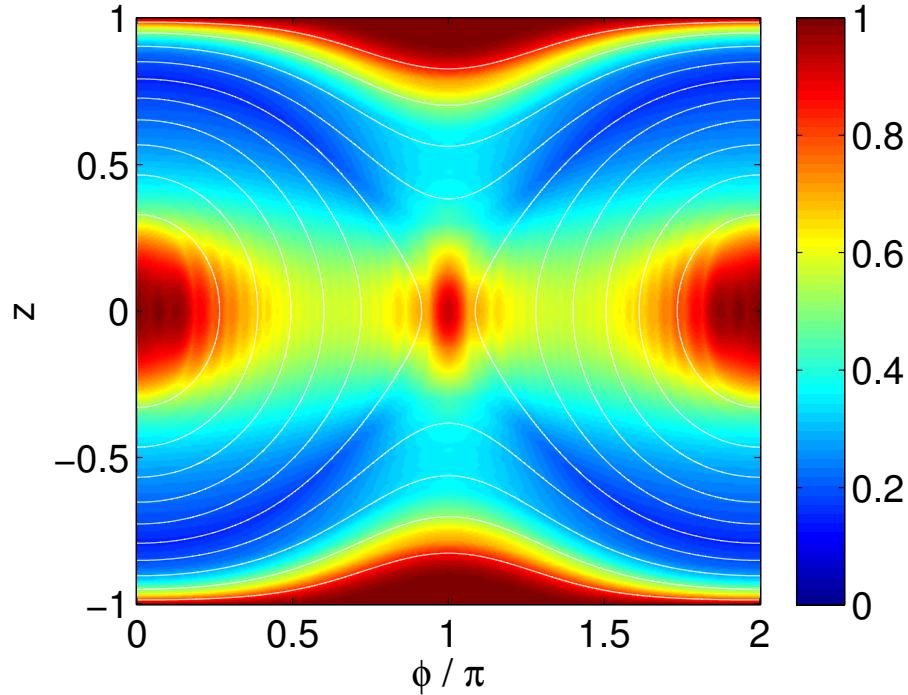
Figure 3.4: A projection onto just 3 eigenstates is effective near the BJJ fixed points. Consider a coherent state $|z, \phi\rangle = \sum_{n=0}^{N} a_n |E_n\rangle$ and its projection $|\psi'\rangle = \sum_{n=0}^{2} a_n |E_n\rangle$ onto the three energy eigenstates with the largest coefficients a_n in the energy eigenstate expansion. The plot above shows the norm $|\langle \psi'|\psi'\rangle|^2$ of this projection as a function of z and ϕ. Note that the norm of the projection is nearly 1 (perfect) near all of the fixed points, including the unstable one, suggesting the three-eigenstate description will be informative for those initial conditions. The system parameters are the same as those in Figure 3.2, namely $J = 10\,\hbar/s$, $\Lambda \approx 5.3$ and $N = 40$. The mean-field stable fixed points are at $z = 0$, $\phi = 0$ and at $z = \pm 0.98$, $\phi = \pi$, while the unstable fixed point is at $z = 0$, $\phi = \pi$. Contours of constant mean-field energy are shown in white.

of the probability weight of the coherent state. We might therefore expect the frequencies
observed in the data to be beats between the eigenstates,

$$(E_0 - E_1)/2\pi = 15.56\,\text{Hz} \equiv f_{\text{fast}}$$

$$(E_1 - E_2)/2\pi = 14.64\,\text{Hz}$$

$$(E_0 - E_2)/2\pi = 30.23\,\text{Hz}$$

or perhaps higher-order beats, such as

$$\frac{E_0 - E_1}{2\pi} - \frac{E_1 - E_2}{2\pi} = 0.8805\,\text{Hz} \equiv f_{\text{slow}}.$$

These expectations are borne out: $16.4\,\text{Hz} \approx f_{\text{fast}}$ is the BJJ frequency given by Eq. 3.2,[2]
while $0.85(5)\,\text{Hz}$ is the measured frequency of the large-amplitude oscillation in Fig-
ure 3.2. The two other beats are also seen in the power spectrum of the condensate
fraction (at $14.65(5)\,\text{Hz}$ and $30.27(5)\,\text{Hz}$), though not in that of EPR.

The projection onto the three most important eigenstates recovers not only the fre-
quencies but essentially all of the observables' dynamics (see Figure 3.5). A projection
onto just two states is sufficient to recover the mean-field motion, but not the low fre-
quency oscillations.

---

[2]The 5% discrepancy between the BJJ frequency and the fast frequency observed in the data will be
discussed in the next section.
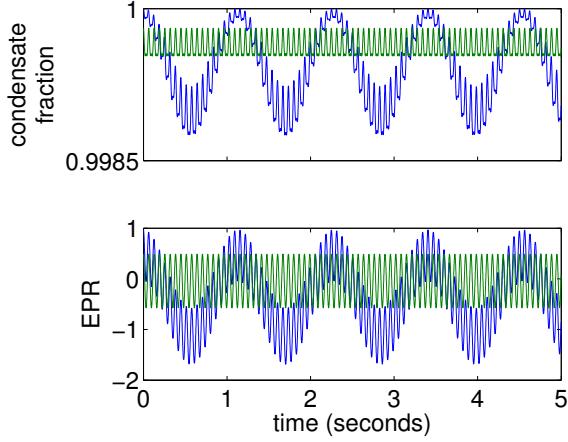
Figure 3.5: Validity of the two-frequency approximation. The condensate fraction and EPR entanglement calculated by approximating the initial coherent state with only 3 eigenstates (blue) is virtually indistinguishable from the numerically exact results shown in Figure 3.2. An approximation with only 2 eigenstates (green) reproduces the fast, but not the slow oscillations.

3.2.2 $J \to 0$ limit

To gain more insight into the two frequencies, consider the limit $J \to 0$ in which the Hamiltonian can be diagonalized exactly [3]. The eigenstates are the Fock states,

$$|N_1, \, N - N_1\rangle \equiv |N_1\rangle,$$

and the associated energies are,

$$\epsilon_{N_1} = \frac{N_1(N_1 - 1)}{2}U + \frac{(N - N_1)(N - N_1 - 1)}{2}U, \tag{3.4}$$

which we denote with ϵ rather than E to distinguish the $J \to 0$ limit from the general case. Note the $N_1 \to N - N_1$ twofold degeneracy of the spectrum, reflecting the symmetry

---

[3]Strictly speaking, the Bose–Hubbard dimer can be analytically solved in the $J \neq 0$ case: a solution based on the Bethe ansatz was developed in the early 1990s (Enol'skii et al., 1991, 1992; Links et al., 2003; Links, 2006). This solution replaces the $N + 1$ dimensional eigenvalue problem with a set of N nonlinear algebraic equations. Since for generic N such equations can only be solved numerically, the Bethe ansatz solution amounts to a restatement of our original problem.

of the system with respect to a relabeling of the wells. The frequencies analogous to f_{fast} and f_{slow} computed numerically in Section 3.2.1 are,

$$\frac{\epsilon_0 - \epsilon_1}{2\pi\hbar} = \frac{U(N-1)}{2\pi\hbar} \approx 15.9\,\text{Hz},$$

$$\frac{\epsilon_0 - \epsilon_1}{2\pi\hbar} - \frac{\epsilon_1 - \epsilon_2}{2\pi\hbar} = \frac{U}{\pi\hbar} \approx 0.82\,\text{Hz}.$$

The $J \to 0$ estimate of f_{fast} coincides with the limit of the BJJ expression, up to a multiplicative factor of $(N+1)/(N-1)$ that leads to discrepancies for small N:

$$
\begin{aligned}
f_{\text{BJJ}} &= \frac{\sqrt{\Lambda^2-1}}{\pi}\frac{J}{\hbar} = \frac{\sqrt{U^2(N+1)^2-4J^2}}{2\pi\hbar} = \frac{U(N+1)}{2\pi\hbar}\sqrt{1-\left(\frac{2J}{U(N-1)}\right)^2} \\
&= \frac{U(N-1)}{2\pi\hbar}\frac{N+1}{N-1}\left[1-\frac{1}{2}\Lambda^{-2}+O(\Lambda^{-4})\right].
\end{aligned}
\tag{3.5}
$$

More interesting is $f_{\text{slow}} = U/\pi\hbar$. The slow oscillations are a purely quantum phenomenon, as $U/\pi\hbar$ goes to zero in the classical limit of $N \to \infty$ with $\Lambda = U(N+1)/2J$ fixed. A first hypothesis might identify them with the quantum revivals, in which *all* of the components of the coherent state re-phase (Greiner et al., 2002b). This is almost correct. Consider an initial state $|\psi(0)\rangle$ decomposed into energy eigenstates (Equation 3.3). Evolving the state over one period $\tau = 1/f_{\text{slow}}$ of the slow oscillation yields,

$$
|\psi(\tau)\rangle =
\begin{cases}
\sum_{n=0}^{N} a_n\,|n\rangle & \text{for } N \text{ odd,} \\
\sum_{n=0}^{N} (-1)^n a_n\,|n\rangle & \text{for } N \text{ even,}
\end{cases}
\tag{3.6}
$$

up to an overall phase (see Appendix C.1 for a proof). For odd N, we observe a full revival, as expected. For N even, the relative phases of the eigenstates are altered, and a revival occurs only after a translation by 2τ. However, the additional phases present after a τ translation cancel when the condensate fraction and EPR are computed (see
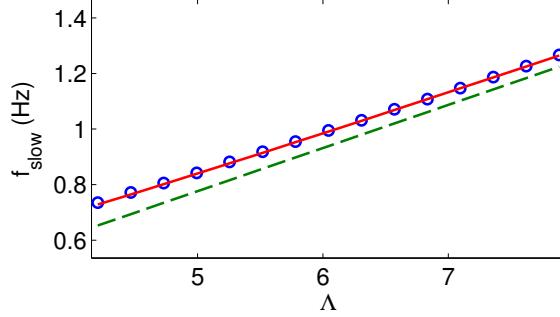
Figure 3.6: The slow frequency near the fixed point as a function of Λ. The numerically exact values (blue circles) are well described by the second order perturbative results (solid red line). Zeroth-order perturbation theory (dashed green line) slightly underestimates the frequency.

Appendix C.2 for a proof). In the limit $J \rightarrow 0$ one therefore expects revivals in these observables with a frequency $1/\tau = \frac{U}{\pi\hbar}$ for all values of N.

Surprisingly, the $J \rightarrow 0$ result is close to the observed frequencies even when $J \gg U$ (see Figure 3.6). To shed light on this, one may compute the shifts in the frequencies due to $J \gtrsim 0$ using degenerate perturbation theory; see Appendix C.3 for a derivation following Bernstein et al. (1990). The resulting corrections to the $J = 0$ result are proportional to Λ^{-2}:

$$
\begin{aligned}
\frac{\epsilon_0 - \epsilon_1}{2\pi\hbar} &= \frac{U(N-1)}{2\pi\hbar}\left[1 - \frac{1}{2}\frac{(N+1)^3}{(N-1)^2(N-3)}\Lambda^{-2} + O(\Lambda^{-4})\right], \\
\frac{\epsilon_0 - \epsilon_1}{2\pi\hbar} - \frac{\epsilon_1 - \epsilon_2}{2\pi\hbar} &= \frac{U}{\pi\hbar}\left[1 + \frac{3}{2}\frac{(N+1)^3}{(N-5)(N-3)(N-1)}\Lambda^{-2} + O(\Lambda^{-4})\right].
\end{aligned}
\tag{3.7}
$$

The perturbative high frequency estimate agrees with the mean-field result (Equation 3.5) in the limit of large N, as one would expect. Close to the bifurcation the mean-field expression performs better than the perturbative one (see Figure 3.3), presumably because we dropped terms of order Λ^{-4} and higher. But above $\Lambda \approx 2$, the agreement of the perturbative expressions with the observed frequencies of both the mean field motion (Figure 3.3) and the quantum revival (Figure 3.6) is excellent.

3.2.3   Region of validity

How far from the fixed point can we expect the dynamics to be dominated by the two-frequency pattern described above? To avoid introducing additional frequencies at the outset, the initial coherent state $|z, \phi\rangle$ must have an appreciable projection onto just three eigenstates: that is, the projection $|\psi'\rangle = \sum_{n=0}^{2} a_n |E_n\rangle$ must satisfy $\|\langle z, \phi|\psi'\rangle\|^2 = \|\langle \psi'|\psi'\rangle\|^2 \approx 1$. But in addition, coherent states at every point of the the mean-field trajectory must be well approximated by the three eigenstates: if $\|\langle z, \phi|\psi'\rangle\|^2$ deviates significantly from 1 anywhere along an orbit, a breakdown of the two-frequency pattern is expected. An instructive example of such a breakdown is observed as the system approaches the bifurcation ($\Lambda \rightarrow 1_+$). Although in the neighborhood of the stable fixed points the norm of the three-eigenstate projection remains high, the orbits of the BJJ model venture out of this neighborhood (see Figure 3.7). The true quantum dynamics involves tunneling from one stable fixed point to the other described in Chapter 2 which is classically forbidden and does not conform to the two-frequency paradigm described in this section.

Thus, the two-frequency description is valid only for initial conditions in some neighborhood of the stable fixed points. However, this is generally sufficient to understand the generation of EPR entanglement: On long time scales EPR entanglement is present only for initial conditions close to the fixed points, as shown in Figure 3.1.

What is more, the slow oscillations set the timescale for which EPR entanglement is present in the sysem. To obtain a global picture of entanglement generation, we simulated the dynamics of 10,000 initially coherent states uniformly sampled from the Bloch sphere. In Figure 3.8 we plot, as a function of time, the fraction of these in which the two wells are entangled. Pronounced revivals occur with the frequency f_{slow} analyzed above. The implication, supported by an examination of individual phase space trajec-
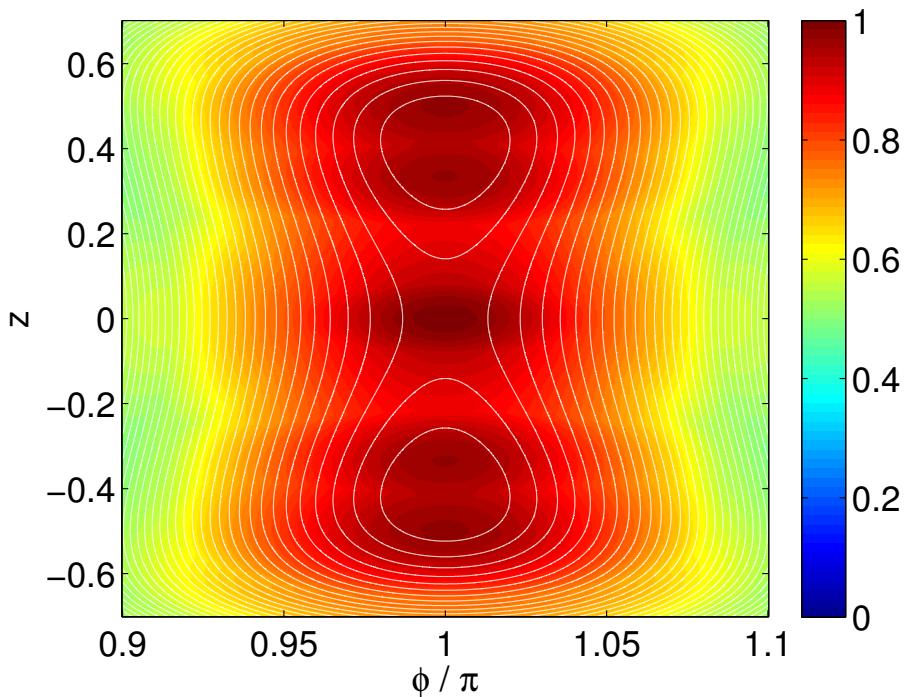
Figure 3.7: Breakdown of the three-eigenstate approximation near the bifurcation. The squared norm $\|\langle\psi'|\psi'\rangle\|^2$ of the projection of coherent states onto the three energy eigenstates with the largest coefficients in the energy eigenstate expansion is plotted, for $\Lambda = 1.1$. The mean-field trajectories are overlaid in white. Note that the projection norm is not conserved along the mean-field trajectories, indicating the breakdown of the mean-field approximation and the two-frequency pattern.
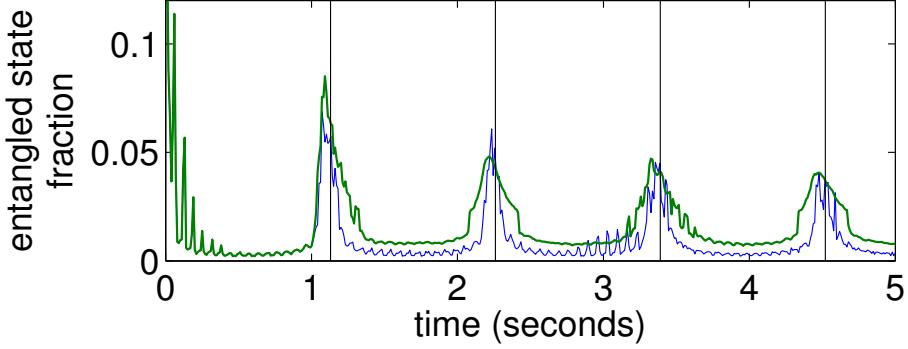
Figure 3.8: EPR entanglement is predominatly found at the quantum revival times and can be promoted by applying localized dissipation. We plot the fraction of coherent state initial conditions for which the two wells are EPR entangled (EPR > 0), as a function of time for $\Lambda = 5.3$. The initial conditions are uniformly sampled on the Bloch sphere. The quantum revival times near the fixed point (multiples of $\tau = 1.13\,\text{s}$) are marked with black vertical lines. The thin blue line is obtained in the absence of dissipation; the thick green line is the result seen when atom loss at the second site is induced between seconds 1 and 1.25 of the simulation. Applying dissipation increases the fraction of initial conditions for which the wells are persistently entangled.

tories, is that entanglement is only observed in those regions of phase space where its dynamics is dominated by the two-frequency behavior. In this sense, the two-frequency model explains the dynamics of the dimer's entanglement quite generically.

3.3 Dissipation-induced coherence

Atoms can be removed from a double-well optical trap with single-site resolution using strong resonant laser blasts or a focused electron beam (Gericke et al., 2008; Würtz et al., 2009). As we discussed in Chapter 1, this process can be described by the quantum master equation in Lindblad form for the density matrix ρ,

$$\frac{d}{dt}\rho = -\iota[\hat{H}, \rho] + \frac{1}{2}\sum_{j=1}^{2}\gamma_j\left(\hat{a}_j^\dagger\hat{a}_j\rho + \rho\hat{a}_j^\dagger\hat{a}_j - 2\hat{a}_j\rho\hat{a}_j^\dagger\right),\tag{3.8}$$

where γ_j is the loss rate at site j. Instead of solving the master equation directly, we use the quantum jump method (Section 1.4.2). Previous studies carried out along these lines
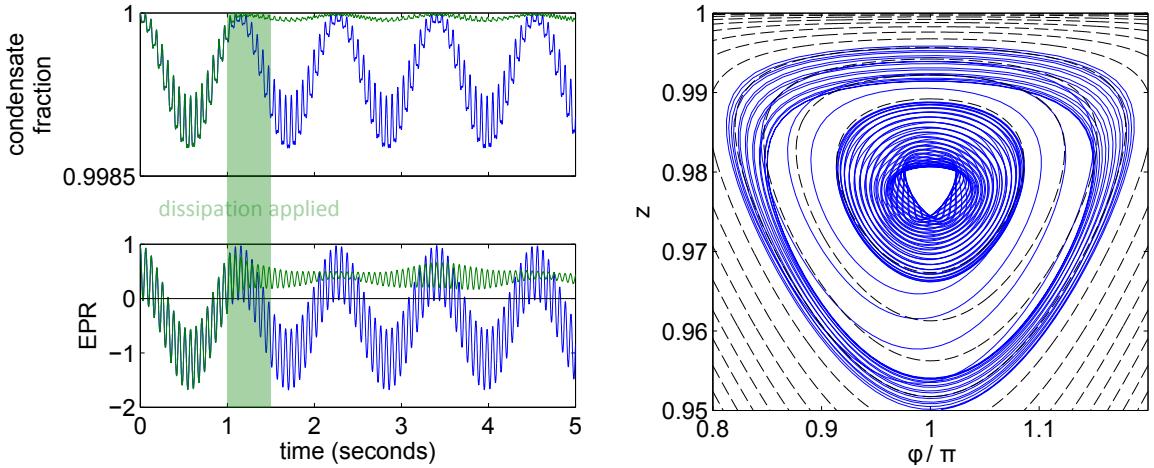
Figure 3.9: Dissipation-induced coherence, with signatures in condensate fraction, EPR entanglement and phase space trajectory (expectation values of z and ϕ). The initial condition is the same as in Figure 3.2, but atom loss ($\gamma_2 = 5\,\mathrm{J}/\hbar$) is induced at site 2 between seconds 1 and 1.5 of the simulation. The plots of condensate fraction and EPR compare the results without (blue) and with (green) dissipation.

show that controlled atom loss may lead to improved coherence (as measured by, among other indicators, the condensate fraction) in the Bose–Hubbard dimer (Trimborn et al., 2008b; Witthaut et al., 2008) and in multi-well systems (Trimborn et al., 2011; Witthaut et al., 2011; Kordas et al., 2012).

An example of dissipation-induced coherence, simulated using the quantum jump method, is shown in Figure 3.9. The initial condition is a coherent state near the self-trapping fixed point. After a second of free evolution, atoms are removed from the less populated site for half a second. The result is a long-term increase in condensate fraction and a transition from intermittent entanglement to a persistently entangled state. This process can be understood within the phase space picture: the system's trajectory is driven towards the stable fixed point, which is a region of high entanglement.

How representative is the picture presented above? Consider again the evolution of 10,000 coherent states uniformly spaced in z and ϕ, shown in Figure 3.8. Between the quantum revivals, the fraction of entangled states is substantially increased by the

application of dissipation. This implies the mechanism shown in Figure 3.9 operates for an appreciable range of initial conditions.

Analogous phenomena have recently been predicted (Grišins et al., 2016) and observed (Rauer et al., 2016) in a quasi-1D ultracold atomic gas. In that setting, the application of dissipation to a rapidly rotating Wigner function symmetrically narrows it, leading to a lowering of the energy. As this happens simultaneously to all occupied modes of a multimode system, it leads to the cooling of the gas.

3.4 Summary & Outlook

In this chapter, we have used the global phase space picture of the Bose–Hubbard dimer to illuminate the dynamics of entanglement in this system and provide a novel perspective on dissipation-induced coherence. We showed that for initial conditions close to the BJJ self-trapping points the dimer's dynamics is completely captured by a projection onto just three eigenstates. Where the projection is successful two frequencies appear prominently in the observables: f_{fast}, due to the mean-field motion, and f_{slow}, associated with a quantum revival. These frequencies are accurately analytically approximated by a second-order expansion about the strong-coupling limit. The frequency f_{slow} sets the dominant time scale for the dynamics of EPR entanglement in the BEC dimer. This is because the regions of phase space in which our description is valid coincide with the regions where EPR entanglement persists. It is also within these regions that dissipation-induced entanglement can be induced.

The significance of this work is two-fold. Firstly, the patterns we describe—two-frequency motion near the fixed point, the driving of the system into the fixed point by dissipation and the resulting enhanced coherence—should be observable in ongoing experiments. Secondly, and more broadly, analogous patterns may be present in larger,

multi-well systems of cold atoms in optical lattices. These systems are potential platforms for quantum information processing, but by virtue of their size cannot be analyzed via exact techniques. Consequently, relationships between approximate but tractable semi-classical dynamics and inherently quantum behavior such as are described here offer an attractive path to large-scale quantum engineering.

Chapter 4

Quantum magnetron

In the preceding chapters we have studied the Bose–Hubbard dimer as a model for cold atoms in optical lattices. In this chapter we consider a very different problem, that of devising quantum models of sources of microwave radiation based on cyclotron electron motion. We focus on the simplest such device, the cylindrical anode magnetron. Its effective quantum description turns out to be a dissipative bosonic dimer, albeit with a different coupling to the reservoir than we have considered so far. Our model shows that net radiation gain persists deep into the quantum regime and that startup will take place even if the field initially contains no photons, thanks to spontaneous emission. Most importantly, though, our work provides a framework for designing solid-state analogs of the magnetron and related devices.

This chapter is based on Pudlik et al. (2016).

4.1   Introduction

Magnetrons are vacuum tubes that convert a DC voltage into electromagnetic radiation in the microwave range. Historically, the designs of vacuum tube and solid state radiation sources were radically different, as transport in semiconductors was limited to the diffusive regime. Today, as a wide range of two-dimensional materials transition from basic research into the toolkit of device designers, it is becoming possible to build solid state de-

vices characterized by ballistic transport (Liang et al., 2007; Du et al., 2008; Mayorov et al., 2011; Wang et al., 2015). Thus, a broad range of vacuum tube designs perfected over the decades—magnetrons, crossed-field amplifiers, gyrotrons, etc. (Gilmour, 2011)—can serve as direct inspiration for a new generation of solid state radiation sources. Such devices could retain some of the advantages of tubes, such as their wide frequency tunability, without the disadvantages of cost and weight associated with vacuum technology. But the new solid state devices would be different in one critical respect: due to their small size and the presence of band structure, they will exhibit quantum effects. Past work on these devices has focused on analogs of linear beam tubes (Gribnikov et al., 2003; Asada, 2003; Ryzhii et al., 2009). Here, we discuss crossed-field designs. As a first step in the investigation of this class of devices, we propose a simple quantum model of the magnetron.

We focus on the most basic magnetron design, the so-called cylindrical anode or Hull magnetron (Hull, 1928; Collins, 1964; Ma, 2004). We briefly review the classical mechanism of its operation in Section 4.2 before developing in the following two sections a fully quantum model in which both the electron motion and the electromagnetic field are quantized.

4.2 The classical model of the magnetron

The cyclotron resonance magnetron consists of two coaxial conducting cylinders; see the top row of Figure 4.1. The inner cylinder is kept at a negative potential and constitutes the cathode, the grounded outer cylinder is the anode, and the space between them is evacuated. An external DC magnetic field points along the axis of the cylinders.
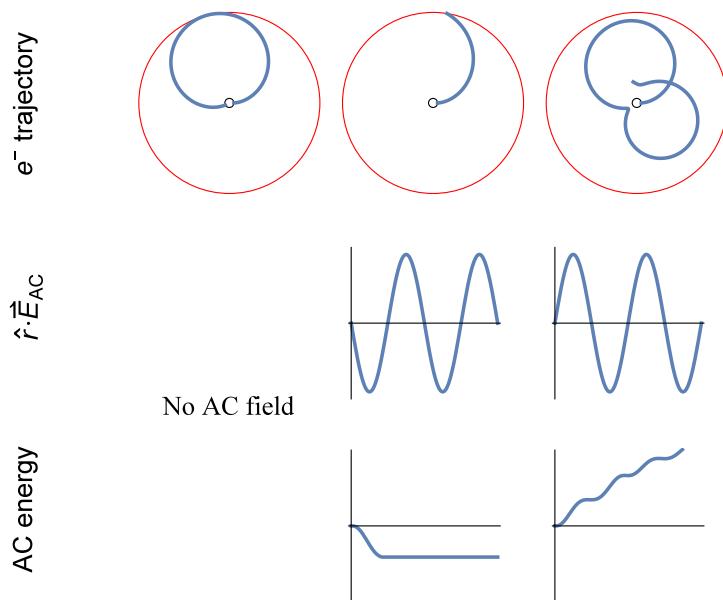
Figure 4.1: Principle of operation of the cyclotron resonance magnetron. The DC fields are set up so that $V \approx V_H$ (first column). If an electron is emitted when the AC voltage has the same polarity as the DC, the electron collides with the anode before removing much energy from the field (second column). If it is emitted when the AC voltage has a polarity opposite to the DC, it remains in the device for a longer time and exchanges more energy with the field (third column).

Equations of motion   Consider an electron moving in the coaxial electrode arrange-
ment of Figure 4.1, with its position given in the usual cylindrical coordinates,

$$\mathbf{r} = s\,\hat{\mathbf{s}} + \phi\,\hat{\phi} + z\,\hat{\mathbf{z}}.$$

The electron moves under the influence of the Lorentz force,

$$\mathbf{F} = -e\mathbf{v} \times \mathbf{B} - e\mathbf{E} = -eB\mathbf{v} \times \hat{\mathbf{z}} + eE\hat{\mathbf{s}}.$$

The motion of the electron is confined to $z = $ const.; we'll take $z = 0$. Since

$$\mathbf{v} = \dot{s}\,\hat{\mathbf{s}} + s\dot{\phi}\,\hat{\phi},$$

we have

$$\mathbf{F} = \hat{\mathbf{s}}\left(eBs\dot{\phi} + eE\right) + \hat{\phi}\left(eB\dot{s}\right)$$

and

$$\mathbf{a} = \frac{d\mathbf{v}}{dt} = \hat{\mathbf{s}}\left(\ddot{s} - s\dot{\phi}^2\right) + \hat{\phi}\left(2\dot{s}\dot{\phi} + s\ddot{\phi}\right).$$

The equations of motion are therefore,

$$\hat{\mathbf{s}}: \qquad \ddot{s} - s\dot{\phi}^2 = -\frac{eB}{\mu}s\dot{\phi} + \frac{eE}{\mu},$$

$$\hat{\phi}: \qquad 2\dot{s}\dot{\phi} + s\ddot{\phi} = \frac{eB}{\mu}\dot{s},$$

where μ is the charge carrier mass.

   To produce the top panels of Figure 4.1, these equations were solved numerically with

the electric field magnitude given by,

$$E(s, t) = E_{DC} + E_{AC}$$
$$= \frac{V_{DC}}{s \ln \frac{s_c}{s_a}} + \frac{V_{AC}}{s_a - s_c} \sin(\omega t + \phi).$$

In the absence of an AC field, the conserved electron energy is given by,

$$\epsilon = \frac{\mu}{2}\left(\dot{s}^2 + s^2\dot{\phi}^2\right) - eV_{DC}\frac{\ln \frac{s_c}{s}}{\ln \frac{s_c}{s_a}}.$$

In the presence of the AC field, ϵ becomes a function of time. The difference between $\epsilon(t = 0)$ and $\epsilon(t = \tau)$ is the net energy gained by the AC field in the t interval $[0, \tau]$.

Hull cutoff voltage An electron emitted by the cathode performs cyclotron motion within the device. The radius of the cyclotron orbit increases with the accelerating voltage, V. Below the so-called Hull cutoff voltage, V_H, the diameter of the orbit is smaller than the device radius, and the emitted electrons never reach the anode. Above V_H, the electrons reach the anode and the device is conducting.

To find the Hull cutoff voltage, rewrite the second equation of motion as,

$$\frac{1}{s}\frac{d}{dt}(s^2\dot{\phi}) = \frac{eB}{\mu}\dot{s},$$
$$\frac{d}{dt}(s^2\dot{\phi}) = \frac{eB}{2\mu}\frac{d}{dt}s^2.$$

This implies,

$$s^2\dot{\phi} = \frac{eB}{2\mu}s^2 + C, \qquad \frac{dC}{dt} = 0.$$

If the electron starts from rest at the cathode ($\dot{\phi} = 0$, $s = s_c$), then

$$0 = \frac{eB}{2\mu}s_c^2 + C \quad \Rightarrow \quad C = -\frac{eB}{\mu}s_c^2$$

and so

$$\dot{\phi} = \frac{eB}{2\mu}\left(1 - \frac{s_c^2}{s^2}\right)$$

where s_a is the anode (outer) diameter.

We're interested in trajectories in which the electron barely grazes the anode. At the apex of such a trajectory, $s = s_a$ and the velocity is purely tangential, so that conservation of energy gives,

$$\frac{1}{2}\mu\dot{\phi}^2 s_a^2 = eV.$$

Using the $\dot{\phi}$ equation and rearranging, we obtain the Hull voltage condition,

$$\frac{V_H}{B^2} = \frac{es_a^2}{8\mu}\left(1 - \frac{s_c^2}{s_a^2}\right)^2. \tag{4.1}$$

AC operation Now, consider a device operating just below V_H. Connect a resonant circuit tuned to the cyclotron frequency to the cathode and anode; this generates an AC voltage in addition to the DC one. Those electrons emitted when the AC voltage has the same polarity as the DC will absorb energy from the electromagnetic field—but since they are accelerated by a voltage $V > V_H$, they will be removed from the device by a collision with the anode during their first orbit (see first column of Figure 4.1). Those electrons emitted when the AC voltage has the opposite polarity lose energy to the field and remain in the device. Crucially, by the time these slowed electrons reach the apex of their orbit and turn around, the polarity of the AC voltage reverses, so that they are once again giving up energy to the field. Thus, those electrons that are not quickly removed

by a collision with the anode continuously transfer their energy to the electromagnetic field (see third column of Figure 4.1). The result is net emission.

An important subtlety is that the interaction with the electromagnetic field perturbs the electron's orbit, leading to a gradual change of the relative phase of the electron's and the field's oscillations. Therefore, even the electrons which initially contribute energy to the field will eventually absorb it instead. From an energy perspective, the problem can be stated as follows: if the only way for the electron to be removed from the device is a collision with the anode, then by the time the electron is removed it must have absorbed energy on net from the AC field. To eliminate this problem, *all* electrons are removed from the device on some timescale long compared to the cyclotron frequency but short relative to the dephasing time, even if they are in orbits too small to reach the anode. In vacuum magnetrons, this can be achieved by tilting the magnetic field slightly away from the electrodes' axis.

4.3   Proposed device

The classical model of the previous section suggests the device design shown in Figure 4.2. Recall that B, the DC magnetic field, is related to the frequency of operation through the cyclotron condition,

$$\omega = \frac{eB}{\mu}. \tag{4.2}$$

Critically, unlike in the vacuum device, the effective charge carrier mass can be controlled by appropriate choice of material. This allows access to higher emission frequencies. For example, in a monolayer of GaSe, with an effective mass of $0.053\,m_e$ (Wickramaratne et al., 2015), an emission frequency of 1 THz should be achieved at a field of 1.9 Tesla. (The device geometry and the Hull condition of Equation 4.1 set the voltage drop at
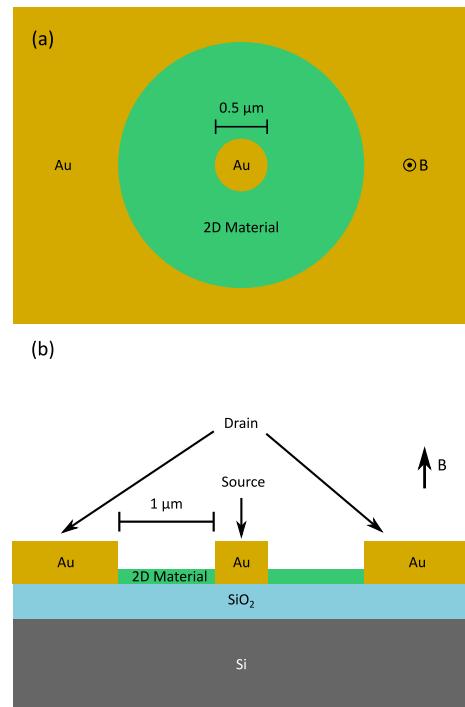
Figure 4.2: Solid state magnetron. *(a)* Top view. *(b)* Side view.

1.6 V.) Other two-dimensional materials with small effective masses and parabolic band structures could be used as well. Bilayer graphene would be a natural candidate, but its band structure shows deviations from parabolicity, and consequently its Landau levels are only approximately uniformly spaced (Pereira et al., 2007). Another possibility would be to use the two-dimensional electron gas in a AlGaAs/GaAs or AlGaAs/InGaAs/GaAs heterostructure, with effective masses of $0.068\,m_e$ (Zudov et al., 2001) and $0.073\,m_e$ (Liu et al., 1988), respectively. This would require a device geometry slightly different from that shown in Figure 4.2, with electrodes penetrating capping layers to contact the two-dimensional electron gas.

Unfortunately, the validity of the simple classical model is far from obvious: the distance between the electrodes is less than 50 magnetic lengths ($\sqrt{\hbar/eB}$), a scale at which the wave nature of the electron cannot be ignored. In the remainder of this chapter, we propose and develop a fully quantum model of a solid state magnetron.

4.4   Quantum model: DC operation

In the classical picture described in Section 4.2, a DC magnetic field and an absorbing boundary allow for the transfer of energy from a DC voltage source to an AC signal. We will now describe the same process from a quantum perspective.

To simplify the analysis, we will discuss a rectangular, rather than cylindrical, geometry as shown in Figure 4.3. (The rectangular geometry is simpler because the DC electric field between the electrodes has a constant magnitude. The general mechanism of device operation is unchanged.) Furthermore, we will restrict our considerations to a planar, or 2D, device. Within the device region ($y \in [0, L]$) there are constant crossed electric and magnetic fields $\mathbf{E}$ and $\mathbf{B}$, while outside of it—in the electrodes—the fields are zero. The motion of an electron subject to these external potentials is described by the
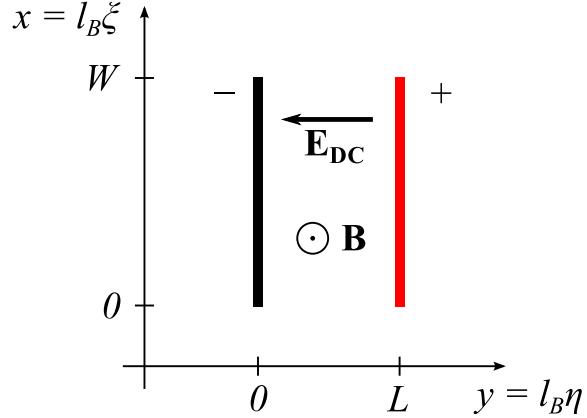
Figure 4.3: A schematic of the quantum magnetron model. We will assume $W \gg L$.

Hamiltonian,

$$H = \frac{1}{2\mu}(\mathbf{p} + e\mathbf{A})^2 - e\Phi, \tag{4.3}$$

where $-e < 0$ is the electron charge and μ the electron mass.

We choose the Landau gauge, in which

$$\Phi = \begin{cases} 0 & \text{for } y < 0, \\ Ey & \text{for } y \in [0, L], \\ EL & \text{for } y > L, \end{cases} \quad \mathbf{A} = \begin{cases} 0 & \text{for } y < 0, \\ By & \text{for } y \in [0, L], \\ BL & \text{for } y > L. \end{cases} \tag{4.4}$$

By introducing the cyclotron frequency and magnetic length,

$$\omega_c = \frac{eB}{\mu}, \quad l_B = \sqrt{\frac{\hbar}{eB}}, \tag{4.5}$$

we can rewrite the Hamiltonian in terms of dimensionless variables,

$$\xi = x/l_B, \quad \eta = y/l_B, \quad \alpha = \frac{eEl_B}{\hbar\omega_c}, \quad \Lambda = L/l_B, \tag{4.6}$$

as,

$$H = \frac{1}{2}\hbar\omega_c \times \begin{cases} p_\xi^2 + p_\eta^2 & \text{for } \eta < 0, \\ (p_\xi + \eta)^2 + p_\eta^2 - 2\alpha\eta & \text{for } \eta \in [0, \Lambda], \\ (p_\xi + \Lambda)^2 + p_\eta^2 - 2\alpha\Lambda & \text{for } \eta > \Lambda. \end{cases} \tag{4.7}$$

In this gauge, ξ does not appear in the Hamiltonian and p_ξ is a constant of the motion. The energy eigenstates $\{\psi\}$ can be taken to be simultaneous eigenstates of p_ξ:

$$\psi_k(\xi, \eta) = e^{ik\xi}\phi_k(\eta), \tag{4.8}$$

where ϕ_k is an eigenstate of the one-dimensional Hamiltonian,

$$H_k = \frac{1}{2}\hbar\omega_c \left(p_\eta^2 + V_k(\eta)\right). \tag{4.9}$$

The effective potential $V_k(\eta)$ is,

$$V_k(\eta) = \begin{cases} k^2 & \text{for } \eta < 0, \\ (k + \eta)^2 - 2\alpha\eta & \text{for } \eta \in [0, \Lambda], \\ (k + \Lambda)^2 - 2\alpha\Lambda & \text{for } \eta > \Lambda. \end{cases} \tag{4.10}$$

If we neglected the electrodes (assumed the device region extends from $-\infty$ to ∞, rather than from 0 to Λ), the effective potential would be parabolic, leading to eigenstates and energies of a simple harmonic oscillator,

$$\psi_{m,k} = \sqrt{\frac{l_B}{W}} e^{ik\xi} e^{-(\eta+k-\alpha)^2} \mathcal{H}_m(\eta + k - \alpha), \tag{4.11}$$

$$\epsilon_m = \hbar\omega_c \left(m + \frac{1}{2}\right) + \hbar\omega_c \left(\alpha k - \frac{\alpha^2}{2}\right), \tag{4.12}$$

where $\mathcal{H}_m$ is the m'th Hermite polynomial, $m = 0, 1, 2, \ldots$; $k = \frac{2\pi l_B}{W}p$ for $p \in \mathbb{Z}$; and W is the device width. If the device region is large but finite, we expect the eigenstates to take a similar form within this region.Halperin (1982) This implies we are interested in states the center of which is within the device, or those for which $k \in (\alpha - \Lambda, \alpha)$.

The parameter α is a dimensionless measure of the electric field strength. If the device is operated at the Hull cutoff voltage, i.e. if the width of the classical cycloid trajectory is equal to the device length ($\frac{2E}{B\omega_c} = L$), then

$$\alpha = \frac{\Lambda}{2}, \tag{4.13}$$

the allowed k values are $k \in (-\Lambda/2, \Lambda/2)$ and the effective potential takes the simple form,

$$V_k(\eta) = \begin{cases} k^2 & \text{for } \eta < 0, \\ (k + \eta)^2 - \Lambda\eta & \text{for } \eta \in [0, \Lambda], \\ k^2 + 2k\Lambda & \text{for } \eta > \Lambda. \end{cases} \tag{4.14}$$

Note that the potential is parabolic within the device region and always contains a bound state as well as higher-energy scattering states. In what follows we will restrict our attention to the $k = 0$ case, corresponding to an electron injected into the device with no momentum in the x (or η) direction.

In the absence of an AC field, the magnetron operates as a diode (see Figure 4.4). For $\alpha \leq \frac{\Lambda}{2}$, an electron initially localized just within the device, by the cathode, can be decomposed into eigenstates that do not enter the anode; consequently, there is no current. For $\alpha > \frac{\Lambda}{2}$, however, states localized near the cathode can be decomposed into scattering states extending to the anode, and current is observed. Increasing α even further affects states initially localized closer to the device's center, but since the electrons
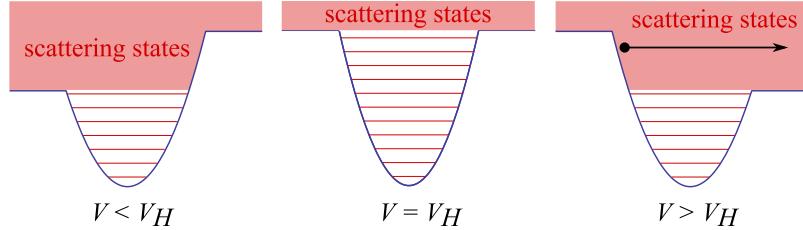
Figure 4.4: In the absence of an AC field, the magnetron operates as a diode. The effective potential $V_0(\eta)$ is plotted above for three values of α (or, equivalently, DC voltage), for $k = 0$. Below and at the Hull voltage V_H, no conduction is observed, as an electron localized near the left edge of the device can be decomposed into bound states. Above V_H, the electron can only be decomposed into scattering states, and the current is a constant independent of voltage.
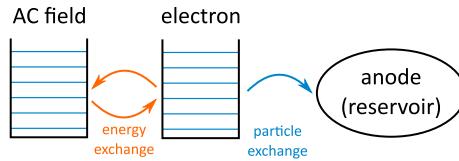
Figure 4.5: Schematic of the two-mode quantum model of magnetron AC operation.

enter the device near the cathode, this does not increase the current. Thus, the current-voltage characteristic is approximately a step function, in agreement with the classical model.

4.5 Quantum model: AC operation

To treat the interaction of the electron with the AC field, we will introduce a simplified effective model schematically depicted in Figure 4.5. We will consider only one mode of the AC field, described by the Hamiltonian,

$$H_{\text{field}} = \hbar\omega \left(\hat{b}^\dagger \hat{b} + \frac{1}{2}\right), \quad [\hat{b}, \hat{b}^\dagger] = \hat{1}. \tag{4.15}$$

Since the effective potential $V_0(\eta)$ within the device region is parabolic, we will approximate the single-particle electron energy with another harmonic mode:

$$H_{\text{electron}} = \hbar\omega \left(\hat{a}^\dagger \hat{a} + \frac{1}{2}\right), \quad [\hat{a}, \hat{a}^\dagger] = \hat{1}. \tag{4.16}$$

The interaction energy between the electron and the field is (Marcuse, 1980, p. 57),

$$H_{\text{int}} = \frac{\hbar e}{2L} \frac{1}{\sqrt{\mu C}} (\hat{a}^\dagger + \hat{a})(\hat{b}^\dagger + \hat{b}) = \frac{e}{2\Lambda} \sqrt{\frac{\hbar\omega}{C}} (\hat{a}^\dagger + \hat{a})(\hat{b}^\dagger + \hat{b}), \tag{4.17}$$

where C is the magnetron's capacitance. Defining

$$J = \frac{e}{2\Lambda} \frac{1}{\sqrt{\hbar\omega C}}, \tag{4.18}$$

and performing a rotating wave approximation [justified as long as the coupling is small, $J \ll \omega$ (Walls and Milburn, 2008)], we can write the total effective Hamiltonian in dimensionless form,

$$H_{\text{eff}} = \hbar\omega \left(\hat{a}^\dagger \hat{a} + \hat{b}^\dagger \hat{b} + J(\hat{a}^\dagger \hat{b} + \hat{b}^\dagger \hat{a}) + \hat{1}\right). \tag{4.19}$$

This model incorporates the effects of the DC and AC fields but does not describe the electron being absorbed by the anode. In the absence of this dissipative process, neither the classical nor the quantum model predicts net energy transfer to the AC field.

To model electron loss from the magnetron cavity, we couple the system described by H_{eff} to a fermionic reservoir representing the anode:

$$H_{\text{E}} = \sum_k \varepsilon_k \hat{r}_k^\dagger \hat{r}_k, \quad \{\hat{r}_k, \hat{r}_l^\dagger\} = \delta_{k,l}. \tag{4.20}$$

The annihilation (creation) of an electron in a state n of the approximate harmonic poten-

tial within the device is described by the fermionic operator $\hat{c}_n$ ($\hat{c}_n^\dagger$), with $\{\hat{c}_m, \hat{c}_n^\dagger\} = \delta_{m,n}$. The electron part of the Hamiltonian can still be written as Equation 4.16,[1] but the operator $\hat{a}$ is now *defined* as,

$$\hat{a} = \sum_{n=0}^{\infty} \sqrt{n+1}\, \hat{c}_n^\dagger \hat{c}_{n+1}. \tag{4.21}$$

On the subspace of one-electron states, the operator $\hat{a}$ satisfies the usual bosonic commutation relation. The most general form of the coupling between the electron in the device and the fermionic reservoir is,

$$\hat{V} = \sum_n \sum_k \gamma_{n,k} (\hat{c}_n + \hat{c}_n^\dagger)(\hat{r}_k + \hat{r}_k^\dagger). \tag{4.22}$$

Since we are not interested in the dynamics of the reservoir, we will treat the electron and AC mode as an open quantum system in the sense of Section 1.4. This will allow us to derive equations of motion for the system degrees of freedom only.

The details of the derivation, which uses the approach of Tomka (2014) originally developed by Beaudoin et al. (2011) are in Appendix D. Here, we will only recapitulate the assumptions:

1. Born approximation: the density matrix of the anode is only negligibly affected by the interaction with the electron in the device.

2. Markov approximation: the anode correlation functions decay at a rate much faster than any other timescale of the model.

3. Rotating wave approximation in the system-bath coupling.

4. The anode is in thermal equilibrium, and the Fermi factor of the relevant levels is approximately zero. This implies the anode never emits electrons into the device,

---

[1]Except that the zero-point energy is no longer 1 but rather $\frac{1}{2} + \sum_n \hat{c}_n^\dagger \hat{c}_n$.

and any electron impinging on the anode from the device will be absorbed.

5. We ignore the frequency shift of the device energy levels that results from the coupling to the reservoir. The frequency shift is in general not negligible. However, its main consequence is that the actual emission frequency of the device is different from the DC cyclotron frequency eB/μ.

6. The system-reservoir coupling constants satisfy $\gamma_{n,k} = \gamma_{n,k'} \equiv \gamma_n$ for all n, k, k'. This is a technical assumption which simplifies the form of the final results; it could be substantially relaxed if we wished to make more specific assumptions about the band structure of the anode.

Given these assumptions, the time evolution of the system density matrix is given by an equation of the Lindblad form,

$$\dot{\rho} = -\imath[H_{\text{eff}}, \rho] + \hat{A}\rho\hat{A} - \frac{1}{2}\left(\hat{A}^\dagger\hat{A}\rho + \rho\hat{A}^\dagger\hat{A}\right), \tag{4.23}$$

where the operator $\hat{A}$ is,

$$\hat{A} = \sqrt{2\pi\sigma}\sum_{n=0}^{\infty}\gamma_n\hat{c}_n, \tag{4.24}$$

with σ the anode density of states.[2] Thus, the effect of the anode is to remove electrons from level n at a rate γ_n.

What are the values of the dissipation rates? The scattering modes of the effective potential $V(\eta)$ (Equation 4.14) overlap with the electrodes; an electron excited into one of these levels will be removed from the device at a rate of order $L/v \sim L\sqrt{\frac{\mu}{\hbar\omega}} \gg J$. But as we observed while discussing the classical device, the lower energy electrons must also be removed from the device, albeit at a slower rate $\sim J$, if net emission is to be observed.

---

[2]The density of states is a constant because we have assumed the device, including the electrodes, to be confined to a plane.

Therefore, we will assume γ_n is a step function of n, taking values of order J for the bound states and much larger values for the scattering states.

The model described above could be further extended in interesting ways, some of which we consider in the final section. But the structure we have built up so far is sufficient to capture the essence of magnetron dynamics, as we discuss next.

4.6 Emission from a Fock state

On the face of it, the effective quantum model is very different from the classical one and rather more complicated.[3] This suggests two questions: does the quantum model agree with the classical one? And does it go beyond it, predicting any new effects? To answer them, we simulate the model using the quantum jump algorithm introduced in Section 1.4.2.

The central prediction of the classical model is that energy will be transferred on average from the DC electrical field which accelerates the electron to the AC field. This phenomenon is reproduced in the quantum model. The left panel of Figure 4.6 shows the expected number of quanta (or energy in units of $\hbar\omega$, or—in the case of the EM mode—number of photons) attributable to the electron and the field over time, for an initial Fock state of the field and the electron in which the two have equal energy. Since the electron decays from the device, in the long-time limit it contributes nothing to the system's energy. The field, however, contains more photons at long times than it contained initially.

What is the mechanism behind this process? The interaction between the electron and the AC field enables emission and absorption events. Because the Hamiltonian of

---

[3]In a certain sense, the quantum model is actually much simpler. While the classical model is defined in terms of partial differential equations on a continuous space, the quantum model is described by ordinary differential equations on a discrete space.
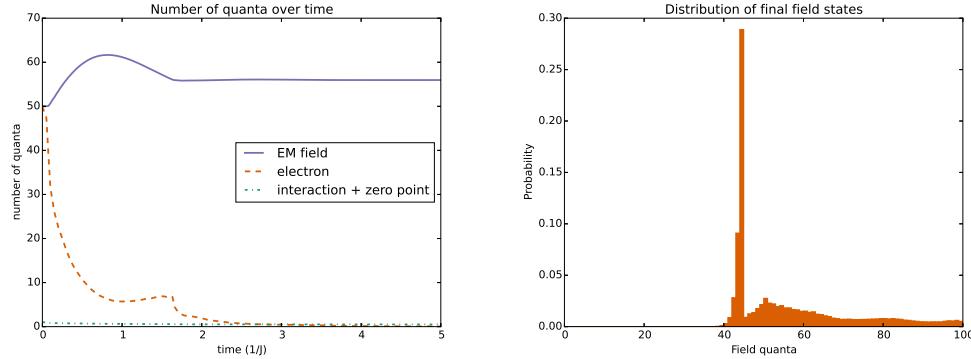
Figure 4.6: Transfer of energy from the DC to the AC field in the quantum magnetron. The left panel shows the time evolution of the expected number of electron quanta, $\langle \hat{a}^\dagger \hat{a} \rangle$ (red), and AC mode photons, $\langle \hat{b}^\dagger \hat{b} \rangle$ (blue), over time. The electron decays from the device, but deposits in the AC field some of its energy, which was ultimately derived from the accelerating DC voltage. The right panel shows the final distribution over Fock states of the EM field: an electron could absorb or emit photons, but sequences of more than a few absorptions did not occur. See the text for further discussion.

Equation 4.19 is symmetric with respect to a relabeling of the modes ($\hat{a} \to \hat{b}$, $\hat{b} \to \hat{a}$), an isolated system would, over times $> 1/J$, be equally likely to emit m photons (transfer m quanta from the electron to the field) as to absorb m photons, for any m. In the open system, this symmetry is broken by the decay rates $\{\gamma_n\}$ that depend on n, the index of the electron level. A sequence of many emissions is now more likely than a sequence of many absorptions, because just a few net absorptions will place the electron in a scattering state—the electron will be removed from the device before it can absorb further. This early termination of chains of net absorptions is illustrated in the right panel of Figure 4.6, which shows the probability distribution over final Fock states of the EM field. The distribution is dramatically skewed to the right: sequences of many emissions (field quanta $\gg 50$) are common, but those of many absorptions (field quanta $\ll 50$) are never observed.

Amplification of an existing AC field, then, is predicted by both the classical and the
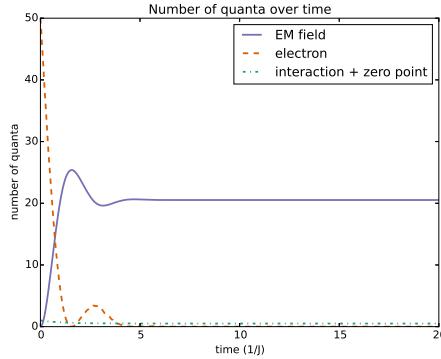
Figure 4.7: The quantum model of the magnetron predicts spontaneous emission. The expected energy of the electron (red) and field (blue) are plotted over time, for an initial Fock state of the electron and vacuum state of the field. Initially, the field carries no energy, but by the time the electron has decayed, about half of the electron's initial energy has been transferred to the field. (The rest of the electron's energy has been lost to the reservoir.)

quantum models. In the former model, the device can *only* operate as an amplifier: if the initial amplitude of the AC field is zero, the classical prediction is that it will stay zero. In contrast, the quantum model of the previous section predicts spontaneous emission even if the field is initially in a vacuum state. This is illustrated in Figure 4.7. (In practice, there is always nonzero field present in the device due to thermal fluctuations, and the magnetron will start up without an external input even in the classical model. At low temperatures, however, the contribution of spontaneous emission should become significant.)

4.7   Summary & Outlook

Inspired by the classical model of the cylindrical diode magnetron, we have proposed an effective quantum model consisting of two bosonic modes coupled to a fermionic reservoir. The quantum model captures the essential behavior of the established classical approach by predicting a net energy transfer from the DC to the AC field. But the quan-

tum framework can explain a greater range of phenomena, such as spontaneous emission when the field starts out in the vacuum state.

Our results suggest that a solid-state analog of the magnetron would continue to act as a radiation source, with the critical difference that the emission frequency could be elevated to the terahertz range by using a material with small effective mass.

The work discussed here can be extended in interesting ways. Accurate numerical simulations accounting for the device geometry, perhaps using non-equilibrium Green's function methods (Datta, 2000, 2005), are the next natural step. Investigating the wide variety of vacuum tube designs beyond the cylindrical anode magnetron (and the interplay between ballistic electron dynamics and electrodynamics they exploit) is another possibility. Finally, one could develop entirely novel designs based on materials with nonparabolic band structures such as graphene. The use of unevenly spaced Landau levels as gain media for lasers had been patented in the 1960s (Wolff, 1966), but at the time thought impossible to realize. Today we possess both the experimental and theoretical tools to finally implement such concepts.

Appendix A

An implementation of the quantum jump algorithm

This Appendix contains a Python implementation of the quantum jump algorithm described in Section 1.4.2.2.

The function below assumes your namespace contains a function `pseudohamiltonian` which returns a matrix representation of the null measurement operator ($\hat{M}_0 - 1$) that appears in Equation 1.26. It does not actually perform the quantum jump, which requires acting on the wavefunction with a problem-dependent operator, but evolves the wavefunction up to the time when the jump ought to be performed. Throughout the evolution, the observables are recorded at regular "snapshot intervals."

```python
import numpy as np
from scipy.integrate import complex_ode

def evolve_until_jump(psi, obs, t, pa):
    """Evolve the wavefunction until the next jump, recording observables.

    Parameters
    ----------
        psi: The initial wavefunction.
        obs: An object with 'measure' and 'snapshots_remaining' methods,
            used for recording the observables given the wavefunction.
        t: Evolution start time.
        pa: Simulation parameters dict.  Should include the key
            'snapshot_interval' (the time between successive measurements)
            and may include any parameters to be passed to the
            'pseudohamiltonian' function or (under 'integrator_params') to
            the integrator.

    Returns
    -------
        tau: Time when the jump took place.
        obs: Updated instance of input obs object.
        psi: Wavefunction at time tau (right before the jump).

    """
    if 'seed' in pa.keys():
        # Random number provided by main program
        r = pa['seed']
    else:
        r = np.random.uniform()

    h = pseudohamiltonian(pa)
    def forward_evolution(t, y):
        """RHS of equation of motion."""
        psi = y[0:-2]
        hpsi = -1.0j*np.dot(h, psi)
        norm_derivative = 2*np.dot(psi.conjugate(), hpsi).real
        return np.append(hpsi, [norm_derivative, 1.0])

    jump_took_place = []
    def terminate(t, y):
        """Should integration be termined at the current time step?"""
        #if np.linalg.norm(y[0:-2])**2 <= r:
        if y[-2].real < 0:
            jump_took_place.append(True)
            return -1 # Stop integration
        else:
            return 0 # Continue on

    integrator = complex_ode(forward_evolution)
    integrator.set_integrator('dopri5', **pa['integrator_params'])
    integrator.set_solout(terminate) # Must be set before initial values to work
    integrator.set_initial_value(np.append(psi, [1 - r, t]), t)
    # Note that the evolved vector was extended by two dimensions, the first
    # of which is the norm of the wavefunction.

    if t > 0:
        # Integrate to the next snapshot.  This special step is necessary when
        # t > 0 so that the interval between snapshots immediately preceding
        # and following the quantum jump is not shorter than the other snapshot
        # intervals.
        next_snapshot = pa['snapshot_interval']*np.ceil(t/pa['snapshot_interval'])
        integrator.integrate(next_snapshot)
```

```python
obs.measure(integrator.y[0:-2]/np.linalg.norm(integrator.y[0:-2]))
for n in range(1, obs.snapshots_remaining() + 1):
    integrator.integrate(t + n*pa['snapshot_interval'])
    if jump_took_place:
        break
    else:
        obs.measure(integrator.y[0:-2]/np.linalg.norm(integrator.y[0:-2]))

if jump_took_place:
    # Use Henon's trick to localize it.
    def backward_evolution(t, y):
        psi = y[0:-2]
        hpsi = -1.0j*np.dot(h, psi)
        norm_derivative = 2*np.dot(psi.conjugate(), hpsi).real
        return np.append(hpsi/norm_derivative,
                         [1.0, 1.0/norm_derivative])

    int_henon = complex_ode(backward_evolution)
    int_henon.set_integrator('dopri5', **pa['integrator_params'])
    int_henon.set_initial_value(integrator.y, integrator.y[-2])
    int_henon.integrate(0)
    tau = int_henon.y[-1].real
    psi_out = int_henon.y[0:-2]
else:
    tau = integrator.y[-1].real
    psi_out = integrator.y[0:-2]

return (tau, obs, psi_out, jump_took_place)
```

Appendix B

Semiclassical quantization

This appendix contains technical details of the semiclassical quantization procedure used in Chapter 2.

B.1 Splitting of the semiclassical ground state

In this appendix, we use Equation 2.16, the quantization condition of Graefe and Korsch (2007), to derive an approximate expression for the energy splitting of the nearly-degenerate self-trapped eigenstates. This expression and its derivation have been known to scholars of the WKB approximation—see Razavy (2003, p. 49) or Child (1991, p. 52)—but the discussion we give here is more complete than that found in other sources.

Equation 2.16 can be rewritten as,

$$\cos(2S_w - S_\phi) = -\frac{1}{\sqrt{1 + \exp(2\pi S_\epsilon)}}. \tag{B.1}$$

Considered as a function of $x \equiv 2S_w - S_\phi$, this equation has pairs of solutions symmetrically spaced about $(2n + 1)\pi$ (see Figure B.1). The pairs of roots coalesce as $S_\epsilon \to -\infty$: in the absence of tunneling, states come in degenerate pairs, one localized in each well. Let the two solutions near $x = \pi$ be $x_\pm$, with $x_+ > \pi$ and $x_- < \pi$. We have,
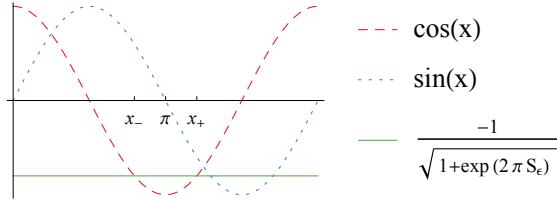
Figure B.1: Graphical representation of the roots of Equation B.1.

$$\tan x_{\pm} = \frac{\mp\sqrt{1 - \cos^2(x_{\pm})}}{\cos x_{\pm}} = \mp \exp(\pi S_{\epsilon}), \tag{B.2}$$

where the sign difference on the right-hand-side arises because $\sin(x)$ changes sign at $x = \pi$, between x_- and x_+.

Recall that $x \equiv 2S_w - S_{\phi}$ is a function of energy. Assume the ground state energy splitting ΔE is sufficiently small that $x(E)$ is approximately linear in an interval of width ΔE about the ground state energy, E_0. Then,

$$x_{\pm} = x(E_0 \pm \Delta E/2),$$

and Equation B.2 gives,

$$\tan(2S_w(E_0 \pm \Delta E/2) - S_{\phi}(S_{\epsilon}(E_0 \pm \Delta E/2))) = \mp \exp(\pi S_{\epsilon}(E_0 \pm \Delta E/2)),$$

or,

$$2S_w(E_0 \pm \Delta E/2) - S_{\phi}(S_{\epsilon}(E_0 \pm \Delta E/2)) = \mp \arctan\left(\exp \pi S_{\epsilon}(E_0 \pm \Delta E/2)\right).$$

Expanding to first order about E_0,

$$2S_w - S_{\phi} \pm \left(2\frac{\partial S_w}{\partial E} - \frac{\partial S_{\phi}}{\partial S_{\epsilon}}\frac{\partial S_{\epsilon}}{\partial E}\right)\frac{\Delta E}{2} = \mp \arctan(\exp(\pi S_{\epsilon})) - \frac{2\pi}{\cosh(\pi S_{\epsilon})}\frac{\partial S_{\epsilon}}{\partial E}\frac{\Delta E}{2}.$$

Subtracting the lower signs from the upper signs and rearranging yields,

$$\frac{\Delta E}{2} = -\frac{\arctan \exp(\pi S_\epsilon)}{2\frac{\partial S_w}{\partial E} - \frac{\partial S_\phi}{\partial S_\epsilon}\frac{\partial S_\epsilon}{\partial E}}. \tag{B.3}$$

Consider the second term in the denominator. Letting $\xi \equiv S_\epsilon$ and using the definition of S_ϕ (Equation 2.17), the dimensionless derivative can be written as,

$$\frac{\partial S_\phi}{\partial S_\epsilon} = -\ln \xi + \frac{1}{2}\psi\left(\frac{1}{2} - \iota\xi\right) + \frac{1}{2}\psi\left(\frac{1}{2} + \iota\xi\right), \tag{B.4}$$

where ψ is the digamma function, defined as

$$\psi(t) = \frac{\Gamma'(t)}{\Gamma(t)}.$$

For $|t| > 3$, an excellent approximation (good to 0.03%) to this function is provided by the asymptotic expansion (Olver et al., 2015, 5.11.2),

$$\psi(t) \approx \ln t - \frac{1}{2t} - \frac{1}{12t^2}.$$

Using this expansion,

$$\frac{\partial S_\phi}{\partial S_\epsilon} \approx \frac{1}{2}\ln\left(1 + \frac{1}{4\xi^2}\right) - \frac{4}{3}\frac{1 + 2\xi^2}{(1 + 4\xi^2)^2} \approx \frac{3 - 8\xi^2(1 - 2\xi^2)}{24\xi^2(1 + 2\xi^2)^2}.$$

This expression is already smaller than 0.01 at $\xi = 2$, and decreases with ξ as $1/\xi^2$. Since the phase space derivatives $\partial S_w/\partial E$ and $\partial S_\epsilon/\partial E$ are of the same order, and $\xi = S_\epsilon$ is of order N, the second term in the denominator of Equation B.3 can be neglected:

$$\Delta E = -\frac{\arctan \exp \pi S_\epsilon}{\frac{\partial S_w}{\partial E}}.$$

Since the splitting is small, $\exp(\pi S_\epsilon) \ll 1$ and so $\arctan \exp(\pi S_\epsilon) \approx \exp(\pi S_\epsilon)$. If we let $T = 2\pi/\omega$ be the period of the orbit corresponding to the action $2S_w$,

$$2\frac{\partial S_w}{\partial E} = \frac{1}{\hbar}T = \frac{2\pi}{\hbar\omega}.$$

Neglecting the second term in the denominator of Equation B.3, we get,

$$\Delta E = -\frac{\hbar\omega}{\pi}\exp(\pi S_\epsilon). \tag{B.5}$$

The negative sign of ΔE indicates that x_+ is actually lower in energy than x_-.

As a special case, this result applies to a single particle in a double-well potential described by the Schödinger equation. For that special case there exist a simpler derivation of Equation B.5: see Landau and Lifshitz (1981), §50.

B.2 Action integrals

To perform actual calculations using the formula,

$$\Delta E = \frac{\hbar\omega}{\pi}\exp(\pi S_\epsilon),$$

we need to find explicit expressions for ω (or the corresponding period T) and S_ϵ in terms of E and Λ. It will also prove useful to find an expression for $2S_w$, the action associated with the self-trapped orbit, which determines the energy about which the splitting takes place. All of these quantities depend on the shape of the classical orbits of the mean-field Hamiltonian of Equation 2.13. The equation of the orbit is,

$$\phi(z, E, \Lambda) = \arccos \frac{\Lambda z^2 - 2E}{2\sqrt{1 - z^2}}, \tag{B.6}$$

and the classical turning points of the orbits (see Figure 2.7) are,

$$z_\pm(E, \Lambda) = \sqrt{\frac{\pm\sqrt{1 - 2E\Lambda + \Lambda^2} + \Lambda E - 1}{\Lambda^2/2}}. \tag{B.7}$$

In what follows, we will generally suppress the explicit dependence of ϕ and $z_\pm$ on E and Λ to obtain clearer expressions. Recall that we defined the dimensionless measure of orbit size as,

$$k \equiv \sqrt{\frac{z_+^2 - z_-^2}{z_+^2}}.$$

We begin with the simplest problem, that of deriving an expression for the orbit period T. The approach to computing the action integrals S_ϵ and S_w will be the same, but the technical details are more involved.

See Graefe et al. (2014) and the references therein for a deeper look at the geometry of the classical model and its relationship to Bose–Hubbard dynamics.

B.2.1   Period T of the classical orbit

The equation of motion for z is,

$$\dot{z} = -\frac{\partial H}{\partial \phi} = -\sqrt{1 - z^2} \sin \phi, \tag{B.8}$$

and so the period is,

$$T = 2 \left| \int_{z_-}^{z_+} \frac{dt}{dz} dz \right| = 2 \int_{z_-}^{z_+} \frac{dz}{\sqrt{1 - z^2} \sin \phi(z)}. \tag{B.9}$$

Since $\sin(\arccos x) = \sqrt{1 - x^2}$, we can use Equation B.6 to eliminate the trigonometric functions:

$$T = 4 \int_{z_-}^{z_+} \frac{dz}{\sqrt{4(1 - z^2) - (\Lambda z^2 - 2E)^2}}. \tag{B.10}$$

Although at first glance this expression has a very complicated structure, the polynomial in the denominator (which is also encountered in the S_w and S_ϵ integrals) can be rewritten in the more suggestive form,

$$4(1 - z^2) - (\Lambda z^2 - 2E)^2 = -\Lambda^2(z^2 - z_+^2)(z^2 - z_-^2). \tag{B.11}$$

The period is therefore,

$$T = \frac{4}{\Lambda} \int_{z_-}^{z_+} \frac{dz}{\sqrt{(z_+^2 - z^2)(-z_-^2 + z^2)}} = \frac{4}{\Lambda z_+} K\left(\sqrt{\frac{z_+^2 - z_-^2}{z_+^2}}\right) = \frac{4}{\Lambda z_+} K(k), \tag{B.12}$$

where K is the complete elliptic integral of the first kind. Note that in this expression, time is measured in the dimensionless units introduced with the Hamiltonian of Equation 2.13. Converting the units to seconds,

$$T = \frac{2}{J\Lambda z_+} K(k), \tag{B.13}$$

where J is measured in hertz.

B.2.2   Action of the classical orbit

The phase space areas (and so actions) associated with the classical orbits can be found by integrating $\phi(z)$. For an orbit in the self-trapping region, the action is

$$S(E, \Lambda) = h\frac{N + 1}{4\pi} \cdot \left(2 \int_{z_-}^{z_+} \pi - \phi(z)\, dz + 2\pi(1 - z_+)\mathbb{1}\,(E < \Lambda/2)\right). \tag{B.14}$$

The prefactor $h\frac{N+1}{4\pi}$ normalizes the total area of phase space to be $h(N+1)$, with N the number of particles. If $E < \Lambda/2$, the orbit is a rotation orbit (see Figure 2.7) and the area of the "cap" at $|z| > z_+$ is added to the integral of $\phi(z)$.

The integral in Equation B.14 can be simplified through an integration by parts:

$$\int_{z_-}^{z_+} \pi - \phi(z)\, dz = \int_{z_-}^{z_+} \frac{z^2 \left(z^2 + 2\frac{E-\Lambda}{\Lambda}\right)}{(1-z^2)\sqrt{(z^2 - z_-^2)(-z^2 + z_+^2)}},$$

where the boundary term is zero since $\phi(z_\pm) = \pi/2$. This is an elliptic integral (Olver et al., 2015, §19.2(i)) and can be reduced to the canonical elliptic integrals using a partial fraction decomposition. Let,

$$P = -(z^2 - z_+^2)(z^2 - z_-^2).$$

Then,

$$\int_{z_-}^{z_+} \pi - \phi(z)\, dz = -z_+ \mathrm{E}(k) + \left(1 - \frac{2E}{\Lambda}\right)\frac{1}{z_+}\left(\mathrm{K}(k) - \frac{1}{1-z_+^2}\Pi\left(\alpha^2, k\right)\right), \tag{B.15}$$

where $\mathrm{K}(k)$, $\mathrm{E}(k)$, and $\Pi(\alpha^2, k)$ are complete elliptic integrals of the first, second and third kinds, k is the measure of orbit size defined in Equation 2.19, and

$$\alpha^2 = \frac{z_+^2 - z_-^2}{z_+^2 - 1}.$$

B.2.3   Tunneling action S_ϵ

The "tunneling action" is defined analogously to the orbit action,

$$S_\epsilon(E, \Lambda) = -\frac{N+1}{4\pi} \cdot 2 \int_{-z_-(E,\Lambda)}^{z_-(E,\Lambda)} |\pi - \phi(z, E, \Lambda)|\, dz,$$

with the absolute value necessary because $\phi(z, E, \Lambda)$ may be complex within the region

of integration. In fact, in the self-trapping region ($E > 1$, $\Lambda > 1$) the argument of the

arccosine in $\phi(z, E, \Lambda)$ is smaller than -1 for all $z \in [-z_-, z_-]$. Consequently, taking

advantage of the identity,

$$\arccos(-1 - x) = \pi - \iota \operatorname{arccosh}(1 + x),$$

one may rewrite S_ϵ as,

$$S_\epsilon = -\frac{N + 1}{\pi} \int_0^{z_-} \operatorname{arccosh}\left(\frac{2E - \Lambda z^2}{2\sqrt{1 - z^2}}\right) dz.$$

As in the case of the orbit action, S_ϵ can be recast as an elliptic integral through integration

by parts, and then reduced to a sum of canonical elliptic integrals using a partial fractions

expansion. The result is,

$$-\frac{\pi S_\epsilon}{N + 1} = -\left(1 - \frac{2E}{\Lambda}\right) \frac{1}{z_+} \Pi(z_+^{-2}, k') + z_+ \left(\mathrm{K}(k') - \mathrm{E}(k')\right), \tag{B.16}$$

where $k' = \sqrt{1 - k^2}$ and we have used identity 19.6.5 in Olver et al. (2015).

B.3 Approximate solution to the quantization problem for large N

In this section, we derive an approximate semiclassical expression for the splitting by

expanding the integrals of the previous section in small orbit sizes, k, and energies, e.

B.3.1 Approximate orbit frequency

To lowest order,

$$\omega = \frac{2\pi}{T} = \frac{\pi \Lambda z_+}{2K(k)} = \sqrt{\Lambda^2 - 1} + O(\sqrt{e}). \tag{B.17}$$

A higher-order expansion is unnecessary because ΔE depends on e primarily through the tunneling phase in the exponent.

B.3.2 Energy of the highest-energy state

Many of the quantities encountered in our discussion so far can be expressed more simply in terms of e [the normalized energy relative to the maximum of E—see Equation 2.22] than E. For instance, the classical turning points are,

$$z_\pm = 1 - \frac{1}{\Lambda^2}\left(1 \mp (\Lambda - 1)\sqrt{e}\right)^2$$

and the dimensionless measure of orbit size is,

$$k^2 = \frac{z_+^2 - z_-^2}{z_+^2} = \frac{4\sqrt{e}}{(\sqrt{e} + 1)^2 + \Lambda(1 - e)}.$$

The quantization condition of Equation 2.21 reads,

$$\frac{\pi}{N+1} - \pi(1 - z_+) \cdot \mathbb{1}\left(e > (\Lambda - 1)^{-2}\right) = -z_+ \mathrm{E}(k)$$
$$- \frac{1 - (\Lambda - 1)^2 e}{\Lambda^2}\frac{1}{z_+}\left(\mathrm{K}(k) - \frac{1}{1 - z_+^2}\Pi(\alpha^2, k)\right), \tag{B.18}$$

with k and $z_\pm$ given by the expressions in the previous section. Consider the case $e < (\Lambda - 1)^{-2}$, when the highest-energy state orbit is a libration. Expanding the elliptic integrals to
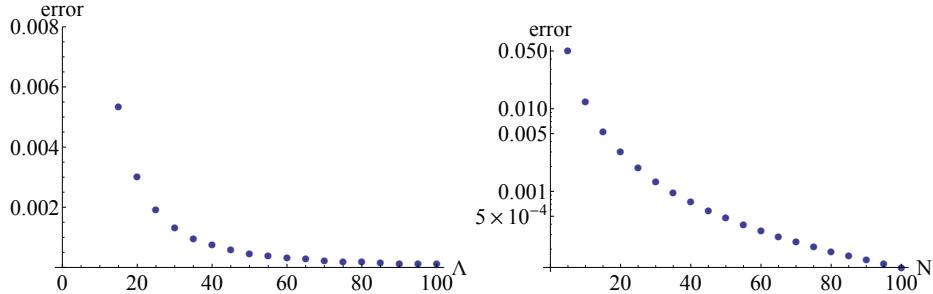
Figure B.2: Relative error in approximating the (numerically exact) solution of Equation B.18 with the lowest-order approximation of Equation B.19. The figure on the left shows the dependence on Λ (for $N = 20$) and that on the right—the dependence on N (for $\Lambda = 2$).

lowest order in k and then to lowest order in e,[1] and then solving for e gives a first-order estimate of the highest-energy state energy,

$$e \approx \frac{2\Lambda\sqrt{\Lambda^2 - 1}}{(\Lambda - 1)^2(N + 1)}.$$
(B.19)

As was already remarked in the main text, this estimate is very good. See also Figure B.2.

What happens if the nonlinearity is sufficiently high that the highest-energy state orbit is a rotation (i.e., $(\Lambda-1)^{-2} < e \ll 1$)? It turns out that this case cannot be successfully treated using the same approach. The term $\frac{1}{1-z_+^2}\Pi(\alpha^2, k)$ becomes ill-behaved, with both the prefactor and α^2 very large. The terms of the small-k^2 expansion of $\Pi(\alpha^2, k)$ are proportional to powers of α^2 (Olver et al., 2015, Eq. 19.5.4), so keeping only the lowest-order terms in k^2 is no longer legitimate. But the difficulty of extending our semiclassical method to this part of the parameter space is not a major concern, for two reasons:

1. The nonlinearity required for the ground state orbit to enclose the point $z = 1$ is large indeed, especially for larger atom numbers. From Equation 2.23, the condition

---

[1]Because the prefactors themselves depend on e, a consistent expansion requires expanding Π to order k^4, though E and K are only expanded to order k^2. (No odd powers of k appear in the expansions.)

$e > (\Lambda - 1)^2$ can be estimated to imply,

$$2\Lambda\sqrt{\Lambda^2 - 1} \approx 2\Lambda^2 > N + 1. \tag{B.20}$$

2. The limit of very strong nonlinearity is particularly easy to treat using quantum perturbation theory (Bernstein et al., 1990; Dounas-Frazer et al., 2007; Salgueiro et al., 2007; Pudlik et al., 2013).

B.3.3 Approximate tunneling action

Finding a good large-N approximation for the tunneling action (Equation B.16) is more difficult because both $\Pi(z_+^{-2}, k')$ and $K(k') - E(k')$ diverge in the limit $k' = \sqrt{1 - k^2} \to 1_-$. The lowest order asymptotic approximation is of $O(e^0)$:

$$-\frac{\pi S_\epsilon}{N + 1} \approx -\frac{\sqrt{\Lambda^2 - 1}}{\Lambda} + \ln\left(\Lambda + \sqrt{\Lambda^2 - 1}\right).$$

It is possible to derive higher-order approximations by combining the known asymptotic expansions of the complete elliptic integrals, but they are complex and disappointingly inaccurate, except for large N and either very large or very small Λ.

Instead of pursuing a formal expansion, let's attempt an *ad hoc* improvement of the zeroth-order expression. S_ϵ is a measure of the barrier to tunneling; as the ground state approaches the separatrix ($e \to 1$), the barrier should disappear. The simplest way to enforce this behavior is to multiply the $O(e^0)$ expression by $(1 - e)$:

$$-\frac{\pi S_\epsilon}{N + 1} \approx \left(-\frac{\sqrt{\Lambda^2 - 1}}{\Lambda} + \ln\left(\Lambda + \sqrt{\Lambda^2 - 1}\right)\right)(1 - e). \tag{B.21}$$

This ansatz works remarkably well; furthermore, unlike the asymptotic expansions which
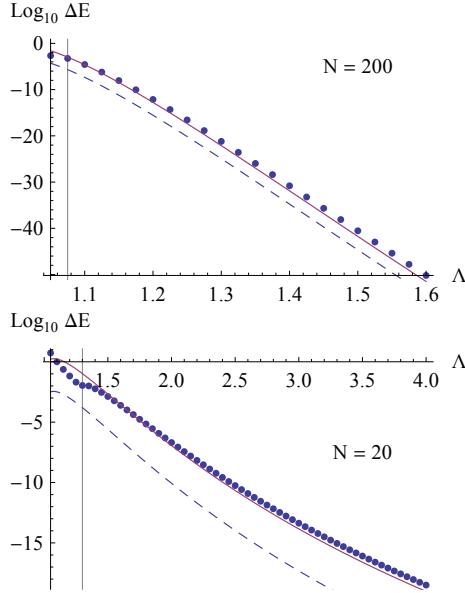
Figure B.3: Approximations to the semiclassical highest-energy state splitting. Numerical solutions to Equation 2.16 are shows as blue dots; Equation B.22 is plotted as the solid red line, while Equation B.22 with $e = 0$ is shown in dashed blue. The black vertical line marks the point where the semiclassical approximation must break down because the area of phase space associated with the self-trapped region is less than $h/2$.

may be either smaller or larger than the true value, Equation B.21 gives an upper bound on the magnitude of S_ϵ for all Λ.

B.3.4   Approximate splitting formula

By combining the approximate expressions for the classical orbital frequency and the tunneling phase, we arrive at the following expression for the highest-energy state splitting:

$$\Delta E \approx \frac{\hbar\omega}{\pi} \left(\frac{1}{\omega}e^{-z_0}\right)^{(N+1)(1-e)},$$

where $z_0 \equiv \sqrt{1 - \frac{1}{\Lambda^2}}$ is the position of the classical potential maximum and $\omega = \Lambda\sqrt{1 - \frac{1}{\Lambda^2}}$ is the frequency of motion about it (cf. Equation B.17]. In this expression, the frequency is measured in the dimensionless units introduced with the Hamiltonian of Equation 2.13.

In the units of J and U (Hz),

$$\Delta E \approx 2J\frac{\omega}{\pi}\left(\frac{1}{\omega}e^{-z_0}\right)^{(N+1)(1-e)}. \tag{B.22}$$

Figure B.3 shows a comparison of this approximation with the numerical solution of the semiclassical quantization condition (Equation 2.16]. Since our approximation to S_ϵ overestimates the barrier to tunneling, the tunneling frequency is generally underestimated, except close to the bifurcation where the dependence of ω on e (which we neglect) becomes important. Some qualitative features of the dependence of ΔE on Λ can be reproduced even without the factor of $(1-e)$ in the exponent, and the agreement with the numerical solution improves as N increases. However, this $e = 0$ approximation to ΔE is generally not within an order of magnitude of the numerically computed value.

Appendix C

Quantum revivals in the Bose–Hubbard dimer

This appendix discusses revivals of the wavefunction and certain observables occurring in the Bose–Hubbard dimer at large U. First, in Appendix C.1, we show that for $J = 0$ and N odd the wavefunction rephases with a period of $\pi\hbar/U$. Then, in Appendix C.2, we show that the condensate fraction and EPR entanglement measure rephase with the same period, for any N. Finally, in Appendix C.3 we derive perturbative corrections to the $J = 0$ estimates of the "slow" and "fast" frequencies used in Chapter 3; the result of this derivation is used as Equation 3.7 in the main text.

C.1   Revivals of the wavefunction

Consider a Bose–Hubbard dimer with $J = 0$ and N atoms. The energy eigenstates of this system are the Fock states $|n\rangle \equiv |N_1, \, N - N_1\rangle$, with energies

$$\epsilon_n = \frac{n(n-1)}{2}U + \frac{(N-n)(N-n-1)}{2}U. \tag{C.1}$$

It will prove convenient to define a de-dimensionalized energy,

$$h_n \equiv \frac{\epsilon_n}{U}. \tag{C.2}$$

The coherent states of the dimer are of the form,

$$|\psi(t)\rangle = \sum_{n=0}^{N} a_n\, e^{-\iota \epsilon_n t/\hbar}\, |n\rangle, \tag{C.3}$$

with the expansion coefficients a_n all nonzero. Consider translating the coherent state in time by

$$\tau \equiv \frac{\pi\hbar}{U}. \tag{C.4}$$

As was asserted in Chapter 3, the results of this translation depend on the value of N:

$$|\psi(\tau)\rangle = \begin{cases} |\psi(0)\rangle & \text{for } N = 1 + 4p, \\[2mm] -\sum_{n=0}^{N}(-1)^n a_n\, |E_n\rangle & \text{for } N = 2 + 4p, \\[2mm] -|\psi(0)\rangle & \text{for } N = 3 + 4p, \\[2mm] \sum_{n=0}^{N}(-1)^n a_n\, |E_n\rangle & \text{for } N = 4 + 4p, \end{cases} \tag{C.5}$$

with $p \in \mathbb{Z}_{\geq 0}$. Let us prove this assertion case by case.

Case 1. *If $N = 1 + 4p$ for $p \in \mathbb{Z}_{\geq 0}$, then $|\psi(\tau)\rangle = |\psi(0)\rangle$.*

Proof. Note that,

$$\exp\left(-\iota \epsilon_n \tau/\hbar\right) = \exp(-\iota \pi h_n). \tag{C.6}$$

The de-dimensionalized energy h_n satisfies,

$$2h_n = n(n-1) + (N-n)(N-n-1) = n(n-1) + (1+4p-n)(1+4p-n-1)$$

$$= n^2 - n + 4p - n + 16p^2 - 4np - 4np + n^2 = 2(n^2 - n) + 4p + 16p^2 - 8pn$$

$$h_n = n(n-1) + 2(p + 4p^2 - 2pn)$$

The right-hand side is even for any $n \in \mathbb{Z}_{\geq 0}$ and any $p \in \mathbb{Z}_{\geq 0}$. Therefore, h_n is even and

$\exp\left(-\imath\pi h_n\right) = 1$. It follows that $|\psi(\tau)\rangle = |\psi(0)\rangle$. $\qquad\square$

Case 2. *If $N = 3 + 4p$ for $p \in \mathbb{Z}_{\geq 0}$, then $|\psi(\tau)\rangle = -|\psi(0)\rangle$.*

Proof. We proceed as in the previous case.

$$2h_n = n(n-1) + (N-n)(N-n-1) = n(n-1) + (3+4p-n)(3+4p-n-1)$$

$$= n^2 - n + 6 + 12p - 3n + 8p + 16p^2 - 4np - 2n - 4np + n^2$$

$$= 2n^2 - 6n + 20p + 16p^2 - 8np + 6$$

$$h_n = \left[b(b-1) + 2(-b + 5p + 4p^2 - 2np)\right] + 3$$

Note that the number in square brackets is always even; thus, h_n is odd. Consequently, for any n,

$$\exp\left(-\imath\pi h_n\right) = -1$$

The claim then follows from the definition of $|\psi(t)\rangle$. $\qquad\square$

Case 3. *Let N be even. Then,*

$$|\psi(\tau)\rangle = \sum_{n=0}^{N} a_n\, e^{-\imath\epsilon_n \tau/\hbar}\, |E_n\rangle$$

$$= \begin{cases} \sum_{n=0}^{N}(-1)^n a_n\, |E_n\rangle & \text{for } N = 4p + 4, \\ -\sum_{n=0}^{N}(-1)^n a_n\, |E_n\rangle & \text{for } N = 4p + 2, \end{cases}$$

with $p \in \mathbb{Z}_{\geq 0}$.

Proof. Let $q = N/2$. We have,

$$2h_n = n(n-1) + (2q-n)(2q-n-1) = 2n^2 + 4q^2 - 4nq - 2q$$

$$h_n = (n^2 - q) + 2(q^2 - nq) = (n^2 - q) + \text{even factor}$$

The factor $n^2 - q$ (and, by extension, h_n) is even if and only if n and q are of the same parity. Recall that q is even when $N = 4p + 4$ and odd when $N = 4p + 2$. Therefore,

$$\exp\left(-\frac{\iota \epsilon_n \tau}{\hbar}\right) = \exp(-\iota \pi h_n)$$

$$= \begin{cases} 1 & \text{if } N = 4p + 4 \text{ and } n \text{ is even or } N = 4p + 2 \text{ and } n \text{ is odd,} \\ -1 & \text{if } N = 4p + 4 \text{ and } n \text{ is odd or } N = 4p + 2 \text{ and } n \text{ is even.} \end{cases}$$

The claim follows immediately from the definition of $|\psi(t)\rangle$. $\qquad\square$

C.2   Revivals of the condensate fraction and EPR

Consider the two observables discussed in Chapter 3. The condensate fraction is given by the normalized largest eigenvalue of the single-particle density matrix,

$$c = \frac{1}{2N}\left(\rho_{11} + \rho_{22} + \sqrt{(\rho_{11} - \rho_{22})^2 + 4\rho_{12}\rho_{21}}\right), \tag{C.7}$$

where $\rho_{ij} = \langle \hat{a}_i^\dagger \hat{a}_j \rangle$. The entanglement measure EPR is,

$$\text{EPR} = \langle \hat{a}_1^\dagger \hat{a}_2 \rangle \langle \hat{a}_2^\dagger \hat{a}_1 \rangle - \langle \hat{a}_1^\dagger \hat{a}_1 \hat{a}_2^\dagger \hat{a}_2 \rangle. \tag{C.8}$$

In this section, we show that these observables take the same values at time $t = \tau = \pi \hbar / U$ as at $t = 0$, regardless of the value of N. For N odd, this follows immediately from the results of the first section of this Appendix, so assume N even.

Consider first the condensate fraction. We have,

$$\rho_{ij}(t = 0) = \sum_n \sum_m a_n^* a_m \langle E_n | \hat{a}_i^\dagger \hat{a}_j | E_m \rangle$$

and, by the result proven in the first section,

$$\rho_{ij}(t = \tau) = \sum_n \sum_m (-1)^{n+m} a_n^* a_m \langle E_n | \hat{a}_i^\dagger \hat{a}_j | E_m \rangle .$$

At $J = 0$ the energy eigenstates are the Fock states, so the components of ρ can be found immediately:

$$\rho_{11}(t = \tau) = \sum_n \sum_m (-1)^{n+m} a_n^* a_m n \delta_{n,m} = \sum_n (-1)^{2n} |a_n|^2 n = \sum_n |a_n|^2 n = \rho_{11}(t = 0)$$

$$\rho_{22}(t = \tau) = \rho_{22}(t = 0) \quad \text{(analogously)}$$

$$\rho_{12}(t = \tau) = \sum_{n,m} (-1)^{n+m} a_n^* a_m \sqrt{(m + 1)(N - m)} \delta_{n,m+1}$$

$$= \sum_n (-1)^{2n-1} a_n^* a_{n-1} \sqrt{n(N - n + 1)} = -\sum_n a_n^* a_{n-1} \sqrt{n(N - n + 1)}$$

$$= -\rho_{12}(t = 0)$$

$$\rho_{21}(t = \tau) = -\rho_{21}(t = 0) \quad \text{(Hermiticity)}$$

Note that $\rho(t = \tau)$ differs from $\rho(t = 0)$ only in the sign of the off-diagonal elements. But these elements enter the condensate fraction only through their product (cf. Equation C.7). Therefore, $c(t = \tau) = c(t = 0)$.

The argument for EPR is similar. The first term in Eq. C.8 is equal to $\rho_{12}\rho_{21}$, and so the same at $t = \tau$ as at $t = 0$; the second term is equal to $N_1 N_2$, the product of the wells' populations, and so independent of time. Therefore, $\text{EPR}(t = \tau) = \text{EPR}(t = 0)$.

C.3   Perturbation about the $J \to 0$ limit

In this Appendix, we derive the perturbative corrections to the $J = 0$ mean-field and quantum revival frequencies (Equation 3.7).

It is convenient to rescale the problem by dividing all energies by NU. Then, the unperturbed Hamiltonian is given by,

$$H_0 = \frac{1}{2N} \left(\hat{a}_1^\dagger \hat{a}_1^\dagger \hat{a}_1 \hat{a}_1 + \hat{a}_2^\dagger \hat{a}_2^\dagger \hat{a}_2 \hat{a}_2 \right) \tag{C.9}$$

and is its representation in the Fock basis is,

$$\begin{pmatrix} \frac{N(N-1)}{2N} & & & & \\ & \frac{(N-1)(N-2)}{2N} & & & \\ & & \frac{(N-2)(N-3)}{2N} + \frac{1}{N} & & \\ & & & \ddots & \\ & & & & \frac{N(N-1)}{2N} \end{pmatrix} \tag{C.10}$$

As in Chapter 3, we will denote the diagonal entries ε_0, ε_1, and so on; because of the rescaling of the Hamiltonian, $\epsilon_i = NU\varepsilon_i$. The perturbed Hamiltonian is

$$H = H_0 + \frac{J}{NU} \left(-\hat{a}_1^\dagger \hat{a}_2 - \hat{a}_2^\dagger \hat{a}_1 \right) \equiv H_0 + \lambda V \tag{C.11}$$

and the Fock basis representation of V is the tridiagonal matrix,

$$- \begin{pmatrix} 0 & \sqrt{N} & & & \\ \sqrt{N} & 0 & \sqrt{2(N-1)} & & \\ & \sqrt{2(N-1)} & 0 & \sqrt{3(N-2)} & \\ & & & \ddots & \\ & & & \sqrt{N} & 0 \end{pmatrix} \tag{C.12}$$

Let P be a projection operator onto a subspace corresponding to a set of degenerate levels of H_0. Number the levels $n = 0, 1, 2, \ldots$, as in the main text; then, this operator is

represented by a matrix with only two nonzero entries, $P_{n+1,n+1} = P_{N+1-n,N+1-n} = 1$. Degenerate perturbation theory can be used to show that the kth order corrections to the level energies, $\epsilon^{(k)}$, are the eigenvalues of the matrix (Bernstein et al., 1990),

$$PW_kP \tag{C.13}$$

where the first few W_k matrices are

$$
\begin{aligned}
W_1 &= V, \\
W_2 &= -VL^{-1}V, \\
W_3 &= V(L^{-1}V)^2, \\
W_4 &= -V(L^{-1}V)^3 - \epsilon^{(2)}V(L^{-1})^2V,
\end{aligned}
\tag{C.14}
$$

with L^{-1} represented by a diagonal matrix with entries,

$$
(L^{-1})_{ll} = \begin{cases} 1/(H_0 - \epsilon^{(0)}I)_{ll} & \text{if } (H_0 - \epsilon^{(0)}I)_{ll} \neq 0, \\ 0 & \text{otherwise,} \end{cases}
\tag{C.15}
$$

where $\epsilon^{(0)}$ are the unperturbed energies.

Since V has no diagonal entries, PW_1P is a matrix of zeroes and there are no first-order corrections. (That $\epsilon^{(1)} = 0$ is used in the expressions for W_3 and W_4 in Eq. C.14, which would otherwise contain terms proportional to $\epsilon^{(1)}$.) The second order corrections can

be computed using the matrix W_2. Its nonzero entries are,

$$
(W_2)_{ij} = \begin{cases}
-N/(\varepsilon_1 - \varepsilon_n) & \text{for } i = j = N + 1 \text{ or } i = j = 1, \\[2ex]
-\frac{(i-1)(N+2-i)}{\varepsilon_{i-1}-\varepsilon_n} - \frac{i(N+1-i)}{\varepsilon_i-\varepsilon_n} & \text{for other } i = j, \\[2ex]
-\sqrt{i(i+1)(N+1-i)(N-i)}/(\varepsilon_{i+1} - \varepsilon_n) & \text{for } j = i + 2, \\[2ex]
-\sqrt{j(j+1)(N+1-j)(N-j)}/(\varepsilon_{j+1} - \varepsilon_n) & \text{for } j = i - 2.
\end{cases}
$$

$$\text{(C.16)}$$

where n is the index of the level considered.

Recall that the degenerate states are those corresponding to rows i and $N + 1 - i$, for $i = 1, 2, \ldots$. Since W_2 has nonzero entries only on the main diagonal and the ± 2 diagonals, the projection onto the subspace of degenerate levels PW_2P may have off-diagonal entries only for the second-lowest energy level. Conversely, if $N \gg 1$, the second-order corrections to the higher energy levels are given by the corresponding diagonal entries of W_2. The corrections to the three highest-energy levels up to second order are given by,

$$
\begin{aligned}
\varepsilon_0 &\to \varepsilon_0 - \frac{N}{\varepsilon_1 - \varepsilon_0} \left(\frac{J}{NU}\right)^2 \varepsilon_0 + \frac{N^2}{N-1} \left(\frac{J}{NU}\right)^2 \\
\varepsilon_1 &\to \varepsilon_1 - \left(\frac{N}{\varepsilon_0 - \varepsilon_1} + \frac{2(N-1)}{\varepsilon_2 - \varepsilon_1}\right) \left(\frac{J}{NU}\right)^2 \varepsilon_1 + \frac{N(N^2 - N + 1)}{(N-3)(N-1)} \left(\frac{J}{NU}\right)^2 \\
\varepsilon_2 &\to \varepsilon_2 - \left(\frac{2(N-1)}{\varepsilon_1 - \varepsilon_2} + \frac{3(N-2)}{\varepsilon_3 - \varepsilon_2}\right) \left(\frac{J}{NU}\right)^2 \varepsilon_2 + \frac{N(N^2 - 3N + 8)}{(N-5)(N-3)} \left(\frac{J}{NU}\right)^2
\end{aligned}
$$

$$\text{(C.17)}$$

After substituting in the entries of the unperturbed Hamiltonian matrix (Equation C.10) for the unperturbed energies ε_i, these expressions lead immediately to Equation 3.7.

Consider now the third-order corrections to the energies, determined by the matrix W_3. Except for the lowest-lying states, there are no off-diagonal entries in PW_3P; this follows from the central result of Bernstein et al. (1990), since off-diagonal entries would break the degeneracy the authors prove to hold to Nth order of perturbation theory.

Therefore, the third-order corrections to the energies are given by the diagonal entries of the matrix W_3. As we show below, these entries are all zero, and thus there are no corrections of this order.

Let A be a matrix. We will call A an *odd matrix* if $A_{i,i+p} = 0$ for all i and all p even (including $p = 0$), and an *even matrix* if $A_{i,i+p} = 0$ for all i and all p odd. Even and odd matrices have the following properties under multiplication which provide the motivation for our terminology:

Lemma 1. *Let A and B be odd $N \times N$ matrices. Then, AB is an even matrix.*

Proof. Let n be an odd integer.

$$(AB)_{i,i+n} = \sum_{k=1}^{N} A_{i,k} B_{k,i+n} = \sum_{p=1-i}^{N-i} A_{i,i+p} B_{i+p,i+n}$$

Since A is an odd matrix, we may restrict the sum to odd p (the other entries are zero):

$$(AB)_{i,i+n} = \sum_{p \text{ odd}} A_{i,i+p} B_{i+p,i+n}$$

Let $m = i + p$.

$$B_{i+p,i+n} = B_{m,m+n-p}$$

Since p is odd and n odd, $n - p$ is even and so $B_{i+p,i+n} = 0$ because B is an odd matrix. Thus,

$$(AB)_{i,i+n} = 0$$

for n odd, and AB is an even matrix. □

Lemma 2. *Let A be an odd $N \times N$ matrix and C an even $N \times N$ matrix. Then, AC and CA are odd matrices.*

Proof. Let n be an even integer. Proceeding as before,

$$(AC)_{i,i+n} = \sum_{k=1}^{N} A_{i,k} C_{k,i+n} = \sum_{p=1-i}^{N-i} A_{i,i+p} C_{i+p,i+n}$$

$$= \sum_{p \text{ odd}} A_{i,i+p} C_{i+p,i+n}.$$

Let $m = i + p$.

$$C_{i+p,i+n} = C_{m,m-p+n}.$$

Since p is odd and n is even, $n - p$ is odd. Since C is an even matrix, $C_{i+p,i+n} = 0$ and

$$(AC)_{i,i+n} = 0$$

for n even, proving that AC is an odd matrix. The proof for CA is analogous. □

The matrix V is odd, while the matrix L^{-1} is even. By the lemmas above, $W_3 = V(L^{-1}V)(L^{-1}V)$ must be odd. The diagonal entries of an odd matrix are all zero. This implies there are no third-order corrections to the energies, except for the lowest few energy levels. Incidentally, the same argument can be used to show that the fifth-order corrections are zero.

Appendix D

Derivation of the magnetron master equation

In this Appendix, we derive the master equation describing the AC operation of a magnetron, Equation 4.23.

We start from the Schrödinger equation for the system density matrix written in the interaction frame,

$$\frac{d\rho}{dt} = -\text{Tr}_E \int_0^t dt' [\hat{V}_I(t), [\hat{V}_I(t'), \rho_{\text{tot}}(t')]]. \tag{D.1}$$

Here, ρ is the system density matrix, ρ_{tot} is the density matrix for the system plus environment, and Tr_E indicates a trace over the environment degrees of freedom. The interaction picture coupling $\hat{V}_I$ is related to the Schrödinger picture coupling $\hat{V}$ of Equation 4.22 by,

$$\hat{V}_I = e^{-\imath(\hat{H}_{\text{eff}}+\hat{H}_E)t} \hat{V} e^{\imath(\hat{H}_{\text{eff}}+\hat{H}_E)t}$$

$$= \sum_n \sum_\mu \gamma_{n\mu} e^{\imath\hat{H}_{\text{eff}}t} (\hat{c}_n + \hat{c}_n^\dagger) e^{-\imath\hat{H}_{\text{eff}}t} e^{\imath\hat{H}_E t} (\hat{r}_\mu + \hat{r}_\mu^\dagger) e^{-\imath\hat{H}_E t}.$$

Equation D.1 is exact.

Our first step will be to rewrite the coupling operator $\hat{V}_I$ in a simpler form.

D.1 Coupling in the interaction picture

For the environment operators, the anticommutation relations (Equation 4.20) imply,

$$[\imath \hat{H}_E t,\, \hat{r}_\mu] = -\imath t \varepsilon_\mu \hat{r}_\mu$$

and so by the Trotter formula,

$$\hat{V}_I = \sum_n \sum_\mu \gamma_{n\mu} e^{\imath \hat{H}_{\text{eff}} t} (\hat{c}_n + \hat{c}_n^\dagger) e^{-\imath \hat{H}_{\text{eff}} t} \left(\hat{r}_\mu e^{-\imath \varepsilon_\mu t} + \hat{r}_\mu^\dagger e^{\imath \varepsilon_\mu t} \right). \tag{D.2}$$

We would like to similarly replace the system operator exponentials with phases, but the commutator $[\hat{H}_{\text{eff}},\, \hat{c}_n]$ is not simply proportional to $\hat{c}_n$, so this is not possible. Instead, we will rewrite $\hat{V}_I$ in terms of dressed analogs of the system and bath annihilation operators.

Let $|j\rangle$ be an eigenstate of the system Hamiltonian $\hat{H}_{\text{eff}}$. We choose the system eigenstates to be simultaneous eigenstates of the electron number operator $\sum_n \hat{c}_n \hat{c}_n^\dagger$. A resolution of the identity for the Hilbert space of the system is $\sum_j |j\rangle \langle j| = \hat{1}$. Inserting it twice, after the system time evolution operators,

$$\hat{V}_I = \sum_n \sum_\mu \sum_{j,k} \gamma_{n\mu} X_{jk}^{(n)} |j\rangle \langle k| \left(\hat{r}_\mu e^{-\imath \varepsilon_\mu t} + \hat{r}_\mu^\dagger e^{\imath \varepsilon_\mu t} \right) e^{\imath \Delta_{jk} t}$$

where

$$\Delta_{jk} = \langle j| \hat{H}_{\text{eff}} |j\rangle - \langle k| \hat{H}_{\text{eff}} |k\rangle,$$

$$X_{jk}^{(n)} = \langle j| \hat{c}_n + \hat{c}_n^\dagger |k\rangle.$$

Since the system eigenstates were chosen to be simultaneous eigenstates of the electron number operator, $X_{jj}^{(n)} = 0$ for all j, n. We split the sum over k into two parts, with a view

towards performing a rotating wave approximation in the system-bath coupling:

$$\hat{V}_I = \sum_{n,\mu,j} \sum_{k:k>j} \gamma_{n\mu} X_{jk}^{(n)} |j\rangle \langle k| \left(\hat{r}_\mu e^{-\imath \varepsilon_\mu t} + \hat{r}_m u^\dagger e^{\imath \varepsilon_\mu t} \right) e^{\imath \Delta_{jk} t}$$

$$+ \sum_{n,\mu,j} \sum_{k:k<j} \gamma_{n\mu} X_{jk}^{(n)} |j\rangle \langle k| \left(\hat{r}_\mu e^{-\imath \varepsilon_\mu t} + \hat{r}_m u^\dagger e^{\imath \varepsilon_\mu t} \right) e^{\imath \Delta_{jk} t}.$$

Note that,

$$\sum_j \sum_{k:k<j} X_{jk}^{(n)} |j\rangle \langle k| e^{\imath \Delta_{jk} t} = \sum_k \sum_{j:j<k} X_{kj}^{(n)} |k\rangle \langle j| e^{-\imath \Delta_{jk} t}$$

$$= \sum_j \sum_{k:k>j} X_{kj}^{(n)} |k\rangle \langle j| e^{-\imath \Delta_{jk} t}$$

$$= \sum_j \sum_{k:k>j} X_{kj}^{(n)*} (|j\rangle \langle k|)^\dagger e^{-\imath \Delta_{jk} t},$$

so we may write,

$$\hat{V}_I = \sum_n \left(\hat{B}_n(t) + \hat{B}_n^\dagger(t) \right) \left(\hat{S}_n(t) + \hat{S}_n^\dagger(t) \right),$$

with

$$\hat{B}_n(t) = \sum_\mu \gamma_{n\mu} \hat{r}_\mu e^{-\imath \varepsilon_\mu t},$$

$$\hat{S}_n(t) = \sum_j \sum_{k:k>j} X_{jk}^{(n)} |j\rangle \langle k| e^{\imath \Delta_{jk} t}.$$

If we assume the system eigenstates are indexed in order of increasing electron number, so that $\hat{S}_n(t)$ is indeed a dressed annihilation operator, we may perform a rotating wave approximation in the system-bath interaction to obtain,

$$\hat{V}_I \approx \sum_n \hat{B}_n^\dagger(t) \hat{S}_n(t) + \hat{S}_n^\dagger(t) \hat{B}_n(t).$$

D.2 Born approximation and commutators of the coupling

As we have noted at the beginning of this Appendix, the evolution of the system density matrix is given by the equation,

$$\hat{V}_I = \sum_n \sum_\mu \gamma_{n\mu} e^{i\hat{H}_{\text{eff}}t}(\hat{c}_n + \hat{c}_n^\dagger)e^{-i\hat{H}_{\text{eff}}t}\left(\hat{r}_\mu e^{-i\varepsilon_\mu t} + \hat{r}_\mu^\dagger e^{i\varepsilon_\mu t}\right).$$

We now perform the Born approximation, replacing $\rho_{\text{tot}}(t')$ with $\rho(t') \otimes \rho_E(0)$ on the right-hand side. This is a weak-coupling approximation: although the system and environment become entangled as a result of their interaction, for the purposes of finding the effect of the environment on the system we will neglect any change in the environment's state. We obtain,

$$\frac{d\rho}{dt} = -\text{Tr}_E \int_0^t dt'[\hat{V}_I(t), [\hat{V}_I(t'), \rho(t') \otimes \rho_E(0)]].$$

We will now evaluate the commutators appearing on the right hand side of this equation.[1]

$$[\hat{V}_I(t'), \rho \otimes (t')\rho_E] = \sum_n \hat{S}_n^\dagger \rho \otimes \hat{B}_n \rho_E - \rho\hat{S}_n^\dagger \otimes \rho_E\hat{B}_n + \hat{S}_n\rho \otimes \hat{B}_n^\dagger\rho_E - \rho\hat{S}_n \otimes \rho_E\hat{B}_n^\dagger$$

---

[1]For clarity, we will drop the explicit time dependence of $\hat{S}$ and $\hat{B}$ (which can be inferred from the index: $m \to t, n \to t'$).

and

$$[\hat{V}_I(t), [\hat{V}_I(t'), \rho \otimes (t')\rho_E]] =$$

$$\sum_{m,n} \hat{S}_m^\dagger \hat{S}_n^\dagger \rho \otimes (\hat{B}_m \hat{B}_n \rho_E - \hat{B}_n \rho_E \hat{B}_m) + (\hat{S}_m^\dagger \hat{S}_n^\dagger \rho - \hat{S}_n^\dagger \rho \hat{S}_m^\dagger) \otimes \hat{B}_n \rho_E \hat{B}_m$$

$$- \hat{S}_m^\dagger \rho \hat{S}_n^\dagger \otimes (\hat{B}_m \rho_E \hat{B}_n - \rho_R \hat{B}_n \hat{B}_m) - (\hat{S}_m^\dagger \rho \hat{S}_n^\dagger - \rho \hat{S}_n^\dagger \hat{S}_m^\dagger) \otimes \rho_E \hat{B}_n \hat{B}_m$$

$$+ \hat{S}_m^\dagger \hat{S}_n \rho \otimes (\hat{B}_m \hat{B}_n^\dagger \rho_E - \hat{B}_n^\dagger \rho_E \hat{B}_m) + (\hat{S}_m^\dagger \hat{S}_n \rho - \hat{S}_n \rho \hat{S}_m^\dagger) \otimes \hat{B}_n^\dagger \rho_E \hat{B}_m$$

$$- \hat{S}_m^\dagger \rho \hat{S}_n \otimes (\hat{B}_m \rho_E \hat{B}_n^\dagger - \rho_E \hat{B}_n^\dagger \hat{B}_m) - (\hat{S}_m^\dagger \rho \hat{S}_n - \rho \hat{S}_n \hat{S}_m^\dagger) \otimes \rho_E \hat{B}_n^\dagger \hat{B}_m.$$

Now, assume the reservoir is in a thermal state. The trace of the first half of the terms is then zero, and

$$\text{Tr}_E [\hat{V}_I(t), [\hat{V}_I(t'), \rho \otimes (t')\rho_E]] = \sum_{m,n} \hat{S}_m^\dagger \hat{S}_n \rho \otimes \text{Tr}_E (\hat{B}_m \hat{B}_n^\dagger \rho_E) - \hat{S}_n \rho \hat{S}_m^\dagger \otimes \text{Tr}_E (\hat{B}_n^\dagger \rho_E \hat{B}_m)$$

$$- \hat{S}_m^\dagger \rho \hat{S}_n \otimes \text{Tr}_E (\hat{B}_m \rho_E \hat{B}_n^\dagger) + \rho \hat{S}_n \hat{S}_m^\dagger \otimes \text{Tr}_E (\rho_E \hat{B}_n^\dagger \hat{B}_m)$$

$$+ \text{h.c.}$$

The master equation can be written as a sum of four integrals (and their hermitian conjugates),

$$\frac{d\rho}{dt} = \sum_{m,n} \int_0^t dt' \quad \hat{S}_m^\dagger(t)\rho(t')\hat{S}_n(t')\langle \hat{B}_n^\dagger(t')\hat{B}_m(t)\rangle - \rho(t')\hat{S}_n(t')\hat{S}_m^\dagger(t)\langle \hat{B}_n^\dagger(t')\hat{B}_m(t)\rangle$$

$$+ \hat{S}_n(t')\rho(t')\hat{S}_m^\dagger(t)\langle \hat{B}_m(t)\hat{B}_n^\dagger(t')\rangle - \hat{S}_m^\dagger(t)\hat{S}_n(t')\rho(t')\langle \hat{B}_m(t)\hat{B}_n^\dagger(t')\rangle \qquad \text{(D.3)}$$

$$+ \text{h.c.}$$

where the bath correlation functions are,

$$\langle \hat{B}_n^\dagger(t')\hat{B}_m(t)\rangle = \text{Tr}_\text{E}\,(\hat{B}_n^\dagger(t')\hat{B}_m(t)\rho_\text{E}) = \text{Tr}_\text{E}\left(\sum_{\mu,\nu}\gamma_{n\mu}^*\gamma_{m\nu}e^{-\iota\varepsilon_\nu t'-\varepsilon_\mu t}\right)$$

$$= \sum_k n_k\gamma_{nk}^*\gamma_{mk}e^{-\iota\varepsilon_k(t-t')}.$$

with n_k the Fermi factor of bath level k (and $\langle \hat{B}_m(t)\hat{B}_n^\dagger(t')\rangle$ defined analogously). Because we are working in two dimensions, the reservoir density of states is a constant, $\sigma(\omega) = \sigma$. Converting a sum over the levels into an integral over energies,

$$\langle \hat{B}_n^\dagger(t')\hat{B}_m(t)\rangle = \int d\omega\, \sigma\gamma_n^*(\omega)\gamma_m(\omega)e^{-\iota\omega(t-t')}n(\omega),$$

$$\langle \hat{B}_m(t)\hat{B}_n^\dagger(t')\rangle = \int d\omega\, \sigma\gamma_n^*(\omega)\gamma_m(\omega)e^{-\iota\omega(t-t')}(1-n(\omega)).$$

D.3 Simplifying the master equation

To make further progress, it is necessary to make additional approximations. Consider the first integral in Equation D.3 (the other integrals can be treated analogously). If we assume that the bath correlation functions are memoryless (depend on t and t' only through $\tau = t'-t$) and make the Markov approximation by replacing the upper limit of integration with ∞,

$$I_1 = \int_0^t dt'\, \hat{S}_m^\dagger(t)\rho(t')\hat{S}_n(t')\langle \hat{B}_n^\dagger(t')\hat{B}_m(t)\rangle$$

$$= \int_0^t d\tau\, \hat{S}_m^\dagger(t)\rho(t-\tau)\hat{S}_n(t-\tau)\langle \hat{B}_n^\dagger(\tau)\hat{B}_m(0)\rangle$$

$$= \int_0^\infty d\tau\, \hat{S}_m^\dagger(t)\rho(t)\hat{S}_n(t-\tau)\langle \hat{B}_n^\dagger(\tau)\hat{B}_m(0)\rangle$$

Expanding the operators $\hat{S}$ and $\hat{B}$,

$$I_1 = \int_0^\infty d\tau \sum_j \sum_{k:k>j} \sum_l \sum_{p:p>l} X_{jk}^{(m)*} X_{lp}^{(n)} |k\rangle \langle j| \rho |l\rangle \langle p| e^{\iota(\Delta_{lp} - \Delta_{jk})t}$$
$$\times \int d\omega \, \sigma \gamma_n^*(\omega) \gamma_m(\omega) e^{-\iota(\omega - \Delta_{lp})\tau} n(\omega).$$

The real part of I_1 contributes to the decay rate, while the imaginary part is the frequency shift. We will ignore the frequency shift, and taking advantage of,

$$\mathfrak{R} \int_0^\infty e^{-\iota\omega t} \, dt = \pi\delta(\omega),$$

will write,

$$I_1 = \sum_j \sum_{k:k>j} \sum_l \sum_{p:p>l} X_{jk}^{(m)*} X_{lp}^{(n)} |k\rangle \langle j| \rho |l\rangle \langle p| e^{\iota(\Delta_{lp} - \Delta_{jk})t} \pi \sigma \gamma_n^*(\Delta_{lp}) \gamma_m(\Delta_{lp}) n(\Delta_{lp}).$$

We will now make a second rotating wave approximation. The usual way of doing so would be to drop all terms for which $\Delta_{lp} \neq \Delta_{jk}$. We will make the milder approximation of replacing Δ_{lp} with Δ_{jk} in the argument of γ_m in the expression above. This allows us to write,

$$I_1 = \sum_j \sum_{k:k>j} \sum_l \sum_{p:p>l} \frac{1}{2} \hat{A}_{jk}^{(m)\dagger} \rho \hat{A}_{lp}^{(n)} e^{\iota(\Delta_{lp} - \Delta_{jk})t} n(\Delta_{lp}), \tag{D.4}$$

where we have defined

$$\hat{A}_{jk}^{(m)} = \sqrt{2\pi\sigma} X_{jk}^{(m)} \gamma_m(\Delta_{jk}) |j\rangle \langle k|.$$

Performing analogous manipulations for the remaining three integrals in Equation D.3, we obtain,

$$I_2 = \sum_j \sum_{k:k>j} \sum_l \sum_{p:p>l} \frac{1}{2} \rho \hat{A}_{lp}^{(n)} \hat{A}_{jk}^{(m)\dagger} e^{\iota(\Delta_{lp}-\Delta_{jk})t} n(\Delta_{lp}),$$

$$I_3 = \sum_j \sum_{k:k>j} \sum_l \sum_{p:p>l} \frac{1}{2} \hat{A}_{lp}^{(n)} \rho \hat{A}_{jk}^{(m)\dagger} e^{\iota(\Delta_{lp}-\Delta_{jk})t} (1 - n(\Delta_{lp})),$$

$$I_4 = \sum_j \sum_{k:k>j} \sum_l \sum_{p:p>l} \frac{1}{2} \hat{A}_{jk}^{(m)\dagger} \hat{A}_{lp}^{(n)} \rho e^{\iota(\Delta_{lp}-\Delta_{jk})t} (1 - n(\Delta_{lp})).$$

Now, assume that the anode only absorbs (never emits) electrons. This means the relevant energy levels of the anode are unoccupied, or $n(\Delta_{lp}) = 0$ for all l, p. The master equation is then,

$$\frac{d\rho}{dt} = \sum_{m,n} \sum_j \sum_{k:k>j} \sum_l \sum_{p:p>l} \frac{1}{2} e^{\iota(\Delta_{lp}-\Delta_{jk})t} (\hat{A}_{lp}^{(n)} \rho \hat{A}_{jk}^{(m)\dagger} - \hat{A}_{jk}^{(m)\dagger} \hat{A}_{lp}^{(n)} \rho) + \text{h.c.}$$

Recall that this is the equation for the density matrix in the interaction picture. The Schödinger picture evolution of the density matrix is given by,

$$\frac{d\rho_S}{dt} = -\iota[\hat{H}_{\text{eff}}, \rho_S] + e^{-\iota\hat{H}_{\text{eff}}t} \dot{\rho} e^{\iota\hat{H}_{\text{eff}}t}. \tag{D.5}$$

Since the sums over the states in the $d\rho/dt$ equations above are over eigenstates of $\hat{H}_{\text{eff}}$, the exponential factors cancel:

$$\frac{d\rho_S}{dt} = -\iota[\hat{H}_{\text{eff}}, \rho_S] + \sum_{m,n} \sum_j \sum_{k:k>j} \sum_l \sum_{p:p>l} \frac{1}{2} (\hat{A}_{lp}^{(n)} \rho_S \hat{A}_{jk}^{(m)\dagger} - \hat{A}_{jk}^{(m)\dagger} \hat{A}_{lp}^{(n)} \rho_S) + \text{h.c.}$$

Let,

$$\hat{A} = \sum_n \sum_j \sum_{k:k>j} \hat{A}_{jk}^{(n)}.$$

In terms of this operator,

$$\dot{\rho}_S = -\imath[\hat{H}_{\text{eff}}, \rho_S] + \hat{A}\rho_S\hat{A}^\dagger - \frac{1}{2}\left(\hat{A}^\dagger\hat{A}\rho_S + \rho_S\hat{A}^\dagger\hat{A}\right),$$

which is Equation 4.23. Let us examine the operator $\hat{A}$:

$$\hat{A} = \sum_{n=0}^{\infty}\sum_{j}\sum_{k:k>j} \sqrt{2\pi\sigma}\, \langle j|\, \hat{c}_n + \hat{c}_n^\dagger\, |k\rangle\, \gamma(\Delta_{jk})\, |j\rangle\langle k| .$$

We have ordered the eigenstates by their electron number, so that in this sum $|k\rangle$ is always a state with at least as many electrons as $|j\rangle$. Consequently, $\langle j|\, \hat{c}_n^\dagger\, |k\rangle = 0$, and

$$\hat{A} = \sqrt{2\pi\sigma}\sum_{n=0}^{\infty}\sum_{j}\sum_{k:k>j} \gamma_n(\Delta_{jk})\, |j\rangle\langle j|\, \hat{c}_n\, |k\rangle\langle k| .$$

If we strengthen our second rotating wave approximation (recall the discussion preceding Equation D.4) by assuming not merely $\gamma_n(\Delta_{lp}) \approx \gamma_n(\Delta_{jk})$, but that γ_n is independent of energy, then this expression can be simplified to,

$$\hat{A} = \sqrt{2\pi\sigma}\sum_{n=0}^{\infty} \gamma_n\hat{c}_n,$$

which is Equation 4.24.

Bibliography

Abdullaev, F., Baizakov, B., Darmanyan, S., Konotop, V., and Salerno, M. (2001). Nonlinear excitations in arrays of Bose–Einstein condensates. *Physical Review A*, 64(4):043606.

Albiez, M., Gati, R., Fölling, J., Hunsmann, S., Cristiani, M., and Oberthaler, M. K. (2005). Direct Observation of Tunneling and Nonlinear Self-Trapping in a Single Bosonic Josephson Junction. *Physical Review Letters*, 95(1):010402.

Anderson, M. H., Ensher, J. R., Matthews, M. R., Wieman, C. E., and Cornell, E. A. (1995). Observation of Bose–Einstein condensation in a dilute atomic vapor. *Science*, 269(5221):198–201.

Andrews, M. R., Townsend, C. G., Miesner, H.-J., Durfee, D. S., Kurn, D. M., and Ketterle, W. (1997). Observation of Interference Between Two Bose Condensates. *Science*, 275(5300):637–641.

Anglin, J. (1997). Cold, Dilute, Trapped Bosons as an Open Quantum System. *Physical Review Letters*, 79(1):6–9.

Arecchi, F., Courtens, E., Gilmore, R., and Thomas, H. (1972). Atomic Coherent States in Quantum Optics. *Physical Review A*, 6(6):2211–2237.

Asada, M. (2003). Quantum theory of a semiconductor klystron. *Physical Review B*, 67(11):115303.

Bakr, W. S., Gillen, J. I., Peng, A., Fölling, S., and Greiner, M. (2009). A quantum gas microscope for detecting single atoms in a Hubbard-regime optical lattice. *Nature*, 462(7269):74–7.

Beaudoin, F., Gambetta, J. M., and Blais, A. (2011). Dissipation and ultrastrong coupling in circuit QED. *Physical Review A*, 84(4):043832.

Becker, C., Stellmer, S., Soltan-Panahi, P., Dörscher, S., Baumert, M., Richter, E.-M., Kronjäger, J., Bongs, K., and Sengstock, K. (2008). Oscillations and interactions of dark and dark-bright solitons in Bose–Einstein condensates. *Nature Physics*, 4(6):496–501, arXiv:0804.0544.

Bernstein, L., Eilbeck, J. C., and Scott, A. C. (1990). The quantum theory of local modes in a coupled system of nonlinear oscillators. *Nonlinearity*, 3(2):293–323.

Bose, S. N. (1924). Plancks Gesetz und Lichtquantenhypothese. *Zeitschrift fuer Physik*, 26(1):178–181.

Bradley, C. C., Sackett, C. A., Tollett, J. J., and Hulet, R. G. (1995). Evidence of Bose–Einstein condensation in an atomic gas with attractive interactions. *Physical Review Letters*, 75(9):1687–1690.

Breuer, H.-P. and Petruccione, F. (2002). *The Theory of Open Quantum Systems*. Oxford University Press.

Brif, C. and Mann, A. (1999). Phase-space formulation of quantum mechanics and quantum-state reconstruction for physical systems with Lie-group symmetries. *Physical Review A*, 59(2):971–987, arXiv:9809052.

Carmichael, H. (1993). *An Open Systems Approach to Quantum Optics*. Springer-Verlag, New York.

Carr, L. D., Dounas-Frazer, D. R., and Garcia-March, M. a. (2010). Dynamical realization of macroscopic superposition states of cold bosons in a tilted double well. *EPL (Europhysics Letters)*, 90(1):10005.

Castin, Y. (2000). Bose–Einstein Condensates in Atomic Gases: Simple Theoretical Results. In *Coherent atomic matter waves*, page 146. Springer Berlin Heidelberg, Berlin, Heidelberg.

Child, M. S. (1991). *Semiclassical mechanics with molecular applications*. Oxford University Press, New York.

Chin, C., Grimm, R., Julienne, P., and Tiesinga, E. (2010). Feshbach resonances in ultracold gases. *Reviews of Modern Physics*, 82(2):1225–1286.

Chuchem, M., Smith-Mannschott, K., Hiller, M., Kottos, T., Vardi, A., and Cohen, D. (2010). Quantum dynamics in the bosonic Josephson junction. *Physical Review A*, 82(5):053617.

Cirac, J. I., Lewenstein, M., Mølmer, K., and Zoller, P. (1998). Quantum superposition states of Bose–Einstein condensates. *Physical Review A*, 57(2):1208–1218, arXiv:9706034.

Cirac, J. I., Schenzle, A., and Zoller, P. (1994). Inhibition of Quantum Tunneling of an Atom due to the Continuous Observation of Light Scattering. *Europhysics Letters (EPL)*, 27(2):123–128.

Collins, G. B., editor (1964). *Microwave Magnetrons*. Boston Technical Publishers, Lexington, MA.

Dalfovo, F., Giorgini, S., Pitaevskii, L. P., and Stringari, S. (1999). Theory of Bose–Einstein condensation in trapped gases. *Reviews of Modern Physics*, 71(3):463–512, arXiv:9806038.

Dalibard, J., Castin, Y., and Molmer, K. (1992). Wave-function approach to dissipative processes in quantum optics. *Physical Review Letters*, 68(5):580–583.

Datta, S. (2000). Nanoscale device modeling: the Green's function method. *Superlattices and Microstructures*, 28(4):253–278.

Datta, S. (2005). *Quantum Transport: Atom to Transistor.* Cambridge University Press.

Davis, K. B., Mewes, M. O., Andrews, M. R., Van Druten, N. J., Durfee, D. S., Kurn, D. M., and Ketterle, W. (1995). Bose–Einstein condensation in a gas of sodium atoms. *Physical Review Letters*, 75(22):3969–3973.

Dounas-Frazer, D., Hermundstad, A., and Carr, L. (2007). Ultracold Bosons in a Tilted Multilevel Double-Well Potential. *Physical Review Letters*, 99(20):200402.

Du, X., Skachko, I., Barker, A., and Andrei, E. Y. (2008). Approaching ballistic transport in suspended graphene. *Nature Nanotechnology*, 3(8):491–5.

Einstein, A. (1924). Quantentheorie des einatomigen idealen Gases. *Sitzungsber. Kgl. Preuss. Akad. Wiss*, 261:3.

Enol'skii, V., Salerno, M., Scott, A., and Eilbeck, J. (1992). There's more than one way to skin Schrödinger's cat. *Physica D: Nonlinear Phenomena*, 59(1-3):1–24.

Enol'skii, V. Z., Salerno, M., Kostov, N. A., and Scott, A. C. (1991). Alternate quantizations of the discrete self-trapping dimer. *Physica Scripta*, 43(3):229–235.

Freericks, J. and Monien, H. (1996). Strong-coupling expansions for the pure and disordered Bose–Hubbard model. *Physical Review B*, 53(5):2691–2700.

Gericke, T., Würtz, P., Reitz, D., Langen, T., and Ott, H. (2008). High-resolution scanning electron microscopy of an ultracold quantum gas. *Nature Physics*, 4(12):949–953.

Gilmour, A. S. (2011). *Klystrons, Traveling Wave Tubes, Magnetrons, Cross-Field Amplifiers, and Gyrotrons.* Artech House, Norwood, MA.

Glick, A., Lipkin, H., and Meshkov, N. (1965). Validity of many-body approximation methods for a solvable model. *Nuclear Physics*, 62(2):211–224.

Graefe, E. and Korsch, H. J. (2007). Semiclassical quantization of an N-particle Bose–Hubbard model. *Physical Review A*, 76(3):032116.

Graefe, E.-M., Korsch, H. J., and Strzys, M. P. (2014). Bose–Hubbard dimers, Viviani's windows and pendulum dynamics. *Journal of Physics A: Mathematical and Theoretical*, 47(8):085304.

Greiner, M., Mandel, O., Esslinger, T., Hänsch, T. W., and Bloch, I. (2002a). Quantum phase transition from a superfluid to a Mott insulator in a gas of ultracold atoms. *Nature*, 415(6867):39–44.

Greiner, M., Mandel, O., Hänsch, T. W., and Bloch, I. (2002b). Collapse and revival of the matter wave field of a Bose–Einstein condensate. *Nature*, 419(6902):51–4.

Gribnikov, Z. S., Vagidov, N. Z., Mitin, V. V., and Haddad, G. I. (2003). Ballistic and quasiballistic tunnel transit time oscillators for the terahertz range: Linear admittance. *Journal of Applied Physics*, 93(9):5435.

Grišins, P., Rauer, B., Langen, T., Schmiedmayer, J., and Mazets, I. E. (2016). Degenerate Bose gases with uniform loss. *Physical Review A*, 93(3):033634, 1411.4946.

Halperin, B. I. (1982). Quantized Hall conductance, current-carrying edge states, and the existence of extended states in a two-dimensional disordered potential. *Physical Review B*, 25(4):2185–2190.

Hastie, T., Tibshirani, R., and Friedman, J. (2009). *The Elements of Statistical Learning: Data Mining, Inference, and Prediction.* Springer-Verlag, New York, 5th printi edition.

He, Q. Y., Reid, M. D., Vaughan, T. G., Gross, C., Oberthaler, M., and Drummond, P. D. (2011). Einstein-Podolsky-Rosen Entanglement Strategies in Two-Well Bose–Einstein Condensates. *Physical Review Letters*, 106(12):120405.

Hennig, H., Dorignac, J., and Campbell, D. (2010). Transfer of Bose–Einstein condensates through discrete breathers in an optical lattice. *Physical Review A*, 82(5):053604.

Hennig, H., Witthaut, D., and Campbell, D. K. (2012). Global phase space of coherence and entanglement in a double-well Bose–Einstein condensate. *Physical Review A*, 86(5):051604.

Henon, M. (1982). On the numerical computation of Poincaré maps. *Physica D: Nonlinear Phenomena*, 5(2-3):412–414.

Hillery, M. and Zubairy, M. (2006). Entanglement Conditions for Two-Mode States. *Physical Review Letters*, 96(5):050503, arXiv:0507168v2.

Howard, J. (2013). Stability of Hamiltonian equilibria. *Scholarpedia*, 8(10):3627.

Hull, A. W. (1928). Gas-Filled Thermionic Tubes. *Transactions of the American Institute of Electrical Engineers*, 47(3):753–763.

Itin, A. P. and Schmelcher, P. (2011). Semiclassical spectrum of small Bose–Hubbard chains: A normal-form approach. *Physical Review A*, 84(6):063609.

Jaksch, D., Bruder, C., Cirac, J., Gardiner, C., and Zoller, P. (1998). Cold Bosonic Atoms in Optical Lattices. *Physical Review Letters*, 81(15):3108–3111.

Jose, J. V. and Saletan, E. J. (1998). *Classical Dynamics: A Contemporary Approach*. Cambridge University Press, Cambridge, UK.

Kordas, G., Wimberger, S., and Witthaut, D. (2012). Dissipation-induced macroscopic entanglement in an open optical lattice. *EPL (Europhysics Letters)*, 100(3):30007.

Landau, L. D. and Lifshitz, E. M. (1981). *Quantum Mechanics (Nonrelativistic Theory)*. Butterworth-Heinemann, 3rd ed edition.

Lee, H.-w. (1995). Theory and application of the quantum phase-space distribution functions. *Physics Reports*, 259(3):147–211.

Leggett, A. (2001). Bose–Einstein condensation in the alkali gases: Some fundamental concepts. *Reviews of Modern Physics*, 73(2):307–356.

Liang, G., Neophytou, N., Nikonov, D. E., and Lundstrom, M. S. (2007). Performance projections for ballistic graphene nanoribbon field-effect transistors. *IEEE Transactions on Electron Devices*, 54(4):677–682.

Lindblad, G. (1976). On the generators of quantum dynamical semigroups. *Communications in Mathematical Physics*, 48(2):119–130.

Links, J. (2006). Bethe Ansatz Solutions of the Bose–Hubbard Dimer. *Symmetry, Integrability and Geometry: Methods and Applications*, 2.

Links, J., Zhou, H.-q., McKenzie, R. H., and Gould, M. D. (2003). Algebraic Bethe ansatz method for the exact calculation of energy spectra and form factors: applications to models of Bose Einstein condensates and metallic nanograins. *Journal of Physics A: Mathematical and General*, 36(19):R63–R104.

Lipkin, H., Meshkov, N., and Glick, A. (1965). Validity of many-body approximation methods for a solvable model. *Nuclear Physics*, 62(2):188–198.

Liu, C. T., Lin, S. Y., Tsui, D. C., Lee, H., and Ackley, D. (1988). Cyclotron resonance measurements of electron effective mass in strained AlGaAs/InGaAs/GaAs pseudomorphic structures. *Applied Physics Letters*, 53(25):2510.

London, F. (1938). On the Bose–Einstein condensation. *Physical Review*, 54(11):947–954.

Ma, L. (2004). *3D Computer Modeling of Magnetrons*. Doctoral dissertation, University of London.

Marcuse, D. (1980). *Principles of Quantum Electronics*. Academic Press, New York.

Matthews, M. R., Anderson, B. P., Haljan, P. C., Hall, D. S., Wieman, C. E., and Cornell, E. A. (1999). Vortices in a Bose–Einstein Condensate. *Physical Review Letters*, 83(13):2498–2501, arXiv:9908209.

Mayorov, A. S., Gorbachev, R. V., Morozov, S. V., Britnell, L., Jalil, R., Ponomarenko, L. A., Blake, P., Novoselov, K. S., Watanabe, K., Taniguchi, T., and Geim, A. K. (2011). Micrometer-Scale Ballistic Transport in Encapsulated Graphene at Room Temperature. *Nano Letters*, 11(6):2396–2399, arXiv:1103.4510.

Meshkov, N., Glick, A., and Lipkin, H. (1965). Validity of many-body approximation methods for a solvable model. *Nuclear Physics*, 62(2):199–210.

Milburn, G. J., Corney, J., Wright, E. M., and Walls, D. F. (1997). Quantum dynamics of an atomic Bose–Einstein condensate in a double-well potential. *Physical Review A*, 55(6):4318–4324.

Mølmer, K., Castin, Y., and Dalibard, J. (1993). Monte Carlo wave-function method in quantum optics. *Journal of the Optical Society of America B*, 10(3):524.

Mossmann, S. and Jung, C. (2006). Semiclassical approach to Bose–Einstein condensates in a triple well potential. *Physical Review A*, 74(3):033601.

Olver, F. W. J. et al. (2015). Digital Library of Mathematical Functions.

Pereira, J. M., Peeters, F. M., and Vasilopoulos, P. (2007). Landau levels and oscillator strength in a biased bilayer of graphene. *Physical Review B*, 76(11):115419, arXiv:0708.0843.

Pethick, C. J. and Smith, H. (2008). *Bose–Einstein Condensation in Dilute Gases*. Cambridge University Press, Cambridge, UK.

Pitaevskii, L. and Stringari, S. (2003). *Bose–Einstein Condensation*. Oxford University Press, Oxford.

Plenio, M. B. and Knight, P. L. (1998). The quantum-jump approach to dissipative dynamics in quantum optics. *Reviews of Modern Physics*, 70(1):101–144.

Pudlik, T., Castro Neto, A. H., and Campbell, D. K. (2016). The mesoscopic magnetron as an open quantum system. arXiv:1602.07669.

Pudlik, T., Hennig, H., Witthaut, D., and Campbell, D. K. (2013). Dynamics of entanglement in a dissipative Bose–Hubbard dimer. *Physical Review A*, 88(6):063606.

Pudlik, T., Hennig, H., Witthaut, D., and Campbell, D. K. (2014). Tunneling in the self-trapped regime of a two-well Bose–Einstein condensate. *Physical Review A*, 90(5):053610.

Raghavan, S., Smerzi, A., Fantoni, S., and Shenoy, S. (1999). Coherent oscillations between two weakly coupled Bose–Einstein condensates: Josephson effects, π oscillations, and macroscopic quantum self-trapping. *Physical Review A*, 59(1):620–633.

Rauer, B., Grišins, P., Mazets, I. E., Schweigler, T., Rohringer, W., Geiger, R., Langen, T., and Schmiedmayer, J. (2016). Cooling of a one-dimensional Bose gas. *Physical Review Letters*, 116(3):030402, 1505.04747.

Razavy, M. (2003). *Quantum Tunneling*. World Scientific Publishing Company.

Ruostekoski, J. and Walls, D. F. (1998). Bose–Einstein condensate in a double-well potential as an open quantum system. *Physical Review A*, 58(1):R50–R53, arXiv:9803298.

Ryzhii, V., Ryzhii, M., Mitin, V., and Shur, M. S. (2009). Graphene Tunneling Transit-Time Terahertz Oscillator Based on Electrically Induced pâĂŞiâĂŞn Junction. *Applied Physics Express*, 2:034503.

Sakmann, K. (2010). *Numerically exact dynamics of the interacting many-body Schrödinger equation for Bose–Einstein condensates: comparison to Bose–Hubbard and Gross–Pitaevskii theory*. Doctoral dissertation, Ruperto-Carola-University of Heidelberg.

Sakmann, K. (2011). Exact Quantum Dynamics of a Bosonic Josephson Junction. In *Many-Body Schrödinger Dynamics of Bose–Einstein Condensates*, pages 65—-80. Springer Berlin Heidelberg, Berlin, Heidelberg.

Sakmann, K., Streltsov, A. I., Alon, O. E., and Cederbaum, L. S. (2009). Exact Quantum Dynamics of a Bosonic Josephson Junction. *Physical Review Letters*, 103(22):220601.

Salgueiro, A. N., de Toledo Piza, A. F. R., Lemos, G. B., Drumond, R., Nemes, M. C., and Weidemüller, M. (2007). Quantum dynamics of bosons in a double-well potential: Josephson oscillations, self-trapping and ultralong tunneling times. *The European Physical Journal D*, 44(3):537–540.

Scharf, G., Wreszinski, W. F., and Hemmen, J. L. (1987). Tunnelling of a large spin: mapping onto a particle problem. *Journal of Physics A: Mathematical and General*, 20(13):4309–4319.

Schutz, B. (1980). *Geometrical Methods of Mathematical Physics*. Cambridge University Press, Cambridge, UK.

Smerzi, A., Fantoni, S., Giovanazzi, S., and Shenoy, S. R. (1997). Quantum Coherent Atomic Tunneling between Two Trapped Bose–Einstein Condensates. *Physical Review Letters*, 79(25):4950–4953.

Steel, M. J. and Collett, M. J. (1998). Quantum state of two trapped Bose–Einstein condensates with a Josephson coupling. *Physical Review A*, 57(4):2920–2930, arXiv:9710124.

Tomka, M. (2014). *Geometric Effects in Quantum Non-Equilibrium Dynamics*. Doctoral dissertation, University of Fribourg.

Trimborn, F., Witthaut, D., Hennig, H., Kordas, G., Geisel, T., and Wimberger, S. (2011). Decay of a Bose–Einstein condensate in a dissipative lattice âĂŞ the mean-field approximation and beyond. *The European Physical Journal D*, 63(1):63–71.

Trimborn, F., Witthaut, D., and Korsch, H. (2008a). Exact number-conserving phase-space dynamics of the M-site Bose–Hubbard model. *Physical Review A*, 77(4):043631.

Trimborn, F., Witthaut, D., and Korsch, H. (2009). Beyond mean-field dynamics of small Bose–Hubbard systems based on the number-conserving phase-space approach. *Physical Review A*, 79(1):013608.

Trimborn, F., Witthaut, D., and Wimberger, S. (2008b). Mean-field dynamics of a two-mode Bose–Einstein condensate subject to noise and dissipation. *Journal of Physics B: Atomic, Molecular and Optical Physics*, 41(17):171001.

Trombettoni, A. and Smerzi, A. (2001). Discrete Solitons and Breathers with Dilute Bose–Einstein Condensates. *Physical Review Letters*, 86(11):2353–2356.

van Hemmen, J. L. and Sütö, A. (1986). Tunnelling of quantum spins. *Europhysics Letters (EPL)*, 1(10):481–490.

Walls, D. F. and Milburn, G. J. (2008). *Quantum Optics*. Springer-Verlag, Berlin, Heidelberg, 2nd ed edition.

Wang, J. I.-J., Yang, Y., Chen, Y.-A., Watanabe, K., Taniguchi, T., Churchill, H. O. H., and Jarillo-Herrero, P. (2015). Electronic Transport of Encapsulated Graphene and WSe 2 Devices Fabricated by Pick-up of Prepatterned hBN. *Nano Letters*, 15(3):1898–1903.

Wickramaratne, D., Zahid, F., and Lake, R. K. (2015). Electronic and thermoelectric properties of van der Waals materials with ring-shaped valence bands. *Journal of Applied Physics*, 118(7):075101, arXiv:1412.2090.

Wiseman, H. M. and Milburn, G. J. (2010). *Quantum Measurement and Control*. Cambridge University Press.

Witthaut, D., Trimborn, F., Hennig, H., Kordas, G., Geisel, T., and Wimberger, S. (2011). Beyond mean-field dynamics in open Bose–Hubbard chains. *Physical Review A*, 83(6):063608.

Witthaut, D., Trimborn, F., and Wimberger, S. (2008). Dissipation Induced Coherence of a Two-Mode Bose–Einstein Condensate. *Physical Review Letters*, 101(20):200402.

Wolff, P. A. (1966). Cyclotron resonance laser. U.S. Patent No. 3,265,977.

Würtz, P., Langen, T., Gericke, T., Koglbauer, A., and Ott, H. (2009). Experimental Demonstration of Single-Site Addressability in a Two-Dimensional Optical Lattice. *Physical Review Letters*, 103(8):080404.

Zhang, W.-M., Feng, D. H., and Gilmore, R. (1990). Coherent states: Theory and some applications. *Reviews of Modern Physics*, 62(4):867–927.

Zibold, T. (2012). *Classical Bifurcation and Entanglement Generation in an Internal Bosonic Josephson Junction.* Doctoral dissertation, Ruperto-Carola-University of Heidelberg.

Zibold, T., Nicklas, E., Gross, C., and Oberthaler, M. K. (2010). Classical Bifurcation at the Transition from Rabi to Josephson Dynamics. *Physical Review Letters*, 105(20):204101.

Zudov, M. A., Du, R. R., Simmons, J. A., and Reno, J. L. (2001). Shubnikov–de Haas-like oscillations in millimeterwave photoconductivity in a high-mobility two-dimensional electron gas. *Physical Review B*, 64(20):201311.

Curriculum Vitae

Contact   Tadeusz Pudlik

Department of Physics, Boston University, 590 Commonwealth Avenue, Boston, MA 02215

tpudlik@gmail.com

Education   **Amherst College**, B.A., Physics and Economics, September 2005 – May 2009.

Boston University Ph.D. candidate, September 2010 – present. Thesis advisor: David K. Campbell.

Publications 1. H. O. Leung, M. D. Marshall, T. L. Drake, T. Pudlik, N. Savji, D. W McCune, "Fourier transform microwave spectroscopy and molecular structure of the 1,1-difluoroethylene-hydrogen fluoride complex," *Journal of Chemical Physics* **131** (20) 204301 (2009).

2. T. Pudlik, H. Hennig, D. Witthaut, and D. K. Campbell, "Dynamics of entanglement in a dissipative Bose-Hubbard dimer," *Physical Review A* **88**, 1 (2013).

3. T. Pudlik, H. Hennig, D. Witthaut, and D. K. Campbell, "Tunneling in the self-trapped regime of a two-well Bose–Einstein condensate," *Physical Review A* **90** 053610 (2014).

4. T. Pudlik, A. H. Castro Neto, and D. K. Campbell, "The mesoscopic magnetron as an open quantum system," arXiv:1602.07669 (2016).